NATIONAL INSTITUTE FOR FUSION SCIENCE

Proceedings of The US-Japan Workshop and
The Satellite Meeting of ITC-9 on Physics of High Beta
Plasma Confinement in Innovative Fusion System
Dec. 14-15, 1998, NIFS, Toki

(Ed.) S. Goto and S. Yoshimura

(Received - Apr. 8, 1999   )

NIFS-PROC-41   Apr. 1999

RESEARCH REPORT
NIFS-PROC Series

NAGOYA, JAPAN

Proceedings

of

The US-Japan Workshop and The Satellite Meeting of ITC-9 on Physics of High Beta Plasma Confinement in Innovative Fusion System

December 14-15, 1998, NIFS, Toki

edited by

Seiichi Goto

Satoru Yoshimura

Abstract

The US-Japan Workshop on Physics of High Beta Plasma Confinement in Innovative Fusion System was held jointly with the Satellite Meeting of ITC-9 at National Institute for Fusion Science (NIFS), Toki-city during December 14-15, 1998. This proceedings book includes the papers of the talks given at the workshop. These include: Theoretical analysis on the stability of field reversed configuration (FRC) plasmas; Theory and Modeling of high β plasmas; Recent progressive experiments in high β systems; Formation of high β plasmas using merging phenomenon; Theory and Modeling of a FRC Fusion Reactor.

Contents

List of participants

US participants		
Name	Affiliation	e-mail address
H. Ji	PPPL	hji@pppl.gov
W. Park	PPPL	wpark@pppl.gov
J. Slough	Univ. Washington	slough@aa.washington.edu
L. Steinhauer	Univ. Washington	steinhauer@aa.washington.edu
G. A. Wurden	Los Alamos Nat. Lab.	wurden@lanl.gov
M. Yamada	PPPL	myamada@pppl.gov
Japanese participants		
Name	Affiliation	e-mail address
S. Hamada	Nihon Univ.	hamada@phys.cst.nihon-u.ac.jp
H. Himura	Univ. Tokyo	himura@plasma.q.t.u-tokyo.ac.jp
R. Horiuchi	NIFS	hori@toki.theory.nifs.ac.jp
A. Ishida	Dept. Environmental Sci., Niigata Univ.	ishida@artemis.ge.niigata-u.ac.jp
M. Ishikawa	Inst. Eng. Mechanics, Univ. Tsukuba	misikawa@kz.tsukuba.ac.jp
N. Iwasawa	Niigata Univ.	iwasawa@artemis.ge.niigata-u.ac.jp
K. Kitano	Plasma Phys. Lab., Osaka Univ.	kitano@ppl.eng.osaka-u.ac.jp
S. Mima	Dept. Electr. Eng., Kyoto Univ.	mima@denjiki1.kuee.kyoto-u.ac.jp
H. Momota	Univ. Illinois at Urbana-Champaign	momota@staff.uiuc.edu
K. Nishimura	NIFS	nisimura@toki.theory.nifs.ac.jp
Y. Nogi	Nihon Univ.	nogi@pyxis.phys.cst.nihon-u.ac.jp
M. Ohnishi	Inst. Advanced Energy, Kyoto Univ.	onishi@iae.kyoto-u.ac.jp
S. Okada	Plasma Phys. Lab., Osaka Univ.	okada@ppl.eng.osaka-u.ac.jp
Y. Ono	Dept. Electr. Eng., Univ. Tokyo	a13931@tina.oc.t.u-tokyo.ac.jp
Y. Shimizu	Dept. Electr. Eng., Kyoto Univ.	shimizu@denjiki1.kuee.kyoto-u.ac.jp
T. Takahashi	Dept. Electr. Eng., Gunma Univ.	t-tak@el.gunma-u.ac.jp
Y. Tomita	NIFS	tomita@nifs.ac.jp
Y. Ueda	Dept. Electr. Eng., Univ. Tokyo	kien@katsurai.t.u-tokyo.ac.jp
T. Watanabe	NIFS	tomo@nifs.ac.jp
H. Yamada	Niigata Univ.	
K. Yamanaka	Plasma Phys. Lab., Osaka Univ.	kojiy@ppl.eng.osaka-u.ac.jp
Y. Yasaka	Dept. Electronic Sci. Eng., Kyoto Univ.	yasaka@kuee.kyoto-u.ac.jp
S. Yoshimura	Plasma Phys. Lab., Osaka Univ.	yosimura@ppl.eng.osaka-u.ac.jp
Participants from other countries		
Name	Affiliation	e-mail address
B. Dasgupta	Saha Inst. Nucl. Phys., India	dasgupta@plasma.saha.ernet.in
V. I. Khvesyuk	Bauman Moscow State Univ., Russia	postmaster@khvesyuk.msk.ru
R. Kh. Kurtmullaev	Russian State Res. Center TRINITI, Russia	plasmoid@fly.triniti.troitsk.ru
V. N. Litunovsky	D.V.Efremov Sci. Res. Inst., Russia	vlitun@niiefa.spb.su

Stability Property of Field-Reversed Configurations

Naotaka Iwasawa

Graduate School of Science and Technology, Niigata University

Ikarashi, Niigata 950-2181, Japan

Akio Ishida

Department of Environmental Science, Faculty of Science, Niigata University

Ikarashi, Niigata 950-2181, Japan

Loren C. Steinhauer

University of Washington, Redmond Plasma Physics Laboratory

Redmond, Washington 98052, USA

I. Introduction

Field-reversed configurations (FRCs) have been produced successfully by several formation techniques. This shows that FRCs are grossly stable. Nevertheless the tilt mode stability theories, which have been developed extensively for more than 15 years, cannot explain the gross stability observed in the experiments. R. Kanno *et al.* examined the stabilizing effects of separatrix shape and current profile on the tilt mode by means of ideal MHD model without plasma flow [1]. To represent the displacements, they used up to 3 basis functions (as a result, the eigen displacement was *almost rigid*). They found the MHD stable domain against the tilt mode for sufficiently hollow current profile and sufficiently racetrack separatrix shape. However in our recent study where the more accurate numerical technique was employed, we found that there was no such MHD tilt stable domain and found that the accurate numerical technique is necessary to study the stability property of FRCs [2].

In this paper, for the purpose of offering a fundamental basis to understand FRC stability, we study the MHD stability properties of FRC eigenmodes with toroidal mode number $l = 1$ and intermediate toroidal mode numbers $l = 2 - 30$ in various FRCs. And we examine the stabilizing effect of the gyroviscosity.

II. Method

One-fluid MHD model is used here to represent equilibria of FRCs with no flow [1, 2]. The equilibria are characterized by (1) the separatrix shape, (2) the current profile index h, and (3) the separatrix elongation E. The following parameter regions have been examined, (1) separatrix shapes: elliptic and racetrack-type ($N = 1$, N is the elongation of the "end cap" region [1]), (2) h: 1 (flat current profile) and 0.8 (hollow current profile), (3) $E: 0.8 - 5$ for the elliptic case and $1 - 5$ for the racetrack case. Fig. 1 shows the examples of the elliptic/flat and the racetrack/flat equilibria with various values of elongation.

To investigate stability of these equilibria we apply the variational principle, $\delta I = 0$,

with variational form I:

$$I[\xi] = \int d\tau \xi^{+} \bullet \left[\omega^2 \rho \xi + \mathbf{F}(\xi) + i\omega \mathbf{G}(\xi)\right] \qquad (2.1)$$

where the integral is over the entire volume. Here ξ is the displacement of the mode considered, ω is the mode frequency, the terms in the square bracket are the inertia term, the ideal MHD force, the force due to the ion's gyroviscosity, respectively [3].

The displacement ξ is expanded in Fourier series in terms of 'boundary-fitted' orthogonal coordinates $V(r,z)$ and $U(r,z)$ [2], and Rayleigh-Ritz method is used to solve $\delta I = 0$.

We assume that the compressibility is negligible and eliminate the azimuthal component ξ_θ using the relation, $i\xi_\theta = -[\partial(r\xi_r)/\partial r + r \partial\xi_z/\partial z]$. And only internal modes, which have no normal component at the separatrix, are studied here. Under these two assumptions modes with the toroidal mode numbers $l = 1 - 30$ are studied. The upper limit $l = 30$ is chosen where the poloidal structure of the modes, similar to those of the $l = \infty$ modes, appear in all of the equilibria examined.

III. Results

A. MHD Stability of $l = 1$ Modes

Fig. 2 shows the normalized growth rates vs. elongation of the most unstable $l = 1$ odd (tilt) and even modes, where a is the separatrix radius at $z = 0$, $V_{A0} = B_a/(4\pi\rho_{max})^{1/2}$, ρ_{max} is the mass density at the magnetic axis, and B_a is the magnetic field at $z = 0$, $r = a$. In the elliptic/flat case, the $l = 1$ odd (tilt) mode is stable in the oblate equilibria, while it is unstable in the prolate equilibria. The $l = 1$ even mode is always stable in this case. In the elliptic/hollow case, only $l = 1$ even mode has a trend different from the flat current case. It is unstable in this case. In the racetrack/flat case (all equilibria are prolate in the racetrack case), the $l = 1$ odd (tilt) and even modes are unstable. In the racetrack/hollow case, the $l = 1$ odd (tilt) and even mode have the same trends as in the flat current case. We can conclude that the oblate equilibria are stable against the $l = 1$ odd (tilt) and even modes, while the prolate equilibria are unstable.

Fig. 3 shows the poloidal structure of the $l = 1$ odd (tilt) and even modes in the elliptic/flat and the racetrack/flat equilibria. As the elongation increases, the activity concentrates near the magnetic axis in the elliptic case, while the activity concentrates near the FRC end region in the racetrack case. In all of the equilibria examined in this study, the $l = 1$ odd (tilt) and even modes have much smaller displacements at the separatrix than in the interior region. This means that the $l = 1$ modes are actually "internal".

B. MHD Stability of Higher l Modes

Fig. 4 shows the growth rates vs. elongation of the most unstable higher l odd and even modes in the elliptic equilibria ((a) and (b)) and in the racetrack equilibria ((c) and (d)). ● shows the growth rates of the $l = 1,2,3,5,10$, and 30 (from the bottom to the top) odd and even modes in the flat current case. ○ in Fig. 4b shows the growth rates of the $l = 1$ (lower) and the $l = 2$ (upper) even modes in the hollow current case (These modes are stable in the

flat current case). For comparison, the growth rates of Newcomb's co-interchange ($l = \infty$) modes $\sqrt{2}/E$ (the broken lines in Fig. 4 (a) and (b)) [4] and the growth rates of the most unstable $l = \infty$ local modes in the racetrack/flat, $E = 5$ equilibrium (crosses in Fig. 4 (c) and (d)) [5] are shown. In all of the equilibria examined, as l increases the growth rates increase and approach to those of the $l = \infty$ modes.

Fig. 5 shows the poloidal structure of the $l = 1$, 3, 30, and ∞ [5] odd modes in the racetrack/flat, $E = 5$ equilibrium. As l increases the mode activity concentrates around some specific magnetic field line and the structure approach to the one of the $l = \infty$ local mode. The same trend can be seen in the unstable modes in other equilibria.

C. Effect of Gyroviscosity on the $l = 1$ Odd Modes

In Sec. IIIA and IIIB, only the most unstable MHD modes were shown. However there are several types of unstable MHD modes for a fixed toroidal mode number and a fixed odd/even symmetry in each equilibrium. Fig. 6 shows the most, 2nd, and 3rd unstable $l = 1$ odd MHD modes in the elliptic/flat equilibrium. In the most unstable $l = 1$ odd MHD mode the activity concentrates the magnetic axis. The less unstable, the more broadly the activity distributes. And the structure becomes finer. Note that the 2nd and 3rd unstable modes have significant growth rates. In the following, we examine the effect of the gyroviscosity on the most and 2nd unstable modes, and then estimate the gyroviscous stability property of FRCs.

Fig. 7 shows the growth rates vs. $1/S_*$ of the most ($\bigcirc$) and 2nd ($\bullet$) unstable $l = 1$ odd MHD modes, where $S_* = a(4\pi e^2 n_{max}/Mc^2)^{1/2}$ is the size parameter, M is the ion mass, and n_{max} is the number density at the magnetic axis. The most unstable MHD mode has a stability boundary at $1/S_* \cong 0.011$ ($S_* \cong 90$). The stability boundary value of $1/S_*$ still depends on the number of basis functions N_{basis}. However, it is found that as N_{basis} increases the value of $1/S_*$ decreases. Therefore this mode is stable at least for $1/S_* > 0.011$ ($S_* < 90$). While the 2nd unstable MHD mode (the growth rates are independent of N_{basis} in this case) cannot be stabilized for $1/S_* < 0.1$ ($S_* > 10$).

The gyroviscosity effectively suppresses activity near the magnetic axis where the magnetic field is weak. Thus the most unstable MHD mode shown above can be effectively stabilized. In the 2nd unstable MHD mode shown above, the activity near the magnetic axis is effectively suppressed, while the activity away from the magnetic axis is ineffectively suppressed by the gyroviscosity (see Fig. 8). All of the prolate equilibria examined have this type of MHD mode. Consequently, the gyroviscous stability boundary may exist at $S_* \ll 10$. It is unrealistic (see FIG. 5 in Ref. 6). Thus the effect of the gyroviscosity alone is not sufficient to explain the stability property of FRCs.

IV. Summary and Discussion

In the present study, using 'boundary-fitted' orthogonal coordinates, we developed the accurate numerical method of FRC stability analysis, and found eigenmodes with $l = 1 - 30$ in the various equilibria, and examined the effect of the gyroviscosity on the global mode stability. As a result, we found that oblate FRCs are stable against the $l = 1$ odd (tilt) and

even modes. And the most unstable $l = 1$ odd (tilt) and even modes are found to be actually internal. As l increases, the growth rates and the poloidal structure of the most unstable higher l modes tend to approach those of the most unstable $l = \infty$ local modes. The gyroviscosity stabilizes effectively the $l = 1$ odd MHD mode that concentrates its activity near the magnetic axis, while it cannot stabilize the mode where its activity distributes broadly or away from the magnetic axis. As a result, any prolate FRC examined has no gyroviscous stability window for the internal global mode. Experiments show that (1) long lived prolate FRCs can be produced, and (2) the current profile is found to be hollow. The present study cannot explain these two properties. Parallel viscosity seems to be insignificant because the mode, in which the activity distributes away from the magnetic axis, could not stabilized by simultaneous effect of the gyroviscosity and the parallel viscosity [2]. This suggests that new stabilizing mechanism must be taken into account and it should entirely distribute within the separatrix. Shear flow may be a candidate. We are now trying to challenge the problem.

References

[1] R. Kanno, A. Ishida, and L. C. Steinhauer, J. Phys. Soc. Japan **64**, 463 (1995).

[2] N. Iwasawa, A. Ishida, and L. C. Steinhauer, Proceedings of US-Japan workshop on Physics of High-Beta Fusion Plasmas (University of Washington, 18-20 March, 1998).

[3] A. Ishida, L. C. Steinhauer, and H. L. Berk, Phys. Fluids **B3**, 1552 (1991).

[4] A. Ishida, N. Shibata, and L. C. Steinhauer, Phys. Plasmas **3**, 4278 (1996).

[5] A. Ishida, N. Shibata, and L. C. Steinhauer, Phys. Plasmas **1**, 4022 (1994).

[6] A. Ishida, R. Kanno, and L. C. Steinhauer, Phys. Fluids B **4**, 1280 (1992).
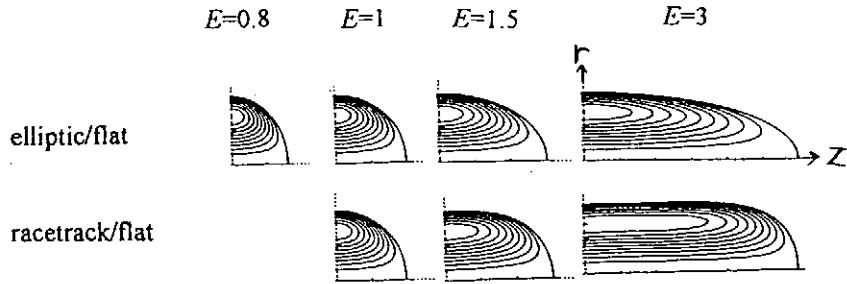
Fig. 1. Examples of the equilibria. The curves are contours of the flux functions $\psi(r,z)$.

(a)

- $\bullet$ *elliptic/flat, l=1 odd*
- $\blacktriangle$ *elliptic/flat, l=1 even*
- $\triangle$ *elliptic/hollow, l=1 even*

(b)

- $\bullet$ *racetrack/flat, l=1 odd*
- $\blacktriangle$ *racetrack/flat, l=1 even*
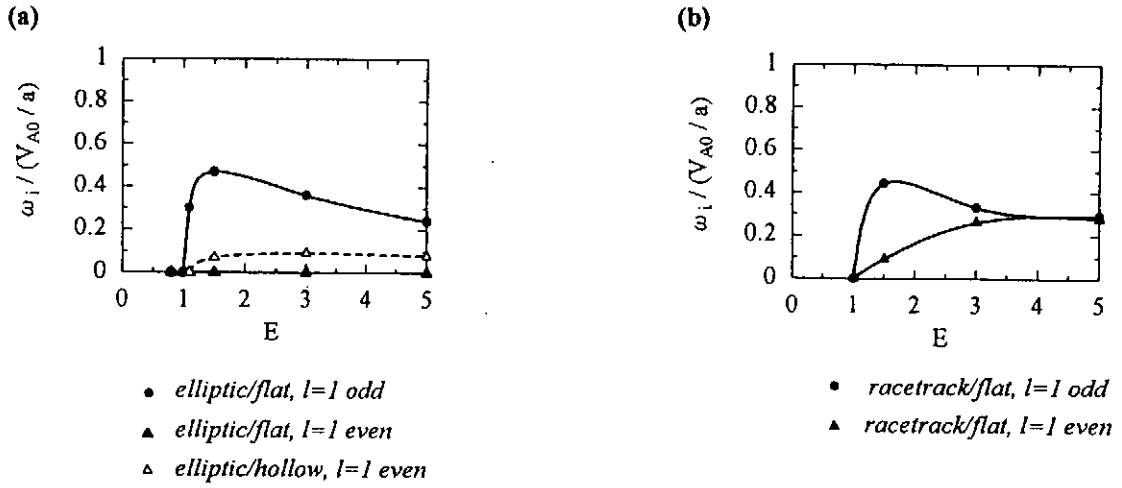
Fig. 2. The growth rates of the most unstable $l = 1$ modes vs. elongation.

(a)
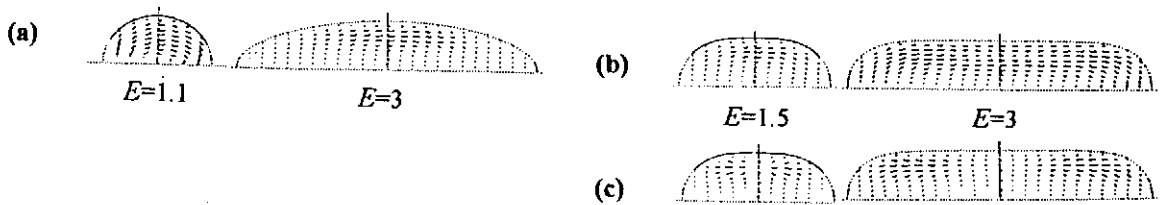
Fig. 3. The poloidal structure of the most unstable $l = 1$ modes: (a) odd (tilt) modes in the elliptic/flat; (b) odd (tilt) modes in the racetrack/flat; (c) even modes in the racetrack/flat.

elliptic

(a)   **(b)**
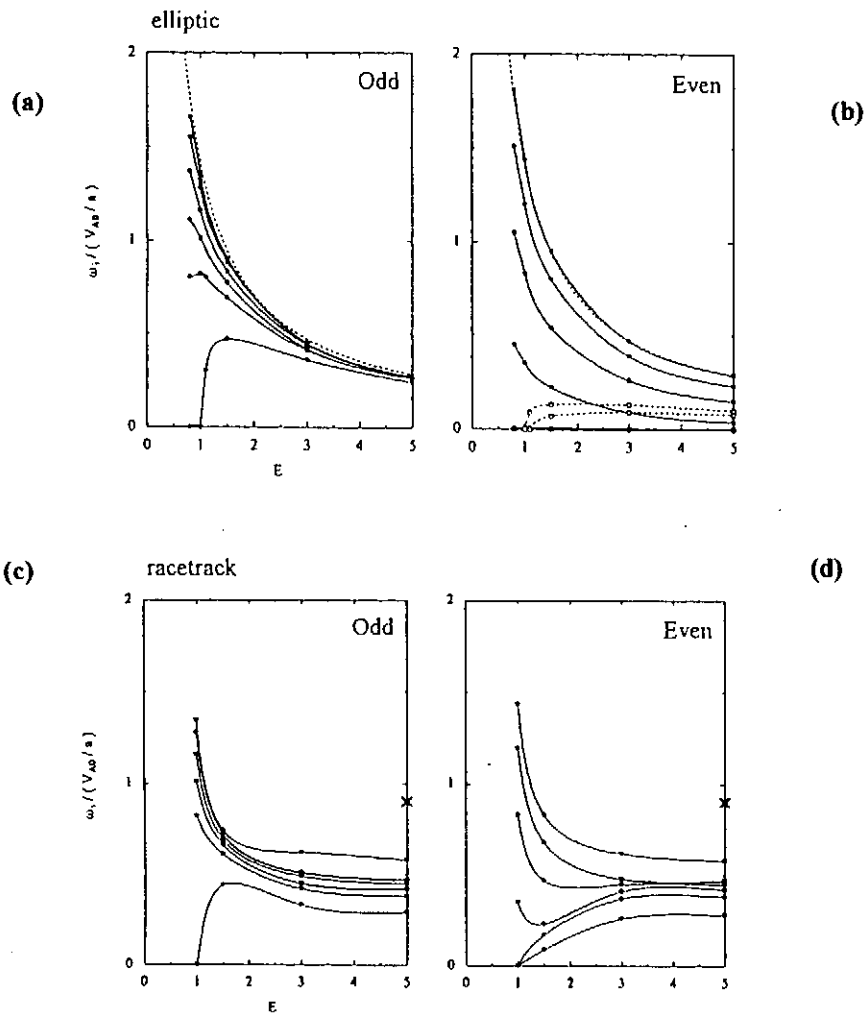
(c)   racetrack   **(d)**

Fig. 4. The growth rates of the most unstable higher l modes vs. elongation.

$l=1$

$l=3$

$l=30$

$l=\infty$
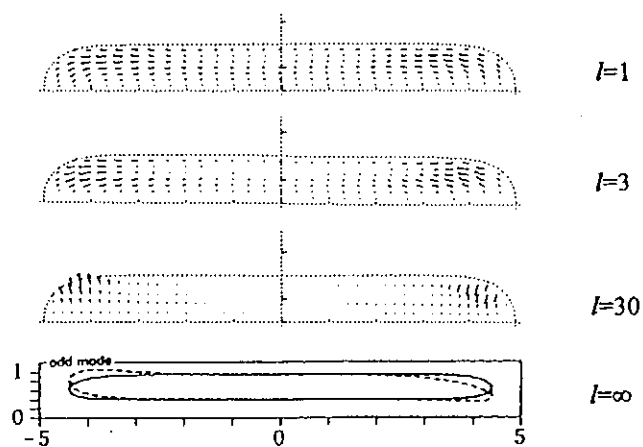
Fig. 5. The poloidal structure of the l = 1, 3, 30, and ∞ odd unstable modes in the racetrack/flat, E = 5 equilibrium.

$$\frac{\omega_i}{(V_{A0}/a)}=0.24$$

the most unstable

0.19

the 2 nd unstable

0.15
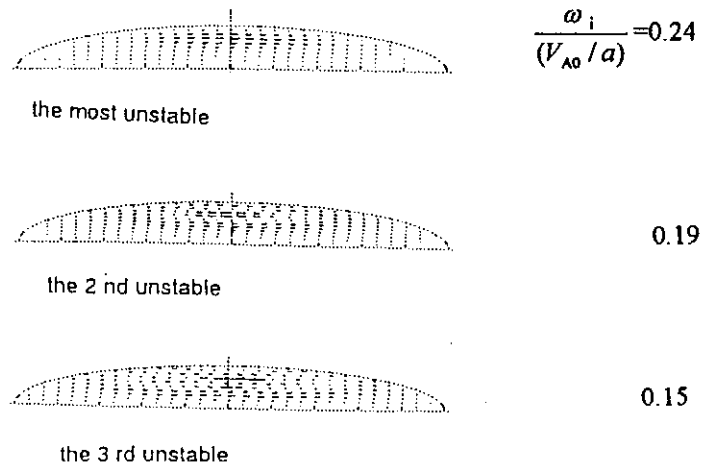
the 3 rd unstable

Fig. 6. The poloidal structure of the most, 2nd, and 3rd unstable $l = 1$ odd MHD modes in the racetrack/flat, $E = 5$ equilibrium.

Fig. 8. The poloidal structure of the 2nd unstable MHD mode in Fig. 6 with $1/S_* = 0.1$.

Fig. 7. The growth rates vs. $1/S_*$ of the most (O) and 2nd (●) unstable MHD modes in Fig. 6.

Two-Fluid Equilibria with Flow

Loren Steinhauer
University of Washington

Abstract

The formalism is developed for flowing two-fluid equilibria. The equilibrium system is governed by a pair of second order partial differential equations for the magnetic stream function and the ion stream function plus a Bernoulli-like equation for the density. There are six arbitrary surface function. There are separate characteristic surfaces for each species, which are the guiding-center surfaces. This system is a generalization of the familiar Grad-Shafranov system for a single-fluid equilibrium without flow, which has only one equation and tw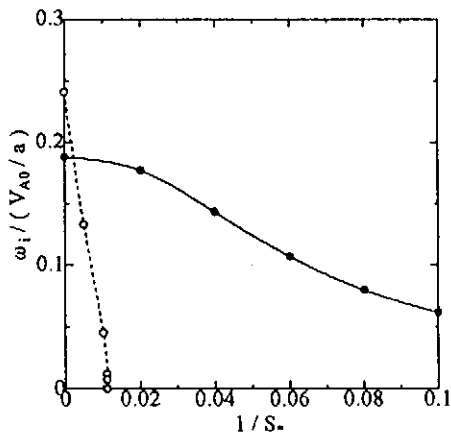o arbitrary surface functions. In the case of minimum energy equilibria, the six surface functions take on particular forms.

I. Introduction

We consider a two-fluid plasma for which the constituents of the system are the electron and ion fluids (hydrogen), and the electromagnetic fields. The objective is to establish the formalism for finding axisymmetric equilibria. This is a significant generalization of the equilibrium problem for a non-flowing single fluid (MHD) which is governed by the Grad-Shafranov (GS) equation. The GS system is a single second order partial differential equation for the magnetic stream function ψ; its characteristic surfaces satisfy $\psi = const$; and it involves two arbitrary surface functions, the toroidal field function $\phi(\psi)$ and the pressure function $p(\psi)$, where. The generalized equilibrium system should also be expressible in terms of stream functions, characteristic surfaces, and arbitrary surface functions. However since we are considering a two fluid with flow, the corresponding system is necessarily much more complicated. The task then is to identify the appropriate stream functions, the characteristic surfaces, and the arbitrary surface functions.

II. Equilibrium state equations

Expression in terms of scalar functions. Axisymmetry with the steady Faraday's law, Gauss's law of magnetism, and the steady continuity equations imply the existence of scalar functions of (r,z) such that

$$\mathbf{E} = -\nabla V_{es}; \qquad \mathbf{B} = \frac{\hat{\theta}}{r}\phi + \frac{\hat{\theta}}{r}\times\nabla\psi; \qquad n_\alpha\mathbf{u}_\alpha = \frac{\hat{\theta}}{r}\phi_\alpha + \frac{\hat{\theta}}{r}\times\nabla\psi_\alpha \qquad (1,2,3)$$

where the seven scalar functions (of r,z) are the electrostatic potential V_{es}, the toroidal field and flow functions ϕ and ϕ_α [$\alpha = i$(ions), e(electrons)], and the poloidal field and flow functions ψ and ψ_α ($\alpha = i, e$).

Fluid-field coupling. The fluid and field behavior are coupled through Ampere's and Gauss's laws, and the equations of motion of each species. The toroidal and poloidal components of the steady Ampere's law are

$$\Delta^{*}\psi \ = \ \frac{4\pi}{c}\sum_{\alpha}q_{\alpha}\phi_{\alpha}, \qquad \phi \ = \ -\frac{4\pi}{c}\sum_{\alpha}q_{\alpha}\psi_{\alpha}, \qquad (4,5)$$

respectively. Gauss's law is

$$\nabla^{2}V_{es} \ = \ -\sum_{\alpha}q_{\alpha}n_{\alpha} \qquad (6)$$

The equations of motion take on a particularly simple form in terms of the generalized vorticity, $\Omega_{\alpha} = m_{\alpha}\nabla\times\mathbf{u}_{\alpha} + (q_{\alpha}/c)\mathbf{B}$, which proved to be an important vector quantity in the modern (two-fluid) relaxation theory [1,2].

$$\nabla\left(m_{\alpha}u_{\alpha}^{2}/2 + q_{\alpha}V_{es}\right) + \frac{\nabla p_{\alpha}}{n_{\alpha}} \ = \ \mathbf{u}_{\alpha}\times\Omega_{\alpha}. \qquad (7)$$

Equation of state. An equation of state can greatly simplify the equation of motion. Two reasonable examples are barotropic species, $p_{\alpha} = p_{\alpha}(n_{\alpha})$ and isothermal characteristic surfaces, $T_{\alpha} = T_{\alpha}(F)$ where the surfaces $F = const$ remain to be determined. In both cases we can define a useful function h_{α}. In the barotropic case $h_{\alpha} \equiv \int dp_{\alpha}/n_{\alpha}$, and in the isothermal surface case $h_{\alpha} \equiv kT_{\alpha}(F)\ln(n_{\alpha})$. In the former case each equation of motion becomes

(barotropic) $\qquad \nabla\left(h_{\alpha} + m_{\alpha}u_{\alpha}^{2}/2 + q_{\alpha}V_{es} + m_{\alpha}V_{g}\right) \ = \ \mathbf{u}_{\alpha}\times\Omega_{\alpha}. \qquad (8)$

In the latter case a slightly less general form follows

(isothermal) $\qquad \left(\frac{\hat{\theta}}{r}\times\nabla F\right)\cdot\left[\nabla\left(h_{\alpha} + m_{\alpha}u_{\alpha}^{2}/2 + q_{\alpha}V + m_{\alpha}V_{g}\right) - \mathbf{u}_{\alpha}\times\Omega_{\alpha}\right] \ = \ 0 \quad (9)$

Surface functions. The three principal directions for each species of a two fluid are the θ direction, the direction of Ω_{α}, and the mutually perpendicular direction, $\hat{\theta}\times\Omega_{\alpha}$. These directions are different for the electrons and ions. Since $\nabla\cdot\Omega_{\alpha} = 0$ one can express the generalized vorticity in terms of *new* toroidal and poloidal functions $\Phi_{\alpha}, \Psi_{\alpha}$:

$$\Omega_{\alpha} \ = \ \frac{q_{\alpha}}{c}\left(\frac{\hat{\theta}}{r}\Phi_{\alpha} + \frac{\hat{\theta}}{r}\times\nabla\Psi_{\alpha}\right) \qquad (10)$$

From Eqs. 2,3 these are given by:

$$\Phi_{\alpha} \ = \ \phi + \frac{m_{\alpha}c}{q_{\alpha}n_{\alpha}}\Delta_{n}^{*}\psi_{\alpha}; \qquad \Psi_{\alpha} \ = \ \psi - \frac{m_{\alpha}c}{q_{\alpha}n_{\alpha}}\phi_{\alpha} \qquad (11,12)$$

where the density-weighted GS operator is defined by $\Delta^{*}F = nr^{2}\nabla\cdot(\nabla F/nr^{2})$. The ordinary GS operator Δ^{*} has the same form but without the density. The characteristic surface functions for each species are defined by $\Psi_{\alpha} = const$. Observe that the ion and electron surfaces are not the same. This choice is justified by the simplification in the components of the equations of motion in these directions. The component in the θ direction (angular momentum) leads to $\Omega_{\alpha}\cdot\nabla\psi_{\alpha} = 0$, which implies

$$\psi_{\alpha} \ = \ G_{\alpha}(\Psi_{\alpha}) \qquad (13)$$

where G_i and G_e are arbitrary surface functions. The parallel component (Ω_{α} direction) leads to Bernoulli equations for each species

$$h_{\alpha} + m_{\alpha}u_{\alpha}^{2}/2 + q_{\alpha}V_{es} + m_{\alpha}V_{g} \ = \ H_{\alpha}(\Psi_{\alpha}) \qquad (14)$$

where H_i and H_e are arbitrary surface functions. The perpendicular component ($\nabla \Psi_\alpha$ direction) is

$$\frac{q_\alpha}{c} G'_\alpha \Phi_\alpha - \frac{q_\alpha}{c} \phi_\alpha = nr^2 [H'_\alpha + kT'_\alpha (1 - \ln n)] \qquad (15)$$

where $(..)'$ denotes the derivative of a surface quantity with respect to Ψ_α. This form applies for isothermal surfaces. For barotropic species the kT'_α term is absent.

The surface function Ψ_α is identical to rP_θ, the angular momentum. In an axisymmetric geometry, the free motion of particles preserves rP_θ. Thus, the surfaces $\Psi_\alpha = const$ are surfaces along which free motion of particles takes place. This is significant because the *parallel* thermal conduction (coefficient $K_{\parallel\alpha}$) is in this direction. Thus in a hot plasmas with large $K_{\parallel\alpha}$, the temperature of species α should be nearly uniform on the surfaces $\Psi_\alpha = const$; this is precisely the isothermal surface case.

III. Systems of equations for flowing two-fluid equilibria

Reducing assumption. Thus far we have made no reducing assumption beyond the basic two-fluid model. Suppose we assume quasineutrality ($n_i = n_e = n$) and massless electrons ($m_e \rightarrow 0$); then the system becomes

$$\Delta^* \psi = \frac{4\pi e}{c}(\phi_i - \phi_e) \qquad\qquad \phi = -(4\pi e/c)(\psi_i - \psi_e) \qquad (16,17)$$

$$\psi_i = G_i(\Psi_i) \qquad\qquad\qquad \psi_e = G_e(\Psi_e) \qquad (18,19)$$

$$h_i + m_i u_i^2/2 + eV_{es} + m_i V_g = H_i(\Psi_i) \qquad h_e - eV_{es} = H_e(\psi) \qquad (20,21)$$

$$\frac{m_i}{n} G'_i \Delta^*_n \psi_i = -\frac{e}{c}\phi G'_i + \frac{e}{c}\phi_i + nr^2[H'_i + kT'_i(1 - \ln n)] \qquad (22)$$

$$0 = \frac{e}{c}\phi G'_e - \frac{e}{c}\phi_e + nr^2[H'_e + kT'_e(1 - \ln n)] \qquad (23)$$

which are the toroidal and poloidal Ampere's laws, the two angular momenta, the two Bernoulli equations, and the two perpendicular momentum equations, respectively. Recall that the surface functions are defined in Eq. 12. This system includes the arbitrary surface functions are $G_i(\Psi_i)$, $G_e(\psi)$, $H_i(\Psi_i)$, $H_e(\psi)$, and (in the isothermal surface case) $T_i(n)$, $T_e(n)$. The eight unknowns are ψ, ϕ, ψ_i, ϕ_i, ψ_e, ϕ_e, V_{es}, and n.

Minimum energy equilibria. The theory of two-fluid minimum energy states was developed elsewhere [SI3-PoP]. This theory is based on the minimization of the magnetofluid energy given fixed values of certain invariants. The magnetofluid energy is the sum of the total magnetic energy and the flow kinetic energy in the system.

$$W_{mf} = \int d\tau (B^2/8\pi + m_i n u_i^2/2) \qquad (24)$$

The proper invariants for a two-fluid are the self helicities for each species, and (for axisymmetric system boundary) the global angular momentum:

$$K_\alpha = (c^2/8\pi e^2)\int d\tau\, \mathbf{P}_\alpha \cdot \nabla \times \mathbf{P}_\alpha \qquad L_\theta = \int d\tau\, rm_i n u_{i\theta} \qquad (25,26)$$

respectively; where $\mathbf{P}_\alpha = m_\alpha \mathbf{u}_\alpha + q_\alpha \mathbf{A}/c$ is the canonical momentum for species $\alpha = i$(ions), e(electrons).

The minimum energy equilibria is a much more restrictive set so that the surface functions G_α, H_α, T_α ($\alpha = i,e$) are no longer arbitrary. In fact they depend on the Lagrange multipliers used in the constrained minimization procedure.

$$G_\alpha(\Psi_\alpha) = \lambda_\alpha \frac{c}{4\pi q_\alpha} \Psi_\alpha; \qquad H_\alpha(\Psi_\alpha) = -(q_\alpha/c)\Omega\Psi_\alpha + const; \qquad (27,28)$$

$$T_\alpha(\Psi_\alpha) = const \qquad (29)$$

This leads to the simplified system for a relaxed equilibrium composed of two second order partial differential equations for ψ and ψ_i:

$$\Delta^* \frac{e\psi}{m_i c} = \frac{1}{\ell_c^2}\left[\left(1 - \lambda_e^2 \ell_c^2\right)\frac{e\psi}{m_i c} - \left(\frac{1}{\lambda_i \ell_c^2} + \lambda_e\right)\frac{\psi_i}{n} - \Omega r^2 \right] \qquad (30)$$

$$\frac{1}{n}\Delta_n^* \psi_i = \frac{1}{\ell_c^2}\left[\left(\frac{1}{\lambda_i} + \lambda_e \ell_c^2\right)\frac{e\psi}{m_i c} + \left(1 - \frac{1}{\lambda_i^2 \ell_c^2}\right)\frac{\psi_i}{n} - \frac{\Omega}{\lambda_i} r^2 \right] \qquad (31)$$

and a Bernoulli equation for the density (in the isothermal surface case) is

$$\frac{2k(T_i + T_e)}{m_i}\ln n + \frac{|\nabla \psi_i|^2}{n^2 r^2} + \left(\frac{e\psi}{m_i c} - \frac{1}{\lambda_i \ell_c^2}\frac{\psi_i}{n} - \Omega\right)^2 = const \qquad (32)$$

Here $\ell_c = c/\omega_{pi} \propto n^{-1/2}$ is the collisionless skin depth, and $h(n) \equiv k(T_i + T_e)\ln n$. The auxiliary equations that accompany this system are

$$toroidal\ field \qquad \frac{e\phi}{m_i c} = -\lambda_e \frac{e\psi}{m_i c} - \frac{1}{\ell_c^2}\frac{\psi_i}{n} \qquad (33)$$

$$electron\ flow \qquad \frac{\psi_e}{n} = -\lambda_e \ell_c^2 \frac{e\psi}{m_i c}; \qquad \frac{\phi_e}{n} = \lambda_e^2 \ell_c^2 \frac{e\psi}{m_i c} + \lambda_e \frac{\psi_i}{n} + \Omega r^2 \qquad (34,35)$$

$$ion\ flow \qquad \frac{\phi_i}{n} = \frac{e\psi}{m_i c} - \frac{1}{\lambda_i \ell_c^2}\frac{\psi_i}{n} \qquad (36)$$

IV. Discussion of 2D flowing equilibria

These equations are the generalization of the GS system for the case of a flowing two-fluid plasma. The following properties, particularly of minimum energy equilibria stand out. (1) The pressure falls with rising velocity according to the Bernoulli relation (Re Eq. 32): thus a minimum energy state of any kind will have velocity rising toward the plasma edge. (2) The relaxed state of a pure FRC (no toroidal field, $\phi = 0$) with only toroidal flow ($\psi_i = 0$) is likely to have a size scale of order ℓ_c (at most a few times ℓ_c), since $\Delta^* \sim 1/\ell_c^2$ (by inspection of Eq.30). This suggests that such FRCs can only be two-fluid stable if the "s" parameter is limited to values of order unity. (3) However, a pure FRC ($\phi = 0$) may have poloidal flow if it is exactly matched by the poloidal flow of the electrons (cp Eqs. 33,34). In this case the size of the FRC may be somewhat larger than ℓ_c is the terms in square brackets on the right sides of Eqs. 30,31 are small, at least over most of the plasma. This would imply a particular relationship between the magnetic flux function ψ and the ion poloidal flux function ψ_i. If so then large-s FRCs that are two-fluid stable may be possible.

Future work on two-fluid, flowing equilibria will address the following topics. (1) A numerical solver for 2D (r,z) equilibria (both relaxed and partially relaxed) will be developed. The most promising approach to this appears to be the successive over-relaxation technique. These equilibria will then be available to test for stability and other properties. (2) The possibility of intermediate cases between pure FRCs (no toroidal magnetic field) and pure spheromaks (zero beta) can be investigated by adjusting the parameters of a relaxed equilibrium, λ_i, λ_e, and Ω. This may help to resolve the question why in experiments there appears to be a clear bifurcation between FRC and spheromaks.

References

1. L.C. Steinhauer and A. Ishida, Phys. Rev. Lett. **79**, 3423 (1997).

2. L.C. Steinhauer and A. Ishida, Phys. Plasmas **5**, 2609 (1998).

Three-Dimensional Particle Simulation of Tilting Instability in Field-Reversed Configurations

Ritoku Horiuchi, Kazumi Nishimura, and Tetsuya Sato
Theory and Computer Simulation Center,
National Institute for Fusion Science,
Toki 509-52, Japan

Abstract

The kinetic stabilization process of the tilting instability in field-reversed configurations is investigated by means of a three-dimensional particle simulation. For the case of no ion beam the growth rate of tilt instability decreases as the plasma beta value at magnetic separatrix β_{sp} increases. This stabilization effect originates from the character of anchoring ions which exist in the vicinity of the magnetic separatrix and play a role as an "anchor" to hold the internal plasma to the external plasma. The tilt mode is also found to be stabilized by injecting an ion beam with about 20% of the ion thermal energy at the neighborhood of the null point even for small β_{sp} plasmas.

1   Introduction

A field-reversed configuration (FRC) is attractive for a fusion reactor because it has several superior features compared with the representative nominated reactor, e.g., tokamak. For example, there is no structure intersecting plasma torus, a high-beta plasma can be confined by a simple magnetic geometry, and so on. The analysis based on the ideal magnetohydrodynamic (MHD) theory predicts that the FRC plasma will be unstable against the tilt mode if its separatrix shape is prolate [1-3]. However, many experimental observations show that FRC plasmas remain stable much longer than the tilt growth time [4-6]. Many papers have so far tried to explain this contradiction by examining non-ideal MHD effects in FRC plasmas, such as the finite ion Larmor radius (FLR) effect[7, 8], the profile control effect[9, 10], the ion beam effect[11], and so on. However, the contradiction can not be fully solved up to the present. For example, the kinetic simulations[7, 8] have disclosed that the tilt mode can be stabilized for the kinetic plasma of $\bar{s} \approx 1$, but it tends to be unstable as $\bar{s}$ increases. Here, the FLR parameter $\bar{s}$ is defined by

$$\bar{s} = \int_R^{r_s} r dr / (r_s \rho_i), \tag{1}$$

r_s is the separatrix radius, R is the radius of the field null, and ρ_i is the local ion gyroradius. Thus, there remains a big discrepancy between the experiments and the theories in the moderately kinetic plasma of $2 \leq \bar{s} \leq 5$. This paper will discuss the tilt stabilization of

FRC plasmas due to the FLR effect, the current profile control effect, and the ion beam effect, based on the results obtained from a three-dimensional full particle simulation and an MHD simulation.

2   Simulation model

Let us consider the FRC plasma confined by a uniform external magnetic field within the cylindrical conducting vessel with the periodic length $2Z_d$ along the z-axis and the radius R_d. The dynamical evolution of FRC plasmas is solved by making use of the three-dimensional electromagnetic particle simulation code which relies on the semi-implicit scheme[8, 12].

As an initial condition we adopt two-dimensional equilibrium solution which satisfies the equations

$$-\nabla P + \frac{1}{c}\mathbf{j}_d \times \mathbf{B} = 0,$$ (2)

$$\nabla \times \mathbf{B} = \frac{4\pi}{c}(\mathbf{j}_d + \mathbf{j}_b),$$ (3)

where $\mathbf{j}_d$ and $\mathbf{j}_b$ are the diamagnetic component and the beam component of an electric current, respectively, and the pressure profile $P(\Psi)$ is given by[10]

$$P(\Psi) = \begin{cases} P_0(K_0 - \chi - \frac{1}{2}D\chi^2) & \text{for } \chi \le 0 \\ P_0 K_0 e^{-\chi/K_0} & \text{for } \chi > 0, \end{cases}$$ (4)

Ψ denotes the poloidal flux function, $\chi = \Psi/|\Psi_{ax}|$, Ψ_{ax} is the value of Ψ at the field null, P_0 is constant, $K_0 = \beta_{sp}(1-D/2)/(1-\beta_{sp})$, $\beta_{sp}[= P(0)/P(\chi = 1)]$ is the normalized pressure value at the magnetic separatrix, and D is the hollowness parameter. The parameter β_{sp} represents roughly the plasma beta value at the separatrix. The current profile j_θ/r is spatially peaked for $D < 0$, flat for $D = 0$, and hollow for $D > 0$ where j_θ is the azimuthal component of the diamagnetic current density. The initial particle distribution of the diamagnetic component is assumed to be a shifted Maxwellian with a spatially constant temperature. The ion beam with zero temperature is injected along the toroidal (azimuthal) direction near the field null point so that it satisfies the radial force balance equation.

We carry out several simulation runs for a moderately kinetic plasma of $2 \le \bar{s} \le 5$. The important parameters used for the simulation are as follows. The ratio of ion to electron mass m_i/m_e is 50, the aspect ratio of the simulation cylinder $(2Z_d/R_d)$ is 6, and $\omega_{pe}/\omega_{ce} = 5$, where ω_{ce} is the electron cyclotron frequency defined by the magnetic field at the vessel wall on the midplane and ω_{pe} is the electron plasma frequency defined by the density at the field null. In the present model, five parameters can be controlled independently. The first three are the FLR parameter $\bar{s}$, the plasma beta value at magnetic separatrix β_{sp}, and the hollowness parameter D. The ion beam is controlled by the total beam current I_b and the total number of beam ions N_b. In order to compare the particle
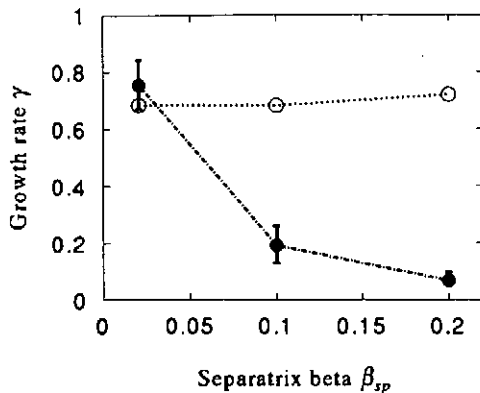
Figure 1: *Dependence of growth rate on separatrix beta for peaked current profiles where* $D = -0.6$, $\bar{s} = 3$. *Open and closed circles correspond to the results obtained from the MHD simulation and the particle simulation, respectively.*
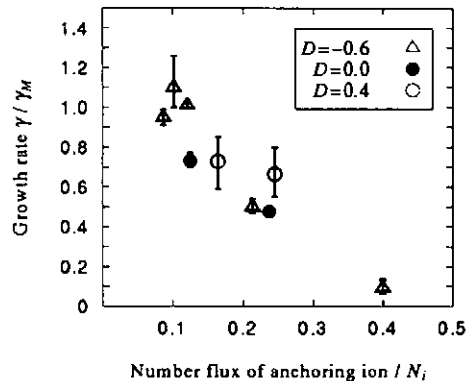
Figure 2: *The tilt growth rate as a function of the number flux of anchoring ions where the kinetic growth rate normalized by the MHD rate is plotted for three different hollowness parameters.*

simulation results with the MHD ones we carry out a three-dimensional MHD simulation which relies on the fourth-order Runge-Kutta-Gill scheme[13].

3   Stabilization by anchoring ions

The dependence of the tilt instability on the parameters $\bar{s}$, D and β_{sp} are examined for the case of no ion beam (I_b, $N_b = 0$). The growth rate of tilt mode is slightly affected by the FLR parameter $\bar{s}$ and the hollowness parameter D[12]. On the other hand, it is found that the growth rate strongly depends on the plasma beta value at magnetic separatrix β_{sp}. The normalized growth rate is plotted as a function of the parameter β_{sp} in Fig. 1 for the case where $\bar{s} = 3$, $D = -0.6$, the growth rate is normalized by the Alfven transit time t_A and the growth rate obtained from the MHD simulation is plotted with open circles for comparison. The initial condition and the boundary condition for the MHD simulation are the same as those for the particle simulation. The kinetic growth rate is almost the same as the MHD one for the case of $\beta_{sp} = 0.01$. The kinetic growth rate decreases as the parameter β_{sp} increases, while the MHD growth rate is almost independent of β_{sp}. Thus, the kinetic stabilization becomes effective for a large β_{sp} plasma ($\beta_{sp} \geq 0.2$). This result indicates that the plasmas in the vicinity of the magnetic separatrix can play an important role in the suppression of the tilt instability. Let us examine the role of gyrating ions crossing the magnetic separatrix repeatedly ("anchoring ions"). The number flux of anchoring ions is found to increase in proportion to β_{sp} where the flux is defined by the total number which times anchoring ions move across the magnetic separatrix in one Alfven time. Figure 2 shows the relationship between the growth rate and the number flux of anchoring ions. The kinetic growth rate decreases
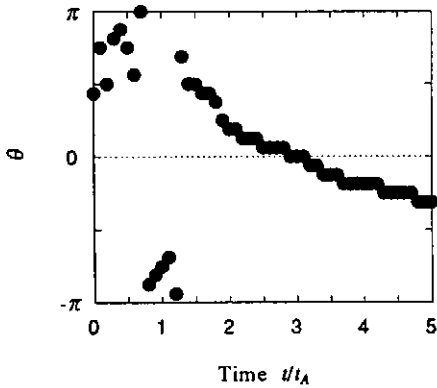
Figure 3: *Temporal evolution of azimuthal angle of tilt mode for the case of $\beta_{sp} = 0.02$ where the parameter θ stands for the azimuthal angle at which the tilt amplitude becomes maximum.*
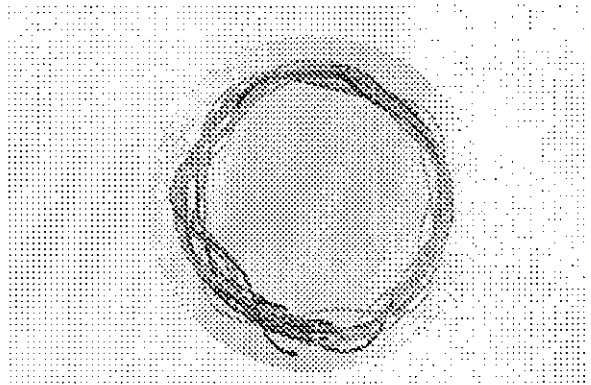

Figure 4: *Top view of five typical orbits of beam ions for the case where $I_b/I_p = 0.022$ and $N_b/N_i = 0.01$. The faint translucent ellipsoid represents the magnetic separatrix.*

with the number flux regardless of the hollowness parameter D. Thus, the tilt stability is realized for a large number flux of anchoring ions.

The kinetic stabilization mechanism by the anchoring ions is as follows. Tilt instability is triggered by the internal mode, i.e., the collective motion of plasma is generated inside the magnetic separatrix. The ions which make a gyrating motion across the separatrix do not follow the collective motion when they are moving outside the separatrix. On the other hand, the unstable internal motion grows while drifting slowly towards the azimuthal direction due to the finite Larmor radius effect, as is shown in Fig. 3. In this way, the phase difference is created between the motion of anchoring ions and the unstable internal motion. When anchoring ions come back inside the separatrix, the internal tilting motion is disturbed by the motion of anchoring ions. The stabilization effect by anchoring ions becomes more effective as the number flux increases. Consequently, the tilt stability is realized for a large beta at the separatrix ($\beta_{sp} \geq 0.2$). In other words, the anchoring ions play a role as an "anchor" to hold the internal plasma to the external plasma, thus stabilizing the tilting motion through their "anchor" effect.

4 Stabilization by ion beam

The beam stabilization effect for small β_{sp} plasmas is examined by controlling the total beam current I_b in two ways[14]. First by changing the beam particle number while keeping the beam velocity nearly equal to 3.0 of the thermal ion velocity, and the other by changing the beam particle velocity while keeping the beam particle number equal to 0.01 of total number of thermal ions. The typical orbits of beam ions are shown in Fig. 4 for the case of $I_b/I_p = 0.022$ and $N_b/N_i = 0.01$, where I_p and N_i are the total current of thermal plasmas and the total number of thermal ions, respectively. It is clearly seen in
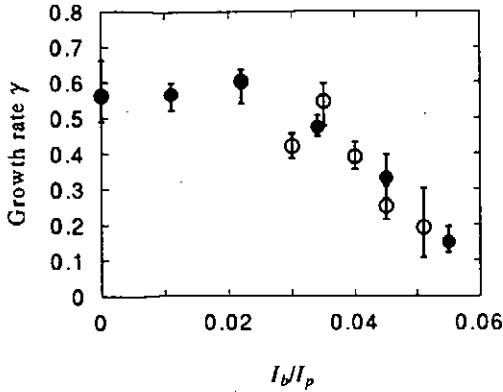
Figure 5: *Dependence of growth rate on the beam current I_b for the cases where the beam number is changed (closed), and the cases where the beam velocity is changed (open).*
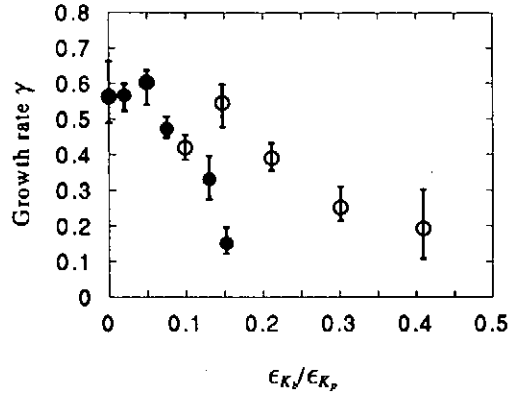
Figure 6: *Dependence of growth rate on the energy ratio of beam ions to thermal ions $\epsilon_{K_b}/\epsilon_{K_p}$ for the same cases as Fig. 5.*

Fig. 4 that the stable orbit of beam ions exists in the vicinity of the magnetic separatrix and undergoes the small oscillation in the radial direction.

Figure 5 shows the dependence of growth rate on the total beam current I_b for the case where $D = -0.6$, $\bar{s} = 3$, $\beta_{sp} = 0.02$. For both cases the growth rate remains almost unchanged until the beam current reaches a critical value ($I_b < 0.03I_p$). The growth rate gradually decreases as the beam current increases above the critical value. Figure 6 shows the dependence of growth rate on the ratio of beam ions to thermal ions energy $\epsilon_{K_b}/\epsilon_{K_p}$ for the same cases as Fig. 5. For the cases where the beam velocity is changed (open circles), the tilt stabilization is realized when the beam energy is about 50% of the ion thermal energy. For the cases where the beam number is changed (closed circles), the tilt stabilization is realized when the beam energy is about 20% of the ion thermal energy.

It is concluded that the beam stabilization effect is evaluated in terms of the beam current, and the effective stabilization with a relatively small beam energy is realized by controlling the total number of beam ions.

5 Conclusions

We have investigated the tilt stabilization mechanism of FRC plasmas by means of a three-dimensional particle simulation and an MHD simulation. The tilt stabilization in the moderately kinetic regime ($2 \leq \bar{s} \leq 5$) is attributable mainly to the character of anchoring ions which exist in the vicinity of the magnetic separatrix and play a role as an "anchor" to hold the unstable internal plasma to the stable external plasma. The beam stabilization effect is evaluated in terms of the beam current, and the effective stabilization with a relatively small beam energy, i.e., about 20% of ion thermal energy, is realized by controlling the total number of beam ions even for small β_{sp} plasmas.

References

[1] W. N. Rosenbluth, and M. N. Bussac, Nucl. Fusion **19**, 489 (1979).

[2] J. H. Hammer, Nucl. Fusion **21**, 488 (1981).

[3] R. A. Clemente and J. L. Milovich, Phys. Letters **85A**, 148 (1981).

[4] M. Tuszewski, Nucl. Fusion **28**, 2033 (1988).

[5] J. T. Slough and A. L. Hoffman, Nucl. Fusion **28**, 1121 (1988).

[6] J. T. Slough, A. L. Hoffman, R. D. Milroy, R. Maqueda, and L. C. Steinhauer, Phys. Plasmas **2**, 2286 (1995).

[7] D. C. Barnes, J. L. Schwarzmeier, R. Lewis, and C. E. Seyler, Phys. Fluids **29**, 2616 (1986).

[8] R. Horiuchi and T. Sato, Phys. Fluids **B 2**, 2652 (1990).

[9] L. C. Steinhauer and A. Ishida, Phys. Fluids **B 4**, 645 (1992).

[10] J. W. Cobb, T. Tajima, and D. C. Barnes, Phys. Fluids **B 5**, 3227 (1993).

[11] D. C. Barnes and R. D. Milroy, Phys. Fluids **B 3**, 2609 (1991).

[12] K. Nishimura, R. Horiuchi and T. Sato, Phys. Plasmas **4**, 4035(1997).

[13] R. Horiuchi and T. Sato, Phys. Fluids **B 1**, 581 (1989).

[14] R. Horiuchi, K. Nishimura and T. Sato, Nucl. Fusion, (1999) [to be published].

Turbulence of High-Beta Plasma

V.I. Khvesyuk and A.Yu. Chirkov

Bauman Moscow State Technical University, Power Engineering Institute,
P.O. Box 38, 105007, Moscow, Russia

Abstract.

Principals of numerical modelling of turbulence in high-beta plasma ($\beta > 0.1$) are discussed. Creation of transport model for axial symmetric nonuniform confining magnetic field is considered. Numerical model of plasma turbulence in FRC is presented. The physical and mathematical models are formulated from nonuniform axial symmetric high-beta plasma. It is shown that influence of waves arise under this plasma conditions lead to chaotic motion of charged particles across magnetic field.

1. Introduction.

In this work we consider principals of numerical modelling of turbulence in high-beta plasma ($\beta > 0.1$). This problem arises for FRC, Tandem Mirror and other magnetic systems confining high-beta plasma.

High-beta plasma has a number of features in comparison with low-beta plasma. It is well-known for high-beta plasma it is necessary to take into account nonuniformity of plasma density, plasma temperature and magnetic field [1]. Investigations of microinstabilities inside a such plasma show the possibilities of arising of following modes [1]: Tserkovnikov and Alfven waves, low-hybrid, low-frequency and ion-cyclotron waves. But increasing plasma beta leads to suppression of some modes of oscillations [1]. Consequently careful analysis of possible microinstabilities for every concrete conditions is required. Here we do not consider this problem but discuss some features of anomalous transport. In this work the method of numerical analysis of the transport processes inside nonuniform high-beta plasma ($\beta > 0.1$) induced by microinstabilities is discussed. The simple examples are considered.

The important example of considered nonuniform plasma conditions is FRC plasma. In Fig. 1 the radial distributions of the plasma pressure and plasma beta for Hill's vortex (in plane $z=0$) are plotted. One can see strong nonuniformity and big values of beta. Naturally in real experimental situations these distributions differ on plotted in Fig. 1. But indicated features are true in any case.

We consider the axial cylindrical radial nonuniform plasma with magnetic field $B(r)$ directed along axis of symmetry (z-axis). The electrostatic and electromagnetic waves propagate inside plasma in azimuthal and longitudinal directions.

In order to estimate numerical values of diffusion coefficient based on [2,3] method developed in [5,4] was used. We derived a set of non-linear equations describing motion of particles under influence of electric field of wave inside axial symmetric trap. Therefore we can

estimate the confinement time for a plasma inside magnetic trap. Preliminary calculations show good agreement between theoretical and experimental data.

Detail investigations also indicate another scenario of radial transport. If oscillations are long-wave and the electric field of the wave is parallel to the wave vector, then it is possible convective losses of the particles across the magnetic field. In this case the particles accomplish the electric drift in the radial direction under the influence of the magnetic field of the trap and the electric field of the wave. This motion is not stochastic, but in this case lines in phase plane directed to plasma boundary are exists.

Therefore numerical calculations allow to investigate the important features of radial transport inside axial symmetric magnetic trap and separate convective and turbulent transport.

$$\beta = \frac{1 - \left(1 - 2\frac{r^2}{R_s^2}\right)^2}{\left(1 - 2\frac{r^2}{R_s^2}\right)^2}$$
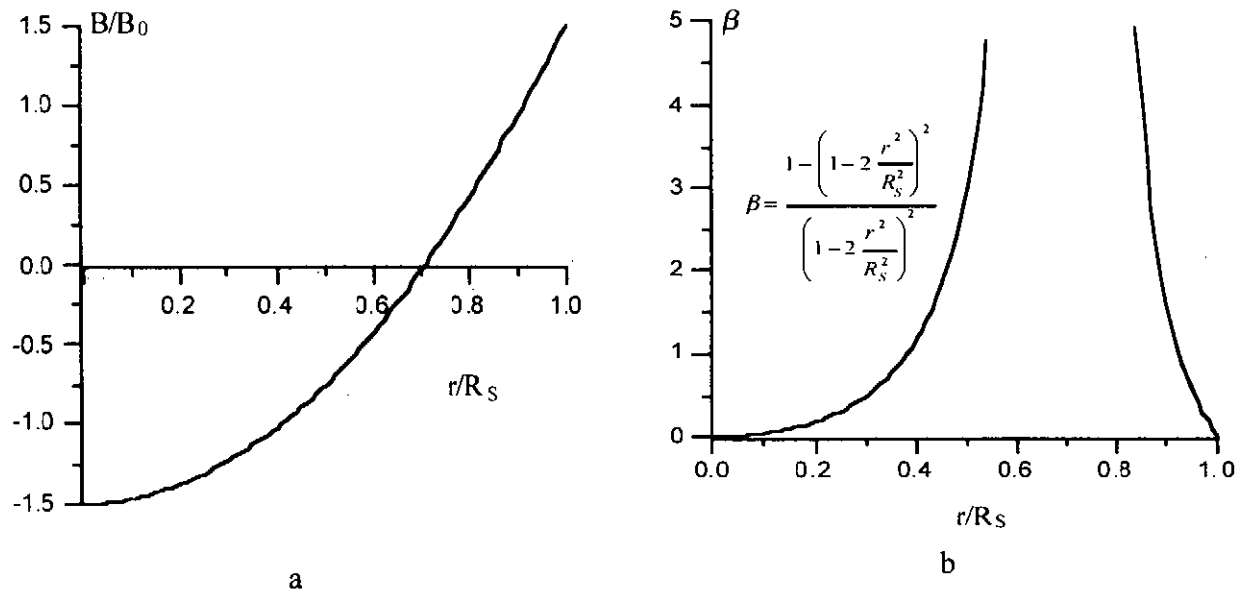
a

b

Fig. 1. Magnetic field (a) and beta (b) distributions for Hill's vortex FRC.

2. Microinstabilities and anomalous transport in nonuniform plasma.

The anomalous transport is a result of simultaneous joint influence on the particles of the static magnetic field and the propagating waves fields. This results is complex particles motion across magnetic field. Solution of this problem allows to estimate the anomalous transport properties of the plasma.

Analysis shows it is non-linear problem. The main parameters determining results of numerical solution are as follows:
- drift frequency of the particles in the static nonuniform magnetic field;
- speed and direction of propagation of waves;
- frequency, magnitude and polarisation of electromagnetic waves.

Investigations [1,6] have shown the most probable oscillations inside the nonuniform high-beta plasma are:
- low frequency oscillations ($\omega \ll \Omega_i$, where ω is the wave frequency, Ω_i is the ion-cyclotron frequency);

- ion-cyclotron oscillations $(\omega\!-\!\Omega_i)$;
- low-hybrid instabilities;
- Tserkovnikov waves;
- Alfven instabilities;
- oscillations, induced by transversal current.

The features of waves propagation depends on different parameters, such as magnetic field B and ∇B, plasma temperature T and ∇T, plasma density n and ∇n, $k_\perp \rho_e$ and $k_\perp \rho_i$ ($k_\perp$ is perpendicular to magnetic field component of wave vector, ρ_e and ρ_i are electron and ion Larmor radiuses), etc. Analysis of microinstabilities allows to define characteristics of oscillation modes for different regions of nonuniform plasma.

3. Non-linear analysis of charged particles dynamics under influence of wave.

We consider cylindrical configuration, where magnetic field $B(r)$ directed along axis z and depends on radius r. Gradient dB/dr has radial direction. Electric field of the wave $E(r,\theta,t)$ in our model is azimuthal and depends on co-ordinates as

$$E(r,\theta,t) = \frac{\phi_0}{r}\sin(\omega_0 t - k_\theta \theta), \tag{1}$$

where ϕ_0 is corresponding potential amplitude ω_0 is the wave frequency, k_θ is azimuthal wave number. We consider wave mode with $k_\theta=1$. Value of wave potential amplitude usually can be estimated as $e\phi_0 \sim kT$.

To obtain particles trajectories in (r,θ) co-ordinates we use dynamics equations

$$\frac{dv_r}{dt} = -\frac{qB(r)}{m}v_\theta, \tag{2a}$$

$$\frac{dv_\theta}{dt} = \frac{qB(r)}{m}v_r + \frac{q}{m}E(r,\theta,t), \tag{2b}$$

where m and $q=Ze$ are particle mass and charge correspondingly, $v_r=dr/dt$ and $v_\theta=rd\theta/dt$.

To obtain model of stochastic diffusion we consider influence of low frequency electrostatic wave on particle motion. In this case ω_0 more less then frequency of synchrotron rotation of the particle. Consequently guiding center approach to particle motion can be used. Equations for guiding center motion in cylindrical geometry in system, connected with wave and rotating with frequency ω_0, are

$$\frac{d\alpha}{dt} = \omega_{dr}(r) - \omega_0, \tag{3a}$$

$$\frac{dr}{dt} = \frac{\phi_0}{B(r)r}\sin\alpha, \tag{3b}$$

where α is angular co-ordinate,

$$\omega_{dr}(r) = \frac{\varepsilon_\perp}{qrB^2} \frac{dB}{dr} \qquad (4)$$

is gradient drift frequency, $\varepsilon_\perp = m(v_r^2 + v_\theta^2)/2$. In order to stochasticity in particle motion can appear, drift frequency and wave frequency mast satisfy resonance condition

$$\omega_{dr} = n\omega_0, \quad n = 1,2,3,\dots \qquad (5)$$

Radial locations of resonance drift surfaces r_n ($n=1,2,3,\dots$) are defined by (4) and (5).
We used new variable

$$X = \frac{q}{\varepsilon_\perp} \int_r^{r_l} B(r)r\,dr, \qquad (6)$$

where r_l is radius of the nearest to separatrix resonance surface in close lines region (l is number of the surface). This variable transforms system (3) to non-linear pendulum like [2,3] equations

$$\frac{d\alpha}{dt} = AX, \qquad (7a)$$

$$\frac{dX}{dt} = -C\sin\alpha, \qquad (7b)$$

where

$$C = \frac{q\phi_0}{\varepsilon_\perp}\omega_0, \qquad (8)$$

$$A = \omega_0 \frac{\left.\dfrac{d\ln|B|}{dX}\right|_{X(r_l)} - \left.\dfrac{d\ln|B|}{dX}\right|_{X(r)}}{X} \approx \frac{\omega_0}{4}. \qquad (9)$$

After these transformations it is easy to obtain phase planes of system (7) and consequently system (3) by standard mapping [7]. For variables α and $I = AT_0X$, where $T_0 = 2\pi/\Delta\omega$ is the iteration time, $\Delta\omega$ is interval between resonance frequencies standard mapping is

$$\overline{I} = I + K_0 \sin\alpha, \qquad (10a)$$

$$\overline{\alpha} = \alpha + \overline{I}, \qquad \mathrm{mod}(2\pi), \qquad (10b)$$

where $\overline{\alpha}$ and $\overline{I}$ are values of α and I at new iteration,

$$K_0 = ACT_0^2 = 4\pi^2 \frac{AC}{(\Delta\omega)^2}$$ (11)

is Chirikov's coefficient. In case $K_0 > 1$ significant stochasticity take place. In considering case $\Delta\omega = \omega_0$ and

$$K_0 = \pi^2 \frac{q\phi_0}{\varepsilon_\perp}.$$ (12)

In case of wave potential amplitude estimated as $q\phi_0 \sim kT$ Chirikov's criterion value is

$$K_0 = \pi^2 \frac{kT}{\varepsilon_\perp}.$$ (13)

For majority of plasma particles $\varepsilon_\perp \sim kT$ and, as Eq. (13) shows, $K_0 \sim 10$. Consequently their motion is significantly stochastic in case of action of considered low frequency electrostatic wave.

Presented above analysis was carried out for general form of magnetic field distribution. Examples of phase plans in (r, α) co-ordinates for different value K_0 are plotted in Fig. 2 for Hill's vortex FRC.

In Fig. 2 change of the nature of the particles motion for increasing magnitude of wave is shown. The important feature of these drawings is the presence of resonance surfaces between magnetic drift frequency of the particles and wave rotation frequency around the axis of the magnetic system. In Fig. 2a shift of the particles in radial direction is restricted by some distance in the vicinity of a resonance surface. This distance is less than distance between neighbouring resonance surfaces. In Fig. 2b the areas of excited motion are overlapped. In this case motion of particles becomes stochastic in whole considered space field. Corresponding particles can move freely in this field and leave the plasma. These conditions corresponds to turbulent transport inside plasma. Example of particle trajectory is plotted in Fig. 3.
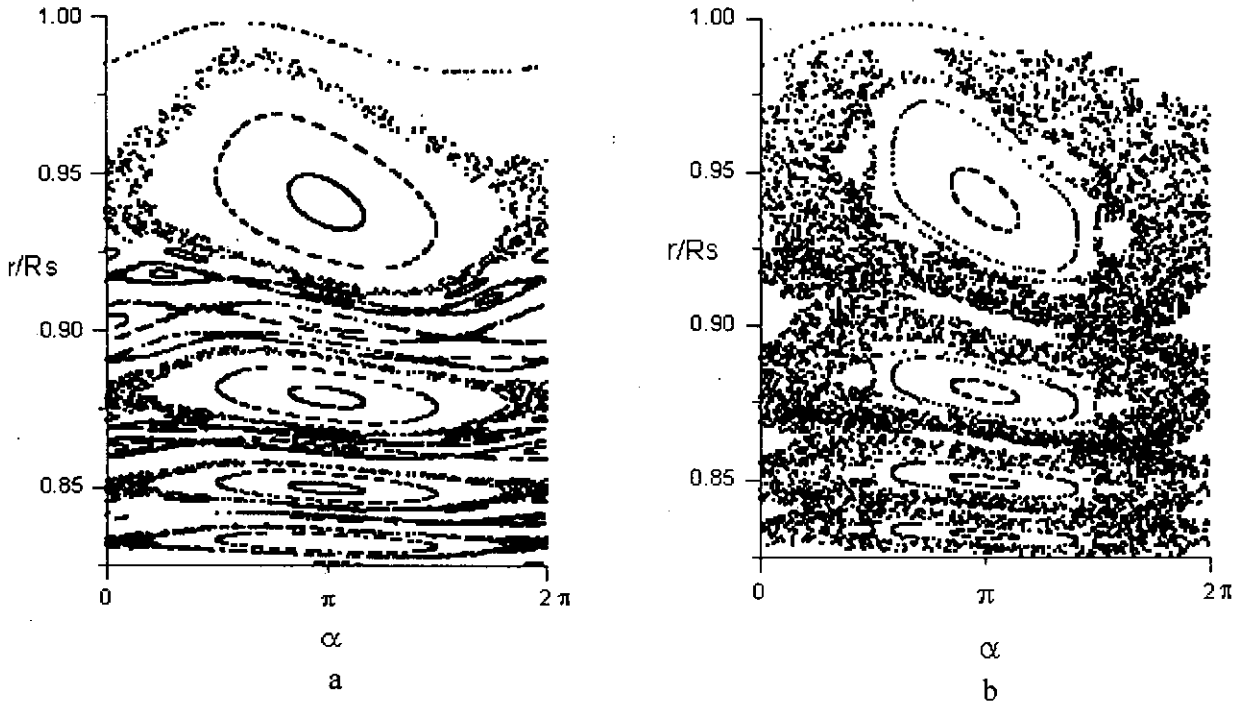
Fig. 2. Phase planes for particles in FRC plasma with magnetic field $B_0=1$ T, separatrix radius $R_s=0.5$ m, wave frequency $\omega_0=4\times10^7$ rad/s for $K_0=1$ (a) and $K_0=2$ (b).

4. Stochastic Diffusion Coefficient.

For $K_0 \gg 1$ motion in phase plane can be considered as diffusion process. Corresponding stochastic radial diffusion coefficient is [7]

$$D_r = \frac{1}{\pi}\Delta\omega(\Delta r)_m^2, \tag{14}$$

where $(\Delta r)_m$ corresponds to coefficient $\phi_0/B(r)r$ in Eq. (3b).

Similarly [4,5] for conditions $q\phi_0 \sim kT$, $l=1$ we obtain averaged value of diffusion coefficient

$$D_r \approx \frac{1}{5}\frac{kT}{qB}, \tag{15}$$

where T is the overaged value of plasma temperature, B is characteristic value of magnetic field (for example, value at the separatrix).

Comparison corresponding stochastic diffusion time

$$\tau_{SD} = \frac{R_s^2}{D_r} = \frac{5qBR_s^2}{kT} \tag{16}$$

with experimental data [8] for particles confinement times τ_P are presented in Fig. 4. Obtained τ_{SD} depends on B, T and R_s similarly to presented in [6] confinement time.
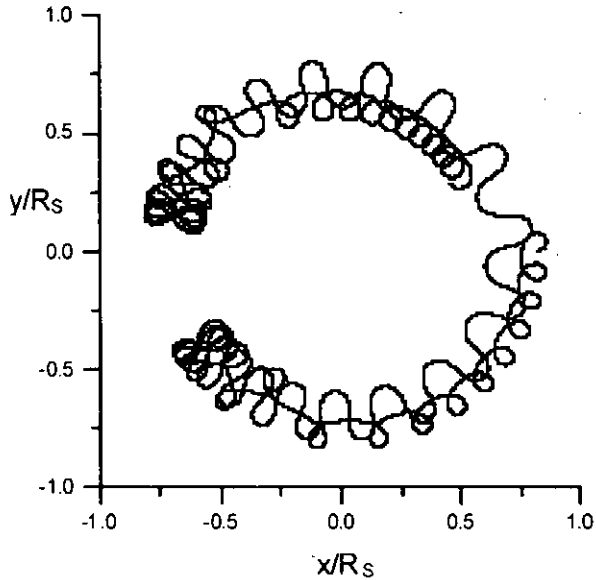

Fig. 3. Fragment of proton trajectory in Hill's vortex FRC $(B_0=1\ T,\ \varepsilon_\perp=10\ keV)$.
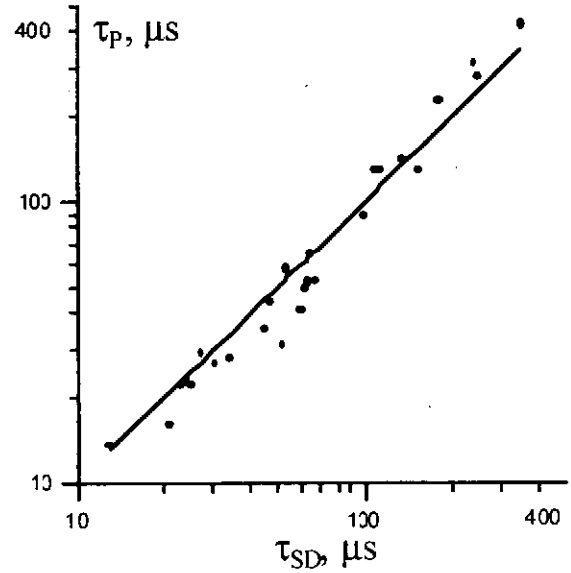
Fig. 4. Comparison between experimental data and theoretical results.

5. Conclusions.

As carried out above analysis shown, in nonuniform high-beta plasma non-linear interaction between particles and waves can induce strong turbulence and influence on particles motion and transport. Therefore problem of calculations of transport processes must include following stages.

1. Analysis of possible modes of microinstabilities for nonuniform plasma ($\beta>0.1$), including nonuniformity both magnetic field and plasma density and temperature.

2. Numerical calculations of stochastic motion of particles for axial symmetric magnetic field taking into account azimuthal electrostatic and electromagnetic waves, including non-linear complex interactions between waves and particles. This analysis allows to separate "clean" turbulent transport and convective transport. These tasks demand non-linear consideration, taking into account resonance processes including overlap of the resonance areas.

References.

1. Mikhailovsky, Theory of Plasma Instabilities, v.2 Instabilities of Nonuniform Plasma, Atomizdat, Moscow, (1977)

2. Zaslavsky, R.Z. Sagdeev, Introduction to Non-linear Physics. From Pendulum to Turbulence and Chaos, Nauka, Moscow (1988)

3. Lichtenberg, M.A. Lieberman, Regular and Stochastic Motion, Springer-Verlag, New York (1983)

4. Shabrov, V.I. Khvesyuk, A.N. Lyakhov, in Int. Conf. on Open Plasma Confinement Systems for Fusion (Novosibirsk, 1993), Ed. A.A. Kabantsev, World Scientific, Singapore - New Jersey - London - Hong Kong, p. 245

5. Khvesyuk, N.V. Shabrov, Russian Technical Physics Letters, v.19, 1 (1994)

6. N.A.Krall, Phys. Fluids, v. B1, 1811 (1989)

7. B.V. Chirikov, in Revews of Plasma Physics, Ed. B.B. Kadomtsev, v. 13, p. 3, Energoatomizdat, Moscow, (1984)

8. L. Steinhauer, FRC Data Digest, US - Japan Workshop, (Niigata, 1996), unpublished

Distribution Function of Plasma Particles in the Edge Region of an FRC

Toshiki Takahashi, Yoshiomi Kondoh, and Hiromu Momota [†]

Department of Electronic Engineering, Gunma University, Kiryu, Gunma 376-8515, Japan
†Department of Nuclear Engineering, University of Illinois at Urbana-Champaign, Urbana, Illinois 61801-2984, U.S.A.

The particle transport in a Field-Reversed Configurations (FRCs) is a one of important issues to study for a realization of the fusion reactor with Deuterium-Helium 3 (D-^{3}He) fuels. The particle transport has been often studied with a use of MHD. By some experiments, however, FRCs have been found to be stable to the tilt instability, which is unstable according to the MHD prediction. Therefore FRCs show the kinetic feature and should be discussed by the kinetic theory. Since the particles near the separatrix are able to reach the mirror points and suffer the consequent mirror loss, those kinetic properties are worthy to study. Our previous work [*)] showed the adiabaticity breaking process of edge region particles at the field null x-points. This phenomena may enhance the particle loss from an FRC. Due to the complicated form of the rate of the statistical change in the pitch angle, it is the hard task to include its effect in the kinetics. As the first step, the classical transport for the particles in the edge region is investigated in the present work.

The kinetic equation for the classical particle transport is expressed in the form:

$$\left(\frac{\partial}{\partial t} + \boldsymbol{v} \bullet \nabla - \frac{q}{M}\boldsymbol{F}(\boldsymbol{r}, t) \bullet \nabla_v\right)f(\boldsymbol{r}, \boldsymbol{v}, t) - \frac{q}{M}\langle\boldsymbol{\delta F}(r(t), t)\rangle \bullet \nabla_v f(\boldsymbol{r}, \boldsymbol{v}, t)$$

$$- \nabla_v \bullet \left(\frac{q}{M}\right)^2 \int_0^{\infty} \langle\boldsymbol{\delta F}(r(t), t)\boldsymbol{\delta F}(r(t - \tau), t - \tau)\rangle d\tau \bullet \nabla_v f(\boldsymbol{r}, \boldsymbol{v}, t) = 0, \quad (1)$$

where the second and the third terms relate to interparticle collisions. The zeroth order equation to collisions describing the plasma in an axisymmetric steady state; $\partial/\partial t = 0$ and $\partial/\partial\theta = 0$, can be expressed in terms of constants of motions:

$$H = W + q\phi, \quad \text{and} \quad P_\theta = Mrv_\theta + q\psi. \quad (2)$$

We introduce two spacial coordinates, i.e., the flux function ψ and the stream function χ defined by

$$\psi \equiv \int_{r'=0}^{r} r'B_z(r', z)dr', \qquad \chi \equiv \int_{z'=0}^{z} rB_z(r, z')dz'. \quad (3)$$

We define also the radial action integral J by the equation:

$$J \equiv \frac{1}{2\pi}\int_{t_1}^{t_2} P_r dr \qquad P_r(t_1) = P_r(t_2), \quad t_1 < t_2 \quad (4)$$

Thus we obtain the zeroth order equation to collisions:

$$\left(\frac{d\psi}{dt}\frac{\partial}{\partial\psi} + \frac{d\chi}{dt}\frac{\partial}{\partial\chi} + \frac{dJ}{dt}\frac{\partial}{\partial J} + \frac{dP_\theta}{dt}\frac{\partial}{\partial P_\theta} + \frac{dH}{dt}\frac{\partial}{\partial H}\right)f(\psi, \chi, J, P_\theta, H) = 0 \quad (5)$$

Since the canonical angular momentum P_θ and the Hamiltonian H are the constants of motion, the last two terms in the bracket of the above equation vanish. We have studied further that the action integral J keeps its value during an excursion between field-null x-points. Thus we have the zeroth order equation in the form:

$$\left(\frac{d\psi}{dt}\frac{\partial}{\partial\psi} + \frac{d\chi}{dt}\frac{\partial}{\partial\chi}\right)f(\psi,\chi,J,P_\theta,H) = 0. \tag{6}$$

The general solution to the zeroth order equation becomes $f(\psi - \frac{d\psi/dt}{d\chi/dt}\chi, J, P_\theta, H)$. By defining the time average as

$$\bar{Q} \equiv \frac{1}{t_2 - t_1}\int_{t_1}^{t_2} Q(t')dt', \qquad Q(t_2) = Q(t_1), \tag{7}$$

the distribution function reduces to

$$
\begin{aligned}
\overline{f(\psi - \frac{d\psi/dt}{d\chi/dt}\chi, J, P_\theta, H)} &= f(\bar{\psi}, J, P_\theta, H) + \overline{\left(\psi - \bar{\psi} - \frac{d\psi/dt}{d\chi/dt}\chi\right)}\frac{\partial f}{\partial\psi}(\bar{\psi}, J, P_\theta, H) \\
&= f(\bar{\psi}, J, P_\theta, H).
\end{aligned} \tag{8}
$$

Therefore, the zeroth order distribution function is uniform along the magnetic lines of force.

The linearized Landau form is employed for the next order kinetic equtation, which is expressed as

$$
\sum_s \frac{n_s q_j^2 q_s^2}{8\pi\varepsilon_0^2 M_j^2}\lambda\left(\frac{M_j}{2W}\right)^{3/2}\left\{\left(2T_s\frac{M_j}{M_s}\right)W\frac{\partial}{\partial W}\left[\eta(x)\left(\frac{\partial}{\partial W} + \frac{1}{T}\right)\right] +
\right.
$$
$$
\left.
\frac{(1 - 1/2x)\eta(x) + \eta'(x)}{\cos^2\theta_p} \times \left[\cos\theta_p\frac{\partial}{\partial\theta_p}\cos\theta_p\frac{\partial}{\partial\theta_p} + \frac{\partial^2}{\partial\varphi^2}\right]\right\}f^j(r,z,W,\theta_p,\varphi) = 0, \tag{9}
$$

where

$$W \equiv \frac{M_j V^2}{2} \qquad x \equiv \frac{M_s W}{M_j T_s} \qquad \eta(x) \equiv \frac{2}{\sqrt{\pi}}\int_0^x t^{1/2}\exp(-t)dt.$$

Defining the kinetic part of the canonical angular momentum as $\rho = \sqrt{r^2 M}\sqrt{2W}\cos\theta_p\sin\varphi$, the ensemble average in terms of the gyro-phase will be

$$\langle\rho\rangle \equiv M\langle rV_\theta\rangle \approx 0 \qquad \langle\rho^2\rangle = r^2 M_j W\cos^2\theta_p.$$

When ρ changes due to collisions, the particles suffer the cross field diffusion. This is expressed by the following substitution.

$$\frac{\partial}{\partial\rho} \longrightarrow \frac{1}{q}\frac{\partial}{\partial\psi} \tag{10}$$

Then we easily obtain the transport equation for ions as

$$
\left\{\frac{q^2}{8\pi\varepsilon_0^2}\frac{\lambda}{2W\sqrt{2WM}}n_i q^2 \times 2TW\frac{\partial}{\partial W}\left[\eta(x)\left(\frac{\partial}{\partial W} + \frac{1}{T}\right)\right] +
\right.
$$
$$
\frac{q^2}{8\pi\varepsilon_0^2}\frac{\lambda}{2W\sqrt{2WM}}n_i q^2\left[(1 - 1/2x)\eta(x) + \eta'(x)\right]\frac{1}{\cos\theta_p}\frac{\partial}{\partial\theta_p}\cos\theta_p\frac{\partial}{\partial\theta_p} +
$$
$$
\left.
\frac{q^2}{8\pi\varepsilon_0^2}\frac{\lambda}{2W\sqrt{2WM}}n_e e^2\sqrt{\frac{m}{MT}}\sqrt{W}\frac{2}{3\sqrt{\pi}}\left(\frac{4}{\cos^2\theta_p} - 1\right)\frac{r^2 MW\cos^2\theta_p}{q^2}\frac{\partial^2}{\partial\psi^2}\right\} \times f^i(W,\theta_p,\psi)
$$
$$
= 0 \tag{11}
$$

-28-

One can get the equation for electrons in the form:

$$\left\{ \frac{e^2}{8\pi\varepsilon_0^2} \frac{\lambda}{2W\sqrt{2Wm}} n_e e^2 \times 2TW \frac{\partial}{\partial W}\left[\eta(x)\left(\frac{\partial}{\partial W} + \frac{1}{T}\right)\right] + \right.$$

$$\frac{e^2}{8\pi\varepsilon_0^2} \frac{\lambda}{2W\sqrt{2Wm}} n_e e^2 \left[(1 - 1/2x)\eta(x) + \eta'(x)\right] \frac{1}{\cos\theta_p} \frac{\partial}{\partial\theta_p} \cos\theta_p \frac{\partial}{\partial\theta_p} +$$

$$\left. \frac{e^2}{8\pi\varepsilon_0^2} \frac{\lambda}{2W\sqrt{2Wm}} n_i q^2 \left(\frac{2}{\cos^2\theta_p} - 1\right) \frac{r^2 m W \cos^2\theta_p}{e^2} \frac{\partial^2}{\partial\psi^2}\right\} \times f^e(W, \theta_p, \psi) = 0 \quad (12)$$

The particles near the separatrix can pass through the mirror points. Without the electrostatic potential, the loss cone is formed in the velocity space. In this case electrons will be lost away rapidly compared to ions. To satisfy the ambipolarity of plasma, the negative potential will be formed around the mirror points. Consequently, the boundary of loss region becomes hyperbolic curve such as

$$v_\parallel^2 - (R-1)v_\perp^2 = -\frac{2e\phi_{mir}}{m} = \alpha^2 \qquad : \text{for electrons,}$$

$$v_\parallel^2 - (R-1)v_\perp^2 = \frac{2q\phi_{mir}}{M} = -\beta^2 \qquad : \text{for ions.} \qquad (13)$$

We assume that inside the loss region the distribution function is set to be zero. For the convenience of the calculation, we had better use the other variables, x and y, so as to fit the boundary condition. If we transform the variables in the form:

$$v_\perp = \sqrt{\frac{R}{R-1}}\alpha \sinh x \sin y,$$

$$v_\parallel = \sqrt{\frac{R}{R-1}}\alpha \cosh x \cos y \qquad : \text{for electrons,}$$

$$v_\perp = \sqrt{\frac{R}{R-1}}\beta \cosh x \cos y,$$

$$v_\parallel = \sqrt{\frac{R}{R-1}}\beta \sinh x \sin y \qquad : \text{for ions,} \qquad (14)$$

the kinetic equations becomes

$$L^e(x,y)f^e(x,y,\psi) + h^e(x,y)\frac{r^2 m^2 R\alpha^2}{2e^2(R-1)}\frac{\partial^2}{\partial\psi^2}f^e(x,y,\psi) = 0,$$

$$L^i(x,y)f^i(x,y,\psi) + h^i(x,y)\frac{r^2 M^2 R\beta^2}{2q^2(R-1)}\frac{\partial^2}{\partial\psi^2}f^i(x,y,\psi) = 0, \qquad (15)$$

where,

$$L^e(x,y) = \frac{1}{\cosh^2 x - \cos^2 y}\left(\sinh x \cosh x \frac{\partial}{\partial x} - \sin y \cos y \frac{\partial}{\partial y}\right)$$

$$\cdot \left\{\frac{(R-1)T}{mR\alpha^2(\cosh^2 x - \sin^2 y)(\cosh^2 x - \cos^2 y)}\left(\sinh x \cosh x \frac{\partial}{\partial x} - \sin y \cos y \frac{\partial}{\partial y}\right) + 1\right\}$$

$$+\frac{\sqrt{\cosh^2 x - \sin^2 y}}{\sinh x \sin y(\cosh^2 x - \cos^2 y)}\left(\sin y \cos y \frac{\partial}{\partial x} + \sinh x \cosh x \frac{\partial}{\partial y}\right)$$

$$\cdot\frac{\sinh x \sin y}{\sqrt{\cosh^2 x - \sin^2 y}(\cosh^2 x - \cos^2 y)}\left(\sin y \cos y \frac{\partial}{\partial x} + \sinh x \cosh x \frac{\partial}{\partial y}\right), \tag{16}$$

$$L^i(x,y) = \frac{1}{\cosh^2 x - \cos^2 y}\left(\sinh x \cosh x \frac{\partial}{\partial x} - \sin y \cos y \frac{\partial}{\partial y}\right)\cdot$$

$$\cdot\left\{\frac{(R-1)T}{MR\beta^2(\cosh^2 x - \sin^2 y)(\cosh^2 x - \cos^2 y)}\left(\sinh x \cosh x \frac{\partial}{\partial x} - \sin y \cos y \frac{\partial}{\partial y}\right) + 1\right\}$$

$$+\frac{\sqrt{\cosh^2 x - \sin^2 y}}{\cosh x \cos y(\cosh^2 x - \cos^2 y)}\left(\sin y \cos y \frac{\partial}{\partial x} + \sinh x \cosh x \frac{\partial}{\partial y}\right)$$

$$\cdot\frac{\cosh x \cos y}{\sqrt{\cosh^2 x - \sin^2 y}(\cosh^2 x - \cos^2 y)}\left(\sin y \cos y \frac{\partial}{\partial x} + \sinh x \cosh x \frac{\partial}{\partial y}\right), \tag{17}$$

$$h^e(x,y) = 2\cosh^2 x - 2\sin^2 y - \sinh^2 x \sin^2 y,$$

$$h^i(x,y) = \frac{2}{3\sqrt{\pi}}\sqrt{\frac{mR\beta^2}{2(R-1)T}}\sqrt{\cosh^2 x - \sin^2 y}(4\cosh^2 x - 4\sin^2 y - \cosh^2 x \cos^2 y). \tag{18}$$

Since one can separate the variables in Eq. (16), the distribution is set in the form:

$$f(x,y,\psi) \equiv cg(x,y)\Psi(\psi). \tag{19}$$

The solution to Eq. (16) for the real space part is obtained as

$$\Psi^e(\psi) = \exp\left\{-\sqrt{\frac{2(R-1)e^2\kappa_e^2}{r^2m^2R\alpha^2}}|\psi|\right\},$$

$$\Psi^i(\psi) = \exp\left\{-\sqrt{\frac{2(R-1)q^2\kappa_i^2}{r^2M^2R\beta^2}}|\psi|\right\}. \tag{20}$$

The number density calculated from the integration of the distribution function in the velocity space is normalized to be equal to the number density at $\psi = 0$. Therefore,

$$n_0 = n_{i0} = n_{e0}$$

$$= \int_0^\infty \int_0^{\sin^{-1}\sqrt{\frac{R-1}{R}}} c_i g^i(x,y)\mathcal{D}^i dx dy = \int_0^\infty \int_{\cos^{-1}\sqrt{\frac{R-1}{R}}}^{\frac{\pi}{2}} c_e g^e(x,y)\mathcal{D}^e dx dy, \tag{21}$$

where,

$$\mathcal{D}^i = 2\pi\left(\frac{R}{R-1}\right)^{3/2}\beta^3 \sinh x \sin y(\cosh^2 x - \cos^2 y),$$

$$\mathcal{D}^e = 2\pi\left(\frac{R}{R-1}\right)^{3/2}\alpha^3 \cosh x \cos y(\cosh^2 x - \cos^2 y). \tag{22}$$

Thus, the constant value c becomes

$$c = \frac{n_0}{\int\int g\mathcal{D}dxdy}.$$ (23)

Velocity space part of distribution function $g(x,y)$ will be determined by solving the following equation numerically.

$$L(x,y)g(x,y) = -\kappa^2 h(x,y)g(x,y).$$ (24)

The contours of the distribution function is presented in Fig. 1 and Fig. 2 by varying the potential at the mirror points .
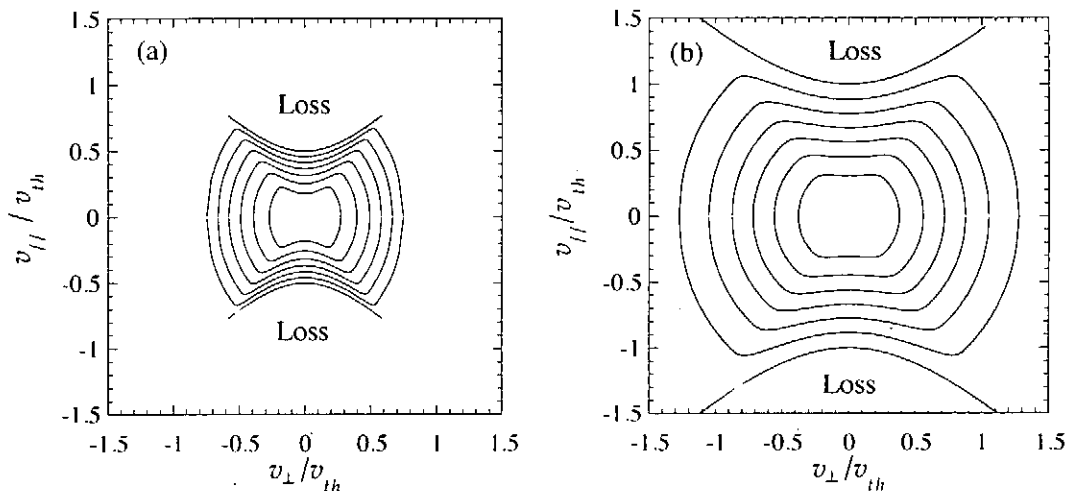

Fig. 1: Contours of the electron distribution in the edge region (a) for $|q\phi| = 0.25T$, and (b) for $|q\phi| = T$.
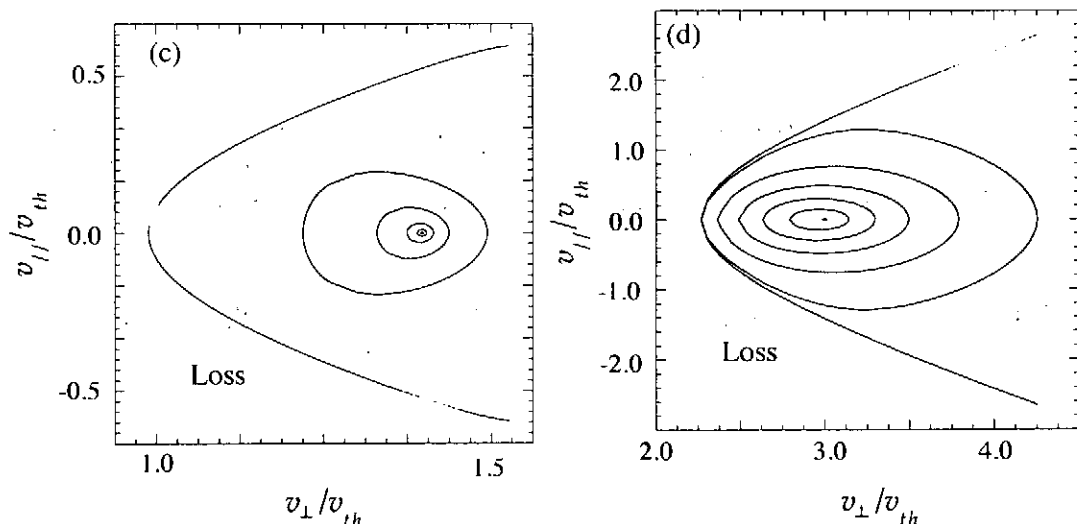

Fig. 2: Contours of the ion distribution in the edge region (c) for $|q\phi| = T$, and (d) for $|q\phi| = 5T$.

From these figures, it appears the gradient of the distribution function toward the loss region increase as the potential decrease. This is because electron mirror loss enhances in this case. Increasing the potential, on the other hand, the gradient for ions increase.

The potential which we give above, however, does not satisfy the ambipolarity. From the charge neutrarity condition, we obtain the following relation.

$$\sqrt{\frac{2(R-1)e^2\kappa_e^2}{r^2m^2R\alpha^2}} = \sqrt{\frac{2(R-1)q^2\kappa_i^2}{r^2M^2R\beta^2}}. \tag{25}$$

Therefore,

$$\frac{\kappa_e^2}{m} = \frac{\kappa_i^2}{M}. \tag{26}$$

The loss flux is defined by the equation:

$$
\begin{aligned}
(\text{Loss flux}) &\equiv \int\int A(x,y)L(x,y)f(x,y,\psi)\mathcal{D}dxdy \\
&= -\int\int c\kappa^2 A(x,y)\Psi(\psi)g(x,y)h(x,y)\mathcal{D}dxdy,
\end{aligned} \tag{27}
$$

where,

$$A^i(x,y) = \frac{nq^4\lambda}{8\pi\varepsilon_0^2}\frac{(R-1)^{3/2}}{M^2R^{3/2}|\beta|^3}\frac{1}{(\cosh^2 x - \sin^2 y)^{3/2}},$$

$$A^e(x,y) = \frac{nq^4\lambda}{8\pi\varepsilon_0^2}\frac{(R-1)^{3/2}}{m^2R^{3/2}|\alpha|^3}\frac{1}{(\cosh^2 x - \sin^2 y)^{3/2}}.$$

By equating the electron loss flux to the ion's to obtain the ambipolar potential, one can find the relation as

$$
\begin{aligned}
\int_0^\infty \int_0^{\sin^{-1}\sqrt{\frac{R-1}{R}}} &c_i\kappa_i^2 A^i(x,y)\Psi^i(\psi)g^i(x,y)h^i(x,y)\mathcal{D}^i dxdy \\
&= \int_0^\infty \int_{\cos^{-1}\sqrt{\frac{R-1}{R}}}^{\frac{\pi}{2}} c_e\kappa_e^2 A^e(x,y)\Psi^e(\psi)g^e(x,y)h^e(x,y)\mathcal{D}^e dxdy.
\end{aligned} \tag{28}
$$

Using Eq. (30), we will find the ambipolar potential ϕ_{mir} corresponding uniquely to the eigenvalue κ. Unfortunately, we have not found the relation between κ and the potential ϕ_{mir} so far. Our future study is to obtain this relation and associated density profile.

*) T. Takahashi, Y. Tomita, H. Momota, and N. V. Shabrov, Phys. Plasmas **4**, 4301 (1997)

High beta plasma as active self-control factor of the compact closed system confinement and disruption

R. Kh. Kurtmullaev
Russian State Research Center TRINITI
Troitsk, 142092, Moscow region, Russia

The Programming Compact Torus approach opens some phenomenal features of the high energized plasma having a dominant role by creation the specific self-organized state, that leads to:

- Strong directed scenario of the system total energy conversion with anomal fast contribution in plasma heating.
- Comprehensive reconstruction of global structure with shock transformation to equilibrium state.
- Forced depressing of any strong disruptive activities, etc.

These principles have universal and reproductive character in wide parameters area relating to operation conditions of the TOR, BN, TL devices ($n \sim (1-5) \times 10^{15}$ cm^{-3}, $B \sim 5$-20 kGs).

A physical affect of the high energized plasma on the system extreme regions (magnetic fields high curvature and sign reversal) represents a special importance.

Other program of the high energized plasma activity, leading to a closed system strong disturbance and disruption, have also some definable special conditions.

Study of 1 1/4D Time Dependent Model of FRC[1]

S. Hamada and Y. Takaku

College of Science and Technology Nihon university

14th December 1998

Abstract

The model is studied systematically. An integral theorem and relations among several decay rates of relevant quantities are obtained. The quasi-steady solution of this model is also studied to make clear under which circumstance it is maintained to be a stationary solution of the time dependent model equation. A formal criterion for a quasi-steady solution to be an attractor is deduced.

1 Introduction

The 1 1/4 D time dependent model of Field Reversed Configuration (FRC) was proposed by Steinhauer, Milroy and Slough in 1985 for the first time and numerically solved to examine validity of their 1 1/4 D quasisteady model[1]. Although there are more realistic models of FRC[2][3] other than this one, it may be worth studying systematically because it is the simplest model with perfect inner consistency. Our study has not yet finished but our schedule is as follows. First, we formulate again this model so as to fit our purpose. Second, quasi stationary solutions are shown to be maintained under a certain circumstance. Third, it is studied under which circumstance it could be an attractor. Finally, it will be studied what would happen if the foregoing circumstances are violated. Here, we report results up to the second problem and, as for the third problem, only a formal criterion for the quasisteady solution to be an attractor. Assumptions for the model are as follows.

1. **long racetrack shape of separatrix** Length $L(t)$ of the uniform part of separatrix is sufficiently longer than the radius $r_s(t)$

$$\frac{L}{r_s} \gg 1 \tag{1.1}$$

   L and r_s are treated as slowly dependent on time t and length of all the magnetic surfaces are taken to be equal to $L(t)$.

2. **axial symmetry** We set cylindrical coordinates (r, θ, z) with z axis aligned on the axis of symmetry and $z = 0$ on the equatorial plane of the separatrix. As we concentrate mainly on structure of the uniform part of separatrix, almost all field quantities are taken to be independent of z, that is, the z component of magnetic field B_z, the θ component of electric field E_θ, the r component of plasma velocity v_r, the plasma pressure p, the plasma density ρ and the electric resistivity η are taken to be functions of r, t only. One exception is the z component of plasma velocity

---

[1] This paper has been submitted also to the editor of proceedings of 1998-workshop on MHD Computation held 25 ~ 27th Nov. 1998 at NIFS.

v_z, which is taken to be a function of r, z, t. Another exception is a parameter Θ of plasma temperatures, which is taken to be spacially uniform. (See next item.)

3. **Uniformity of temperatures** We assume that the ratio of the plasma pressure to the density is spacially uniform and dependent only on time t.

$$\frac{p}{\rho} = \frac{kT_i}{m_i} + \frac{ZkT_e}{m_i} = \Theta(t) \tag{1.2}$$

where m_i and m_e are the ion and electron mass, T_i and T_e the ion and electron temperatures, Z the charge number of ion and k the Boltzmann's constant.

4. **uniformity of main coil** The main coil has a uniform inner radius r_w and sufficiently longer than the separatrix length $L(t)$. As a result, we have the well known axial force balance relation[6]

$$\langle \beta \rangle = 1 - \frac{r_n^2}{r_w^2} \tag{1.3}$$

where $\langle \beta \rangle$ is the β ratio averaged inside the separatrix and r_n is the radius of the neutral surface. (Notice the well known relation that $2r_n^2 = r_s^2$.)

5. **functional form of v_z** We assume that

$$v_z(r, z, t) = \frac{2z}{L} v_z(r, \frac{L}{2}, t) \quad (1.4) \qquad v_z(r, \frac{L}{2}, t) = \frac{1}{2}\frac{dL}{dt} + \nu(r, t) \tag{1.5}$$

where ν is the z component of relative velocity of plasma to the separatrix end. The function ν is determined later. See eq. (3.2).

6. **basic laws used for the model** In addition to the foregoing assumptions. the model is based upon the following laws.

pre-Maxwell equations:

$$\frac{\partial \vec{B}}{\partial t} = -\nabla \times \vec{E} \quad (1.6) \qquad \nabla \cdot \vec{B} = 0 \quad (1.7) \qquad \mu\vec{j} = \nabla \times \vec{B} \tag{1.8}$$

generalized Ohm's law

$$\eta\vec{j} = \vec{E} + \vec{v} \times \vec{B} \tag{1.9}$$

equilibrium equation

$$\nabla p = \vec{j} \times \vec{B} \tag{1.10}$$

mass continuity equation for particle transport

$$\frac{\partial \rho}{\partial t} + \nabla \cdot (\rho\vec{v}) = 0 \tag{1.11}$$

where μ is the permiability of vacuum, $\vec{j}$ the electric current density and η the electric resistivity of the plasma.

2   Dimensionless Flux ψ, Coordinate u and Time Variable τ

We define a dimensionless flux ψ as

$$\psi(r,t) = \frac{1}{\pi r_s^2 B_e} \int_0^r 2\pi r B_z(r,t) dr \qquad (2.1)$$

so that ψ is related to the magnetic flux Φ as

$$\Phi(r,t) = \pi r_s^2(t) B_e(t) \psi(r,t) \qquad (2.2)$$

Here, $B_e(t)$ is the value of B_z at the inner wall $r = r_w$ of the main coil. It will be called "external field" hereafter. From this definition of ψ, we have

$$B_z = \frac{B_e r_s^2}{2r} \frac{\partial \psi}{\partial r} = 2B_e \frac{\partial \psi}{\partial u} \qquad (2.3) \quad where \quad u = \frac{2r^2}{r_s^2(t)} - 1 \qquad (2.4)$$

The coordinate u was introduced by Tuszewski and Linford[4]. As it is well known, this coordinate has many advantages. The axis of the system, the neutral surface and the separatrix always correspond to the values $-1, 0, 1$ of u, respectively. Inside the separatrix, every magnetic surface $\psi = const.$ has two radii $r_+(\psi) > r_-(\psi) > 0$ and, correspondingly, two coordinates $u_+(\psi) > u_-(\psi)$. The remarkable relation $u_- = -u_+$ always holds. Therefore, we have $\psi(u) = \psi(-u)$ so that $\psi(u)$ is an even function of u in the domain $[-1,1]$ of u. p and ρ are also even functions of u but B_z is an odd function of u on account of (2.3). Furthermore, the function ν in eq. (1.5) is easily seen to be an odd function of u. Since the neutral surface corresponds to $u = 0$ because $u_+ = u_-$, we always have $r_n^2 = r_s^2/2$ on account of (2.4). These facts suggest that we had better to use the coordinate u rather than r.

In order to make resulting equation dimensionless, we introduce a dimensionless time variable τ and, correspondingly, decay rate $1/\tau_f$ of an arbitrary quantity f, which are defined as

$$\tau(t) = \int_0^t \frac{\eta(0,t)}{\mu r_n^2(t)} dt \qquad (2.5) \qquad \frac{1}{\tau_f} = -\frac{1}{f}\frac{df}{d\tau} = -\frac{\mu r_n^2}{\eta(0,t)f}\frac{df}{dt} \qquad (2.6)$$

where $\eta(0,t)$ is the electric resistivity on the neutral surface.

Now, almost all relevant quantities except ν in (1.5) can be expressed in terms of $\psi(u,\tau)$ in the following way.

$$p = \frac{B_e^2}{2\mu}(1 - 4\psi'^2) \quad (2.7) \quad \rho = \frac{B_e^2}{2\mu\Theta}(1 - 4\psi'^2) \quad (2.8) \quad \mu j_\theta = -4B_e \frac{\sqrt{u+1}}{r_n}\psi'' \quad (2.9)$$

$$E_\theta = -\frac{\eta(0,\tau)}{\mu r_n(\tau)}\frac{B_e}{\sqrt{u+1}}\{\frac{\partial \psi}{\partial \tau} - (\frac{1}{\tau_{B_e}} + \frac{1}{\tau_{r_s^2}})\psi + \frac{u+1}{\tau_{r_s^2}}\psi'\} \qquad (2.10)$$

$$rv_r = \frac{\eta(0,\tau)}{\mu}\frac{1}{2\psi'}\{-\frac{\partial \psi}{\partial \tau} + (\frac{1}{\tau_{B_e}} + \frac{1}{\tau_{r_s^2}})\psi - \frac{u+1}{\tau_{r_s^2}}\psi' + \frac{4\eta(u,\tau)}{\eta(0,\tau)}(u+1)\psi''\} \qquad (2.11)$$

where $'$ means the partial derivative with respect to u.

3 Equation of Mass Continuity

The equation of mass continuity (1.11) is expressed in the cyrindrical coordinates as

$$(\frac{\partial \rho}{\partial t})_r + \frac{1}{r}\frac{\partial \rho r v_r}{\partial r} + \rho \frac{\partial v_z}{\partial z} = 0$$

Changing independent variables (r, t) to (u, τ), using (1.4, 5) for v_z, (2.8) for ρ and (2.11) for rv_r, we obtain an equation for $\psi(u, \tau)$. In the domain $[-1, 1]$ of u, the even and odd parts of this equation should hold separately. Thus, we obtain from the even part.

$$(\frac{1}{\psi'}\frac{\partial \psi}{\partial \tau})' = \frac{1}{1 + 4\psi'^2}[\{\frac{1 - 4\psi'^2}{\psi'}(\frac{\psi}{\tau_{B_e}r_s^2} + 4g(u, \tau)\psi'')\}'$$

$$-(\frac{1}{\tau_{B_e^2/\Theta}} + \frac{1}{\tau_{r_s^2}} + \frac{1}{\tau_L})(1 - 4\psi'^2)] \tag{3.1}$$

where g is a function defined as $g(u, \tau) = (\bar{\eta} + \tilde{\eta}u)/\eta(0, \tau)$ with the even part $\bar{\eta}$ and the odd part $\tilde{\eta}$ of $\eta(u, \tau)$. The equation (3.1) is used to determine $\psi(u, \tau)$. On the other hand, from the odd part of the mass continuity equation we obtain

$$\nu = \frac{\eta(0, \tau)}{\mu r_n^2}\frac{L}{2(1 - 4\psi'^2)}\left[\frac{8\psi'\psi''}{\tau_{r_s^2}} + [\frac{1 - 4\psi'^2}{\psi'}\{\frac{\psi'}{\tau_{r_s^2}} - \frac{4(\bar{\eta}u + \tilde{\eta})}{\eta(0, \tau)}\psi''\}]'\right] \tag{3.2}$$

This equation is used to determine $\nu(u, \tau)$ after the equation (3.1) is solved.

4 Flux Loss Time τ_Φ and Particle Loss Time τ_N

From (2.2), we have a relation

$$\frac{1}{\tau_\Phi} = \frac{1}{\tau_{B_e}} + \frac{1}{\tau_{r_s^2}} + \frac{1}{\tau_\psi} \quad where \quad \frac{1}{\tau_\Phi} = -\frac{\partial \Phi(0, \tau)}{\Phi(0, \tau)\partial \tau}, \quad \frac{1}{\tau_\psi} = -\frac{\partial \psi(0, \tau)}{\psi(0, \tau)\partial \tau} \tag{4.1}$$

From physical point of view, rv_r should be continuous everywhere. This means that the even and odd parts of the right hand side of (2.11) should be continuous, separately. In particular, the odd part should vanish and continuous at $u = 0$. Then, we obtain the following two equations

$$\frac{1}{\tau_\Phi} = -\frac{4\psi''(0, \tau)}{\psi(0, \tau)} \tag{4.2} \qquad \lim_{u \to 0}\frac{1}{\psi'}(\frac{\psi}{\tau_\Phi} + 4g\psi'') = 0 \tag{4.3}$$

For the total ion number N inside the separatrix, we have $N = (L/m_i\Theta)\pi r_s^2(B_e^2/2\mu)\langle\beta\rangle$. Then, we have a relation

$$\frac{1}{\tau_N} = \frac{1}{\tau_L} - \frac{1}{\tau_\Theta} + \frac{1}{\tau_{r_s^2}} + \frac{1}{\tau_{B_e^2}} + \frac{1}{\tau_{\langle\beta\rangle}} \tag{4.4} \quad where \quad \frac{1}{\tau_{r_s^2}} = -\frac{\langle\beta\rangle}{1 - \langle\beta\rangle}\frac{1}{\tau_{\langle\beta\rangle}} \tag{4.5}$$

where (4.5) is obtained from (1.3). The particle loss rate can also be obtained by calculating ion number per unit time passing through the separatrix.

$$\frac{1}{\tau_N} = \frac{2\pi r_s L\rho_s}{m_i N}\{\frac{\mu r_n^2 v_{rs}}{\eta(0, \tau)} - \frac{dr_s}{d\tau}\} = \frac{\beta_s}{\langle\beta\rangle}\{\frac{\mu r_s v_{rs}}{\eta(0, \tau)} + \frac{1}{\tau_{r_s^2}}\} = \frac{4g_s(1 - 4\psi_s'^2)\psi_s''}{\langle1 - 4\psi'^2\rangle\psi_s'} \tag{4.6}$$

Here, the suffix s means the value on the separatrix $u = 1$ and the final expression is obtained with use of (2.11). This expression for particle loss rate is the same as those obtained for quasisteady models[4][5].

5   Basic Equation for the Model

Since $\psi'(0,\tau) = 0$ on the neutral surface (see eq. (2.3)), the equation (3.1) has singularity on both sides at $u = 0$. Noticing an identity

$$(\frac{\psi}{\psi'})' = \frac{1}{1 + 4\psi'^2}\{(\frac{1 - 4\psi'^2}{\psi'}\psi)' + 8\psi'^2)\} \tag{5.1}$$

multiplying $1/\tau_\psi$ on both the sides, adding them to both sides of (3.1) and using (4.1) and (4.4) we get

$$\frac{\partial \psi(u,\tau)}{\partial \tau} = \psi'(u,\tau)\int_0^u \frac{du}{1 + 4\psi'^2}\left[\{\frac{1 - 4\psi'^2}{\psi'}(\frac{\psi}{\tau_\Phi} + 4g(u,\tau)\psi'')\}'\right.$$

$$\left. -(\frac{1}{\tau_N} - \frac{1}{\tau_{\langle\beta\rangle}})(1 - 4\psi'^2) + \frac{8\psi'^2}{\tau_\psi}\right] - \frac{\psi(u,\tau)}{\tau_\psi} \tag{5.2}$$

where the singurarities have been removed as seen from (4.3). This is our basic equation. In order to determine the time variation of ψ at a time τ, it needs to know, together with $\psi(u,\tau)$, several decay rates $1/\tau_\Phi, 1/\tau_N, 1/\tau_\psi$ and $1/\tau_{r_s^2}$ or $1/\tau_{\langle\beta\rangle}$ at the same time τ. The former three decay rates, however, can be determined by (4.2), (4.6) and (4.1) if $\psi(u,\tau)$ and $1/\tau_{r_s^2}$ are given. Differentiating both sides of (5.2) with respect to u, and trying directly to calculate $1/\tau_{\langle\beta\rangle}$, we obtain an integral theorem instead of $1/\tau_{\langle\beta\rangle}$ itself. That is

$$\int_0^1 \frac{du}{1 + 4\psi'^2}\left[\{\frac{1 - 4\psi'^2}{\psi'}(\frac{\psi}{\tau_\Phi} + 4g(u,\tau)\psi'')\}' - (\frac{1}{\tau_N} - \frac{1}{\tau_{\langle\beta\rangle}})(1 - 4\psi'^2) + \frac{8\psi'^2}{\tau_\psi}\right] = 0 \tag{5.3}$$

This theorem is clearly necessary for the basic equation to be compatible with the requirement

$$\psi(1,\tau) = 0 \quad and \quad \frac{\partial \psi(1,\tau)}{\partial \tau} = 0 \tag{5.4}$$

The decay rate $1/\tau_{r_s^2}$ or $1/\tau_{\langle\beta\rangle}$ is determined so that this theorem holds. That is

$$\frac{1}{\tau_{r_s^2}} = \frac{\langle\frac{2g\beta\beta'^2}{(2-\beta)^2(1-\beta)}\rangle + \frac{1}{\tau_N}(1 + \frac{\langle\beta\rangle}{2-\beta_s} - \langle\frac{1}{1-\beta/2}\rangle) - \frac{1}{\tau_{B_e}}(2 - \langle\frac{1}{1-\beta/2}\rangle)}{1 + (2 - \frac{1}{\langle\beta\rangle})(1 - \langle\frac{1}{1-\beta/2}\rangle)} \tag{5.5}$$

Notice that the decay rate of the external field $1/\tau_{B_e}$ is a known variable. The angle bracket means integration from $u = 0$ to 1: average of an even function inside the separatrix. By the way, we obtain from (5.5) and (4.4)

$$\frac{1}{\tau_L} - \frac{1}{\tau_\Theta} = -\frac{2 - \frac{1}{\langle\beta\rangle}}{1 + (2 - \frac{1}{\langle\beta\rangle})(1 - \langle\frac{1}{1-\beta/2}\rangle)}\{\langle\frac{2g\beta\beta'^2}{(2-\beta)^2(1-\beta)}\rangle$$

$$+(\frac{\langle\beta\rangle}{2 - \beta_s} - \frac{1}{2 - \frac{1}{\langle\beta\rangle}})\frac{1}{\tau_N} + (\frac{2}{2 - \frac{1}{\langle\beta\rangle}} - \langle\frac{1}{1-\beta/2}\rangle)\frac{1}{\tau_{B_e}}\} \tag{5.6}$$

6   Quasisteady State

We call ψ satisfying (5.2) but independent of time τ "quasisteady solution" and denote it as $\psi_0(u)$ with suffix 0. All quantities relevant to ψ_0 will also be shown by the same suffix 0. In order for the equation (5.2) to have a quasisteady solution, $g, \tau_\Phi, \tau_N, \tau_\psi$ and $\tau_{r_s^2}$ or $\tau_{\langle\beta\rangle}$ have to be independent of time τ. Furthermore, we have $1/\tau_\psi = 0, 1/\tau_{\langle\beta\rangle} = 1/\tau_{r_s^2} = 0$ for the quasisteady state. Thus, the basic equation (5.2) becomes the following ordinary differential equation for the quasisteady state

$$\{\frac{1 - 4\psi_0'^2}{\psi_0'}(\frac{\psi_0}{\tau_{\Phi 0}} + 4g\psi_0'')\}' - \frac{1}{\tau_{N0}}(1 - 4\psi_0'^2) = 0 \tag{6.1}$$

Boundary conditions for this equation are as follows.

$$\psi_0'(0) = 0 \qquad (6.2) \qquad \lim_{u \to 0} \frac{1}{\psi_0'}(\frac{\psi_0}{\tau_{\Phi 0}} + 4\psi_0'') = 0 \tag{6.3}$$

$$\psi_0(1) = 0 \qquad (6.4) \qquad \psi'(1) = \frac{1}{2}\sqrt{1 - \beta_{0s}} \tag{6.5}$$

The problem (6.1 $\sim$ 5) was investigated by one of the authors[5] in case of $g = 1$. That is, for a pair of parametors $0 < \alpha < \infty$, $0 < \beta_{0s} < 1$, there is a unique solution $\psi_0, \tau_{\Phi 0}, \tau_{N0}$ with a single neutral surface and negative flux inside the separatrix. The flux loss time $\tau_{\Phi 0}$ is a function of α and β_s, and the particle loss time τ_{N0} is given by $\tau_{N0} = \tau_{\Phi 0}/\alpha$. This results do not change for non-uniform g. Thus, there may be a two dimensional domain D such that, if $(\tau_{\Phi 0}, \tau_{N0}) \in D$, there is at least a solution which satisfies (6.1 $\sim$ 4) except (6.5).

Now, let us consider conditions under which, if the initial value of ψ is equal to $\psi_0(u)$, the quasisteady state $\psi_0(u)$ is maintained as a stationary solution of the equation (5.2). First, g should be independent of time. Second, $\tau_N = \tau_{N0}$ should be maintained by somehow controlling the edge layer. Third. $1/\tau_{\langle\beta\rangle} = 1/\tau_{r_s^2} = 0$ should be maintained by controlling the external field B_e so that (see (5.5))

$$\frac{1}{\tau_{B_e 0}} = \frac{1}{2 - \langle\frac{1}{1-\beta_0/2}\rangle}\{\langle\frac{2g\beta_0\beta_0'^2}{(2 - \beta_0)^2(1 - \beta_0)}\rangle + \frac{1}{\tau_{N0}}(1 + \frac{\langle\beta_0\rangle}{2 - \beta_{0s}} - \langle\frac{1}{1 - \beta_0/2}\rangle)\} \tag{6.6}$$

Under these three conditions, $\psi_0(u)$ continues to be a solution of (5.2). In fact, if at a time τ the three conditions are satisfied and $\psi(u, \tau) = \psi_0(u)$, then, the basic equation (5.2) and the integral theorem (5.3) become

$$\frac{\partial \psi}{\partial \tau} = \psi_0' \int_0^u \frac{8\psi_0'^2/\tau_\psi}{1 + 4\psi_0'^2}du - \frac{\psi_0}{\tau_\psi} \qquad and \qquad \int_0^1 \frac{du}{1 + 4\psi_0'^2}\frac{8\psi_0'^2}{\tau_\psi} = 0$$

respectively. We, therefore, have $1/\tau_\psi = 0$ from the integral theorem and the right hand side of the basic equation vanishes. Thus, $\psi_0(u)$ continues to be a solution of the time dependent equation.

7   Small Deviation $\delta\psi$ from a Quasisteady State

We put $\psi(u,\tau) = \psi_0(u) + \delta\psi(u,\tau)$ and consider behavior of $\delta\psi$ within a range of linear theory. We assume that g is not only independent of τ but also uniform: $g = 1$, for simplicity. Since the particle loss rate is always given by (4.6), we assume that the deviation of particle loss rate $\delta(1/\tau_N)$ due to the perturbation $\delta\psi$ is given by

$$\frac{1 - 4\psi_{0s}'^2}{\psi_{0s}'} \delta\psi_s'' - (\frac{1}{\psi_{0s}'^2} + 4)\psi_{0s}'' \delta\psi_s' = \frac{\delta\langle\beta\rangle}{4\tau_{N0}} + \frac{\langle\beta_0\rangle}{4}\delta(\frac{1}{\tau_N}) \tag{7.1}$$

An assumption included here is that the value of τ_{N0} on the right hand side is fixed by somehow controlling the edge layer. We fix the decay rate of the external field at the value of $1/\tau_{B_e0}$ given by (6.6). Then, if $\delta\psi = 0$, we have $1/\tau_{\langle\beta\rangle} = 0$. But if $\delta\psi \neq 0$, as it can be seen from (5.5) and (4.5) we have a deviation given by

$$\delta(\frac{1}{\tau_{\langle\beta\rangle}}) = \frac{1 - \frac{1}{\langle\beta_0\rangle}}{1 + (2 - \frac{1}{\langle\beta_0\rangle})(1 - \langle\frac{1}{1-\beta_0/2}\rangle)}[\delta\langle\frac{2\beta\beta'^2}{(2-\beta)^2(1-\beta)}\rangle$$

$$+ \frac{1}{\tau_{N0}}(\delta\frac{\langle\beta\rangle}{2 - \beta_s} - \delta\langle\frac{1}{1-\beta/2}\rangle) + \frac{1}{\tau_{B_e0}}\delta\langle\frac{1}{1-\beta/2}\rangle$$

$$+ \delta(\frac{1}{\tau_N})(1 + \frac{\langle\beta_0\rangle}{2 - \beta_{0s}} - \langle\frac{1}{1-\beta_0/2}\rangle)] \tag{7.2}$$

The deviations $\delta(1/\tau_\Phi)$ and $\delta(1/\tau_\psi)$ due to $\delta\psi$ can also be calculated from (4.2) and (4.1). Now, linearizing the basic equation (5.2), we get

$$\frac{\partial}{\partial\tau}(\frac{\delta\psi}{\psi_0'})' = \frac{1}{1 + 4\psi_0'^2}\left[\{-\frac{1 + 4\psi_0'^2}{\psi_0'^2}(\frac{\psi_0}{\tau_{\Phi0}} + 4\psi_0'')\delta\psi' + \frac{1 - 4\psi_0'^2}{\psi_0'}(\frac{\delta\psi}{\tau_{\Phi0}} + 4\delta\psi'')\}'\right.$$

$$+ \frac{8\psi_0'}{\tau_{N0}}\delta\psi' + \delta(\frac{1}{\tau_{\langle\beta\rangle}})\{(1 - 4\psi_0'^2) - \frac{\langle\beta_0\rangle}{1 - \langle\beta_0\rangle}(\frac{1 - 4\psi_0'^2}{\psi_0'}\psi_0)'\}$$

$$\left. - \delta(\frac{1}{\tau_N})(1 - 4\psi_0'^2)\right] \tag{7.3}$$

Notice that $\delta(1/\tau_\Phi)$ and $\delta(1/\tau_\psi)$ disappear by cancelling each other. Denoting [ ] on the right hand side as $L(\delta\psi)$, the equation is written in a short form:

$$\frac{\partial}{\partial\tau}(\frac{\delta\psi}{\psi_0'})' = \frac{L(\delta\psi)}{1 + 4\psi_0'^2} \tag{7.3'}$$

8   a Criterion for ψ_0 to be an Attractor

Multiplying $(1 + 4\psi_0'^2)\psi_0'^4(\delta\psi/\psi_0')'$ on both sides of (7.3') and integrating from $u = 0$ to 1, we get

$$\frac{1}{2}\frac{\partial}{\partial\tau}\langle(1 + 4\psi_0'^2)\psi_0'^4(\frac{\delta\psi}{\psi_0'})'^2\rangle = \langle(\frac{\delta\psi}{\psi_0'})'\psi_0'^4 L(\delta\psi)\rangle \tag{8.1}$$

If the right hand side of this equation is always negative for any permissible $\delta\psi$, the quasisteady state ψ_0 is an attractor. In fact, if the condition holds, we have

$$\langle(1+4\psi_0'^2)\psi_0'^4(\frac{\delta\psi}{\psi_0'})'^2\rangle \to 0$$

Then, we have at each point of u

$$\delta\psi'\psi_0' - \delta\psi\psi_0'' \to 0$$

On the other hand, the differential equation of $\delta\psi$

$$\delta\psi'\psi_0' - \delta\psi\psi_0'' = 0$$

has the general solution $\delta\psi = const.\psi_0'$ and only one solution satisfying the boundary condition $\delta\psi(u=1) = 0$ is $\delta\psi = 0$. Therefore, if the right hand side of (8.1) is always negative, $\delta\psi$ indefinitely tends to zero and the quasisteady state is an attractor. The right hand side of (8.1) can be rewritten by integration by parts as

$$\langle(\frac{\delta\psi}{\psi_0'})'\psi_0'^4 L(\delta\psi)\rangle = -\langle\frac{\delta\psi}{\psi_0'}\{\psi_0'^4 L(\delta\psi)\}'\rangle$$

So, if we define a linear operator $\mathcal{L}$ as

$$\mathcal{L}(\delta\psi) = \frac{1}{\psi_0'}\{\psi_0'^4 L(\delta\psi)\}' \tag{8.2}$$

the criterion for ψ_0 to be an attractor is that the inequality

$$\langle\delta\psi\mathcal{L}(\delta\psi)\rangle > 0 \tag{8.3}$$

is always satisfied.

9   Conclusion

The 1 1/4D time dependent model of field reversed configuration has been formulated in somewhat different way from the original work[1], and in its process, an integral theorem has been obtained together with relations among decay rates of several relevant quantities. Conditions that the quasisteady state is maintained as a stationary solution of the time dependent equation have been listed up. A formal criterion has been proposed for a quasisteady state to be an attractor.

references

[1] L.C. Steinhauer, R.D. Milroy and J.T. Slough, Phys. Fluids 28 p888 1985
[2] L.C. Steinhauer, Phys. Fluids B2(11) p2679 1990
[3] D.E. Schumaker, J.K. Boyd, S.P. Auerbach and B. McNamara, J. of Computational Phys. 45 p266 1982
[4] M. Tuszewski and R.K.Linford Phys. Fluids 25 p765 1982
[5] S. Hamada, Nuclear Fusion, 26 p729 1986
[6] W.T. Armstrong, R.K. Linford, J. Lipson, D.A. Platts and E.G.Shertwood, Phys.Fluids 24 p2068 1981

Global Stability of FRC Plasmas in the Proposed SPIRIT Device

H. Ji, M. Yamada, R. Kulsrud, C.Z. Cheng, and N. Pomphrey

PPPL, Princeton University, New Jersey, USA

Global stability of field-reversed configuration (FRC) plasmas has been conceptually studied [1] using a simple rigid body model in the parameter space of s (ratio of separatrix radius to average ion gyro-radius), plasma elongation E (ratio of separatrix length to separatrix diameter), and plasma rotation. Tilt stability is predicted, independent of s, for FRC's with low E (oblate), while the tilt stability of FRC's with large E (prolate) depends on s/E. It is found that plasma rotation due to ion diamagnetic drift and ion gyro-viscosity can stabilize the tilt mode when s/E < 2.8. Effects of an additional rotation, which is self-consistently incorporated in the equilibrium, are also being studied. Similar approaches are taken to study the physics of shift and interchange stability of FRC plasmas. Global stability of FRC plasmas in the proposed SPIRIT device [2] will be discussed in light of these conceptual studies.

[1] H. Ji, M. Yamada et al. Phys. Plasmas 5, 3685(1998).
[2] M. Yamada, H. Ji et al. this conference.

Magnetic compression of an FRC plasma

S. Okada, K. Kitano, H. Matsumoto, K. Yamanaka, T. Ohtsuka,
A. K. Martin, M. Okubo, S. Yoshimura, S. Sugimoto, S. Ohi, S. Goto.
Plasma Physics Laboratory Faculty of Engineering,
Osaka University, Osaka, Japan.

Abstract

Confinement of a plasma with field-reversed configuration (FRC) is predicted to be improved if it is compressed only axially, keeping the magnetic flux between the separatrix and the confining chamber (flux conserver) wall unchanged, while allowing the plasma to expand radially. The prediction is based on an empirical scaling law of FRC confinement and on the assumption that the compression is done adiabatically. The apparatus for this axial compression was developed and the axial compression experiment was actually carried out by decreasing the distance of the mirror fields between which the FRC plasma is confined by 30% and the plasma life time of about 500μs was increased by about 50μs.

1. Introduction

A field-reversed configuration (FRC) plasma has only poloidal field and an elongated shape[1]; the ratio of its length to diameter is about 10. From this fact, the separatrix radius r_s and magnetic axis radius at axial midplane R of the FRC are related by $r_s = \sqrt{R}$. Outside the separatrix, plasma pressure drops to zero with a scale length of a few ion gyro radii[2]. From these facts, the beta value in the axial mid-plane, averaged inside the separatrix of an FRC in a solenoid or a cylindrical flux conserver is given by $<\beta> = 1 - (r_s/r_w)^2/2$, where r_w is the conductive wall radius. The separatrix radius $r_s(z)$ at an arbitrary axial position is obtained with good precision from an axial array of diamagnetic probes except for the region near either end of the FRC.

The FRC plasma is produced in our case by a negatively-biased theta-pinch machine, which consists of quartz discharge tube and massive, high voltage pinch coils; therefore access to the plasma for additional heating is extremely poor. As no material structures link the FRC, it can be translated axially from the theta pinch to a confinement chamber. By translating the FRC, additional heating experiments could be performed. On the FRX-C/LSM facility in Los Alamos, high power (1GW) magnetic compression heating was successfully done[3]. On the FRC Injection Experiment (FIX) machine in Osaka, a fast rising (rise time was about an ion gyro period) magnetic pulse from a one turn coil placed coaxially to the machine axis was applied to the translated FRC plasma and heating was observed[4]. In the former experiment, the plasma heating from $T(= T_e + T_i)$ of 0.6keV to 2.2keV was accomplished by increasing the confining magnetic field from 0.4T to 1.5T in 55μs. The result was consistent with the adiabatic compression theory. Though the heating was excellent, the confinement properties became poor. The energy confinement time τ_E shortened by a factor of 2~3 to 35μs. In the latter case, the strength of the magnetic pulse at its maximum was about equal to the strength of the confining field of 0.04T and the rise in the plasma temperature was only about 10% of its initial value. But most importantly, the confinement properties were improved by this heating. The result was explained based on the empirical scaling law $\tau_N \propto R^2/\rho_i$, where, τ_N and ρ_i are particle confinement time and the ion gyro radius in the external field, respectively. The explanation for this is that an unfavorable tendency for the confinement due to the increase of ρ_i was more than cancelled by the favorable effect brought about by the increase of R by the heating.

We propose in this work an axial compression of an FRC plasma as a method to heat as well as improve confinement.

2. Theoretical model

The FRC is compressed axially in a flux conserver without changing the external flux or the magnetic flux between the separatrix and the chamber wall. The plasma is heated by the compression and r_s increases until the magnetic pressure of the external field balances the plasma pressure. The change of the plasma parameters from before to after the axial compression is estimated with a simple model: We assume that the compression is done adiabatically in a time scale faster than the transport time scale. The plasma is assumed to be cylindrical in shape with the radius r_s and the length l_s. Therefore, the total particle number N is written by

$$N = n_{max}\langle\beta\rangle V$$

where, n_{max} is the density at the magnetic axis and

$$V = \pi r_w^2 x_s^2 l_s$$

where, x_s is r_s/r_w and l_s is the plasma length. Plasma temperature is assumed to be uniform. As the adiabatic relation, we use

$$n_{max}^{1-\gamma} T = const.$$

Conservation of the external flux reads as follows.

$$B_w = B_{vac}/(1 - x_s^2)$$

where, B_w and B_{vac} are the magnetic fields just inside the flux conserver wall with and without the plasma, respectively. The plasma length before and after compression is written by l_i and l_f. The change of x_s from x_i to x_f is obtained from the above equations to be

$$(1 - x_f^2)/(1 - x_i^2) = (\langle\beta\rangle_f x_f^2 l_f / \langle\beta\rangle_i x_i^2 l_i)^{\gamma/2}$$

We can obtain an approximate solution to this equation if we set $\langle\beta\rangle_i = \langle\beta\rangle_f = 1$. As $\langle\beta\rangle_i$ is about 0.9 and $\langle\beta\rangle_f$ is closer to 1, serious error will not result from this approximation. The term in the parenthesis of the above equation is written as n_f/n_i. If we define a compression ratio c as $c = B_f/B_i$, c can then be written as

$$c = (1 - x_f^2)/(1 - x_i^2)$$

In terms of c, the final temperature and density are

$$T_f/T_i = c^{2(1-1/\gamma)}, \quad n_f/n_i = c^{2/\gamma}$$

The most important ingredient in this model is to associate an empirical scaling law[5][6]

$$\tau_N \propto R^2/\rho_i,$$

with the axial compression. The change of ρ_i and τ_N with the compression is written as follows.

$$\rho_f/\rho_i = c^{-1/\gamma}, \quad \tau_{N_f}/\tau_{N_i} = (x_f/x_i)^2 c^{1/\gamma}(r_{T_f}/r_{T_i})^{-1/2}$$

where, $r_T = T_i/T$ (T: pressure balance temperature, T_i: ion temperature). The results of this analysis are shown below. In Fig.1(a), (b) and (c), x_f/x_i, T_f/T_i and τ_f/τ_i are plotted against l_f/l_i for some initial x_s values. As is seen in the figure, the heating done by the axial compression is modest because of the one dimensional nature of the compression and also possibly the existence of an upper limit to compression, perhaps due to the tilt instability[7]. The important point is that simultaneous heating and improvement of confinement is predicted for this method of compression.

3. Apparatus

The FRC is produced in the formation region of the FRC Injection Experiment (FIX) machine. The formation region is 1.26m long, 0.155m radius theta pinch with independently driven mirror coils at both ends. The FRC is then translated into a 3.4 m long, 0.8 m diameter confinement region made of stainless steel, equipped with mirror fields at both ends. The FRC translated into the metal chamber bounces back and forth a few times and settles down

in the confinement region[8]. Typically, the electron density of the translated FRC plasma is about $5 \times 10^{19} m^{-3}$ and the pressure balance temperature is about 150eV at 150μs and decays to 50eV at 400μs. Axial compression of the FRC is done by energizing additional segmented mirror coils successively with time in such a way as to shorten the length of the confinement region. The rise time of the additional mirror field should be slow enough to accomplish a soft compression but faster than plasma decay times. In our case, the rise time was chosen to be 30-50 μs. As this rise time is shorter than the skin time of the metal confinement chamber, the additional mirror coils must be installed in the vacuum chamber. The additional mirror coils are arranged in two segments, each segment consisting of a 0.66m diameter 3-turn winding, each of which is contained in a stainless-steel jacket separated by 0.2m axially. Each jacket consists of two halves, separated by an insulator to prevent azimuthal return currents from flowing. The individual coil segments are spaced at 0.2m intervals along the machine axis. These coils are arranged next to the upstream mirror region. The length of the confinement region can be shortened from 3.4 m to 2.4 m [9]. A schematic drawing of the apparatus is shown in Fig.2.

4. Experiment

An axial compression experiment was done on the FRC injection experiment (FIX) machine. The additional mirror coils were energized when the movement of the FRC plasma associated with the translation ceased. The separatrix shape and its change with time during the compression is inferred from an axial array of diamagnetic probes arranged in the confinement region. The separatrix shape near the additional mirror coils is not obtainable when the coils are energized, because the magnetic field is assumed to be almost straight in calculating r_s [10]. In Fig.3, the change of separatrix radius with time is shown for the case with and without compression. The measurement was made, in the case without compression, at the axial midplane of the confinement region and with compression, 0.6m downstream from the midplane. These positions were chosen in such a way that the axial midplane of the FRC itself was near the measurement position after the movement of the plasma associated with translation ceased in the former case, and after the compression in the latter case.

In the case of compression shown in Fig.3, two sets of additional mirror coils were energized at the same time. The magnetic field was increased from 0.04T to 0.08T in 35μs and the length of the FRC was decreased from 3.4m to 2.4m by about 30%. The wavy structure before 200μs is due to the movement of the FRC plasma associated with translation. Without the compression, r_s is seen to decrease monotonically after 200μs. While, with the compression applied at 230μs, r_s increased from 248μs to 266μs and then started to decay after that period. The apparent change in decay rate is seen at 310μs. Before that time, deformation of the FRC caused by compression was seen; a part of the FRC near the downstream mirror field swelled and then the swelling disappeared. After 310μs, the FRC decayed almost uniformly without appreciable irregularity in shape. After all, the configuration life time of about 500μs increased by about 50μs. In the theoretical analysis, the decay process was neglected and therefore r_s takes a different but constant value before and after the compression. In this case the improvement of τ_N can be concluded by simply comparing τ_N before and after the compression. However the following two facts complicate the comparison between analysis and experiment: i) r_s decreases with time as a result of unneglectable loss of plasma particles, energy and trapped magnetic flux: ii) Transport times change with time. To overcome these difficulties and to see the change in confinement due to compression, experimental τ_N was plotted against the confinement time predicted from the empirical scaling law (Fig.4). The experimental τ_N is obtained at each instance of time by

$$\tau_N = \left((dN/dt) \ /N \right), \quad N = \bar{n}V$$

V is calculated from the measured $r_s(z)$ and as $\bar{n}$ we used a quantity obtained by dividing a side-on interferometer signal by r_s measured at the interferometer location. Without compression, experimental τ_N is longer than predicted τ_N by a factor of about 5 as already noted in Ref.[4]. However the functional dependence of τ_N on R^2/ρ_i still holds approximately:

The discrepancy of the proportionality constant at τ_N=60μs and 150μs is a factor of about 2. With compression, before 327μs, experimental τ_N exceeds that of the case without compression considerably. Probably due to the deformation of the FRC associated with the compression, the measurement may not be done correctly. When the FRC is decaying uniformly, experimental τ_N with compression almost coincides with the no compression case (maximum deviation is only 12%).

5. Disussion

So far, we have compressed the FRC axially by about 30%. If we compress the FRC further, the dependence of τ_N on the plasma length and radial magnetic field profile may appear chearly. The existence of a 35μs offset in the curve of τ_N-experiment versus τ_N -scaling, which is equivalent to a 50eV D^+ ion transit time along the half-length of the FRC, may suggest that particle transport along open field lines outside the separatrix plays an important role in FRC confinement, and may yield a dependence of τ_N on l_s. Experimental evidence that the confinement was improved by the compression suggests that the dependence of τ_N on l_s should be small. Even a dependence like $\tau_N \propto l_s^{1/2}$ makes r_s to decrease with compression.

Our model, in which the compression is done sufficiently faster than transport times, predics that r_s increases 15% from r_s~16.0cm to r_s~18.4cm, when it is axially compressed by 30%, with a consequent increase in τ_N of 16%. Experimentally, without compression, r_s near the midplane decreased from 16.2cm at 230μs to 15.2cm at 248μs and further to 14.4cm at 266μs. With compression, r_s started to increase from 15.2cm at 248μs and attained its maximum value of 16.4cm at 266μs.

The increase of r_s from the time when the axial compression field was triggered and the time when r_s started to increase was 1% and 8%, respectively. The difference of r_s at the time when r_s became maximum under compression and that of the case without compression at the corresponding time was 12%. This value is close to the value of 15% predicted by the model if we assume that the compression was done quickly at 266μs. A more careful analysis in which the effects of compression and transport loss are taken into account will be required to make reliable comparisons with the experiment. The effect of the deformation of the FRC by compression - the dynamics of the compression -may also have to be taken into consideration. Even given the crudeness of the model, a comparison of r_s at 266μs with and without compression, demonstrates that compression was achieved.

If experimental τ_N with and without compression obeys the same scaling law, as was approximately shown by experiment, the increase in FRC life time because of compression even if r_s changes in time due to unneglectable losses, can be explained as follows: τ_N decreases gradually with time when r_s decreases due to unneglectable loss. Axial compression brings the FRC to a state with larger r_s and, therefore, longer τ_N . The magnetic field B_w between r_s and the chamber wall increases with r_s because the magnetic flux is conserved. This increase of B_w has a stronger influence on ρ_i than the increase of T_i by compression in such a way to decrease ρ_i. This also tends to increase τ_N . When the compression ends, the FRC starts to decay again from this state with improved confinement.

6. Conclusion

A new method for the axial magnetic compression of an FRC plasma in a flux conserver is proposed. The ability of this scheme to heat as well as improve FRC plasma confinement was predicted by taking into account both the empirical scaling law and the adiabatic compression relations. An experimental apparatus to test this concept was built and was installed on the FIX machine. Reflecting the smallness of the compression ratio, heating was not recognized but improvement of confinement was observed by the experiment.

References

[1]   Tuszevski, M., Field Reversed Configurations, Nuclear Fusion **28** (1988) 2033-2092
[2]   Ohtsuka, T., Okubo, M., Okada, S., Goto, S., Particle end loss in the edge plasma of a field-reversed configuration, Physics of Plasmas, **6** (1998) 3649-3655
[3]   Rej, D. J., Taggart, D. P., Barn, M. H., Chrien, R. E., Gribble, R. J., Tuszewski, M., Waganer, W. J., Wright, B. L., High-power magnetic-compression-heating of field-reversed configurations, Phys. Fluids, **B4**, (1992) 1909-1919
[4]   Okada, ., Taniguchi, H., Sagimori, H., Himura, H., Hase, M., Yoshida, R., Okubo, M., Sugimoto, S., Goto, S., Heating of Plasma with Field Reversed Configuration by a Fast Rising Magnetic Pulse, Fusion Energy 1996, (Proc. Conf. Montreal, 1996), vol.2, 229-236, IAEA, Vienna, 1997
[5]   McKenna, K. F., Armstrong, W. T., Bartsch, R. R., Chrien, R. E., Cochrane, J. C., Kewish, R. W., Klinger, P. L., Linford, R. K., Rej, D. J., Sherwood, E. G., Siemon, R. E., Tuszewski, M., Particle confinement scaling in Field Reversed Configurations, Phys. Rev. Lett. **50**, 1787-1790 (1983)
[6]   Tuszewski, M., McKenna, K. F., Interpretation of end-on interferometry in field-reversed configurations, Phys. Fluids, **27** (1984) 1058-1060
[7]   Ishida, A., Shibata, N., Steinhauer, L. C., Local modes of field-reversed configurations, Phys. Plasmas, **1**(1994) 4022-4031
[8]   Himura, H., Okada, S., Sugimoto, S., Goto, S., Rethermalization of a Field-Reversed Configuration Plasma in Translation Experiments, Phys. Plasmas, **2** (1995) 191-197
[9]   Kitano, K., Matsumoto, H., Yamanaka, K., Kodera, F., Yoshimura, S., Sugimoto, S., Okada, S., Goto, S., Advanced experiments on Field-Reversed Configuration at Osaka, Proceedings of the 1988 International Congress on Plasma Physics combined eith the 25th EPS Conference on Controlled Fusion and Plasma Physics, ((Proc. Conf. Prague, 1998), in press
[10] Tuszewski, M., Excluded flux analysis of a field-reversed plasma, Phys. Fluids, **24** (1981) 2126-2127

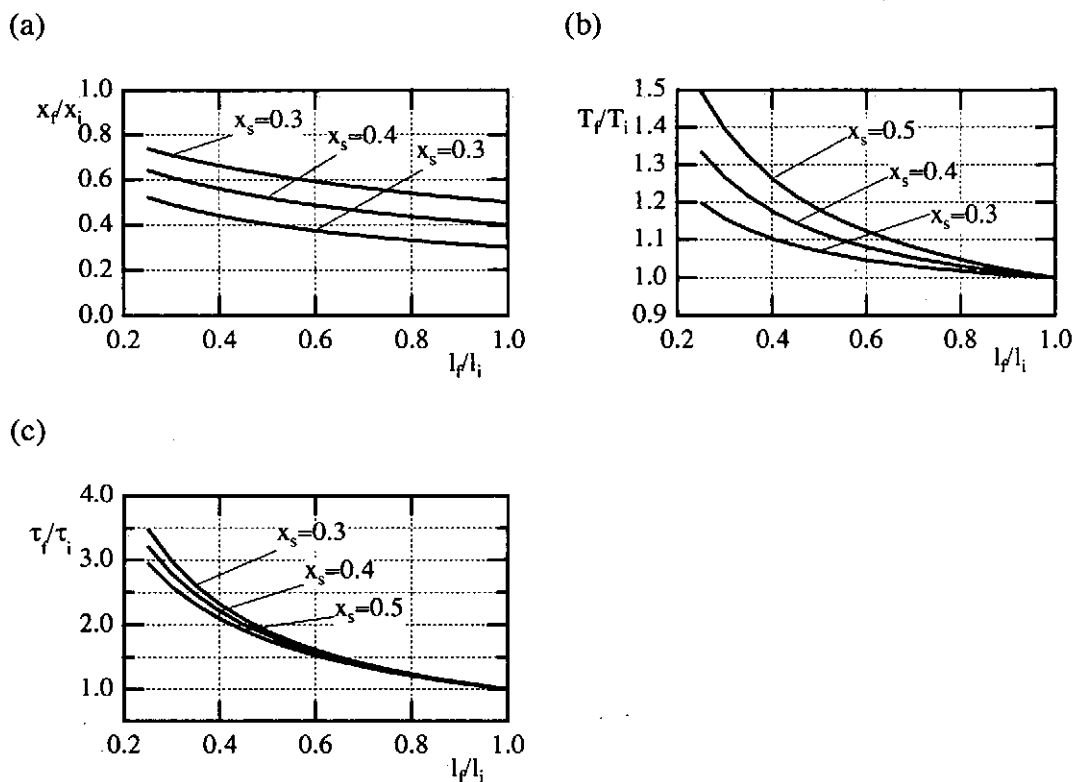This work is intended to be a preprint for the 17th IAEA Fusion Energy Conference.

(a)

(b)

(c)

Fig.1 (a) Change of separatrix radius by axial compression for different initial x_s values.
  (b) Effect of heating by axial compression.
  (c) Effect of confinement improvement by axial compression.
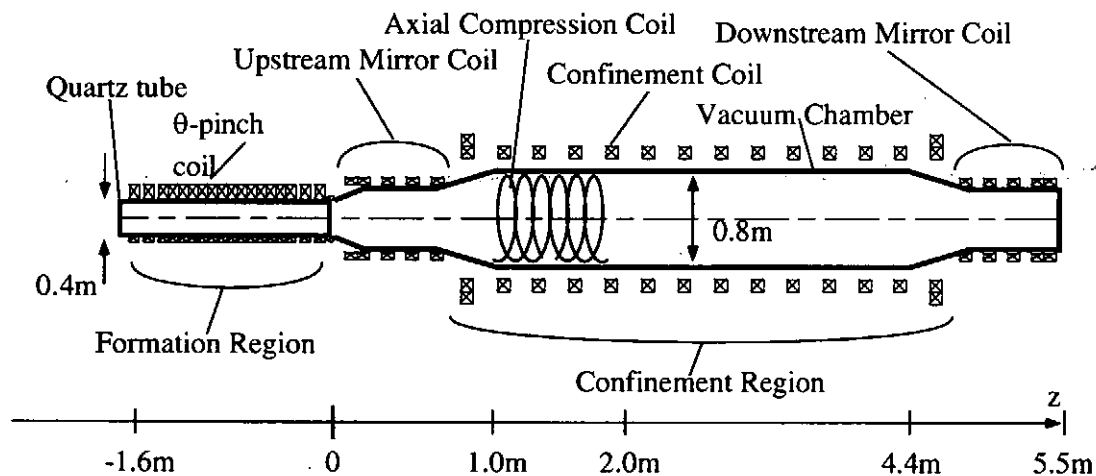
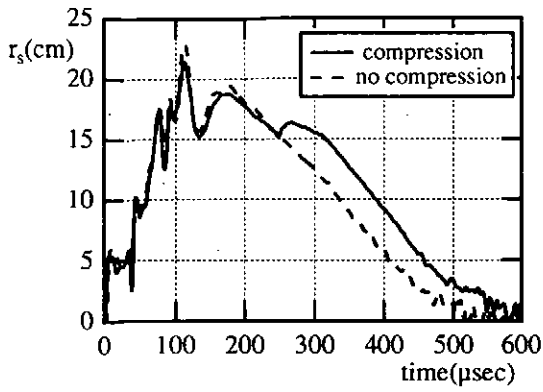

Fig.2
  Schematic drawing of the FIX machine.

Fig.3 Change in separatrix radius with time at 0.6m downstream from the axial midplane of the confinement region. Dashed line: no compression. Solid line: axial compression field applied at 230μs.
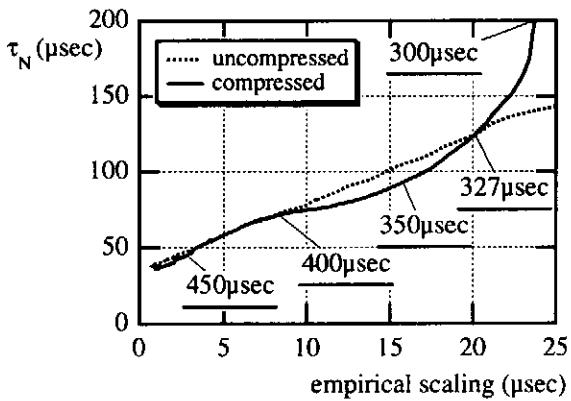

Fig.4 Particle confinement time at each instant of time plotted against the value calculated for the empirical scaling law with (solid line) and without (dotted line) axial compression.

First experimental result of toroidal confinement of non-neutral plasma on Proto-RT

H. Himura, Z. Yoshida, J. Morikawa, Y. Ogawa, C. Nakashima,
H. Kakuno, N. Shibayama, S. Tahara, S. Kondo, M. Iqbal,
M. Hashimoto, T. Hirotsu, K. Takemura
University of Tokyo, Hongo, Bunkyo ward, Tokyo 113-8656, Japan

S.M. Mahajan
University of Texas, Austin, Texas 78712, U.S.A.

Abstract

Recently, an internal-ring device named Proto-RT (Prototype Ring Trap) was constructed at University of Tokyo, and experiments on the device have been just initiated. The goal of Proto-RT is to explore an innovative way which has a possibility to attain a plasma equilibrium with extremely high-β ($\beta > 1$) in a toroidal geometry using non-neutral condition. At the first series of the experiments, pure electron plasma ($n_e \sim 10^{12}$ m^{-3}) is successfully confined inside a separatrix. No disruption is so far observed. The confinement time of the electron plasma is the order of 1 sec. A shear effect of magnetic fields seems to result in longer confinement. The non-neutrality of $\Delta n_e \sim 10^{12}$ m^{-3} is already beyond the value required to produce an enough self-electric field E in plasma, causing a strong $E \times B$ flow thoroughly all over the plasma where the hydrodynamic pressure of the flow is predicted to balance with the thermal pressure of the plasma.

I. INTRODUCTION

A possibility of high-β equilibrium with strong flow has been theoretically pointed out [1], which is based on double-curl Beltrami field. In fact, several high-β solutions have been numerically found out in a cylindrical geometry. The requirement to this high-β equilibrium is to maintain two-fluid effects with the large velocity field whose magnitude is comparable to that of the magnetic field in plasma. Another significant feature of this equilibrium is that the thermal pressure of plasma is sustained by the hydrodynamic pressure of the strong flow, alleviating the strength of magnetic fields to confine plasma which offers attractive benefits including the lowest construction costs among toroidal fusion systems.

To obtain such a flow in plasma, a non-neutral condition is proposed [2] which can produce a self-electric field E in plasma, causing strong $E \times B$ shear flow if we apply an appropriate magnetic field B there. Then the question is asked on how the non-neutral plasma can be produced in laboratory experiments. Although several methods can be considered, we have proposed to add quasi-neutral plasma to pure electrons. To explore this way, the toroidal confinement of pure electron plasma has been conducted on Proto-RT. A description of the Proto-RT device and the diagnostics employed are explained in Sec. II. The first experimental data of pure electron plasma and a summary are given in Sec. III and IV, respectively.

II. APPARATUS OF PROTO-RT DEVICE

An internal-ring device named Proto-RT (Prototype Ring Trap) has been constructed to investigate the fundamental physics of (1) non-neutral plasma, (2) magnetic null, and (3) traps for positrons or antiprotons in a static magnetic field B. The primary objective of Proto-

RT is the study of toroidal confinement of pure electron plasma inside a closed **B** region as portrayed in Fig. 1, and chaos-induced anomalous resistivity in field null [3].

Figure 2 shows a schematic view of the Proto-RT device. A 1.18 m inner diameter and 0.90 m long vacuum vessel, which is made of 1.0 cm thick stainless steel (SUS304), contains an internal-ring (30.0 cm major radius and 4.3 cm minor radius) and a center stack with 11.4 cm outside diameter. The internal-ring, 6 mm thick stainless steel, has one toroidal and four poloidal cuts which present to help smooth flux surfaces around the ring. Inside the ring, there is a 175 turn copper wire with 3.2 mm diameter to produce a dipole-field (DF), and each of which is stiffen together with an epoxy. Two copper veneers are inserted into the coil as fins. Also, Freon is applied to cool the coil down. The Freon circulates in toroidal direction of the coil through a quarter-inch stainless tube that is attached to the fins. Furthermore, He_2 gas is filled up inside the ring to promote the heat conduction there. Both the tube and the gas are introduced in the internal-ring through the same bus-bar; In fact, there are two bus-bars on the internal-ring. The another one is used to energize the coil. To hold the ring with the bus-bars, a set of eight stainless steel rods having 3 mm diameter is used to connect the ring with the center stack. A ceramic tube covers each rod.

The inner diameter of the center stack, 4.0 mm thick stainless steel, is 10.6 cm through which a set of six toroidal-field (TF) coils passes in order to carry poloidal currents, being linked with the vacuum vessel. Each TF coil has ten-turn which is made of copper boards (1 mm thick each), and is cooled down by water. A vertical-field (VF) is added to produce a magnetic separatrix.
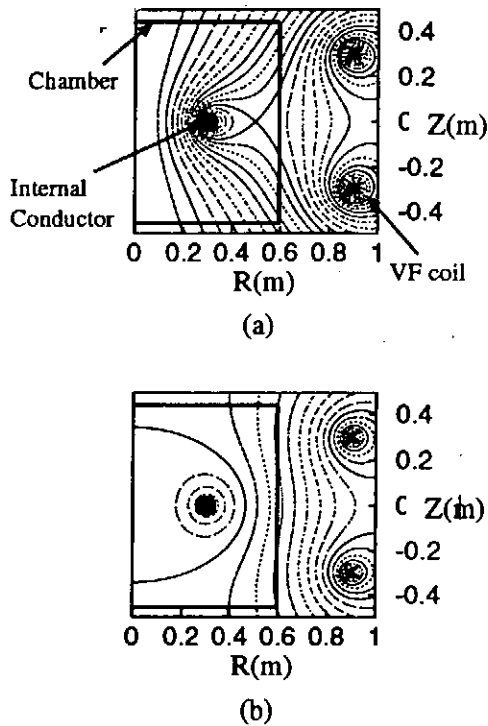

FIG. 1. Two types of magnetic surfaces; (a) The separatrix generates an X-point on the outside of the internal conductor. (b) The magnetic null points are located on the center axis.
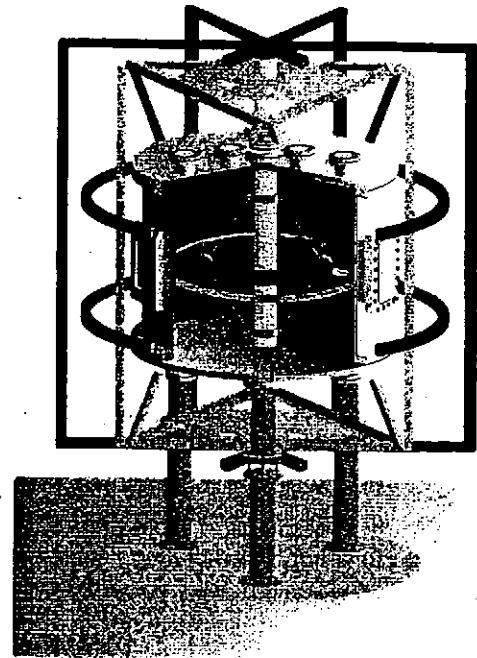

FIG. 2. Schematic view of Proto-RT; a toroidal non-neutral plasma confinement device. Dipole magnetic field is produced by an internal ring conductor. Toroidal magnetic field yields sheared magnetic field.
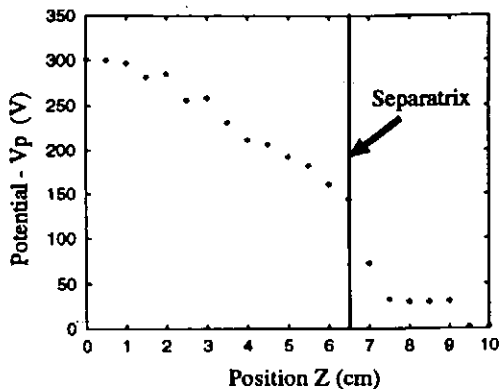
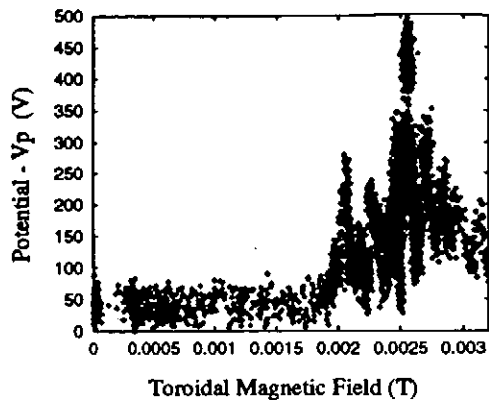FIG. 3. Radial distribution of the electrostatic potential in a pure electron plasma.

FIG. 4. Dependence of the confined plasma potential to the toroidal magnetic field.

Proto-RT uses three DC power supplies, (1) TF: 50 V · 500 A, (2) DF: 60 V · 60 A, (3) VF: 60 V · 30 A×2, to form a well-controlled static **B**. By properly programming these currents, we can flexibly create various magnetic configurations as shown in Fig. 1. The vacuum vessel is pumped down to $3\text{-}4 \times 10^{-7}$ Torr for the present experimental research. In Proto-RT, radio frequency of 13.56 MHz (up to 1 kW) is available to launch an electromagnetic wave to plasma through a toroidal loop antenna having 1.0 m diameter. An electron gun is installed at $z = 0$ to inject electrons which can be accelerated up to 2.0 kV. The head of the gun is movable in not only the radial direction but also the tangent plane perpendicular to $r\text{-}z$ plane.

Regarding to diagnostics of Proto-RT, two potential probes are now used to measure electrical potentials $-\Phi$ of pure electron plasma from which number of electron density n_e can be inferred. An array of probes having semiconductor tips and electrodes will be installed to determine static **B** and **E** simultaneously. A conventional Faraday cup is used to provide electron energy E_e. Also, a directional faraday cup is now being built to measure precise electron flow flux $n_e v_f$.

III. FIRST RESULT OF PURE ELECTRON PLASMA

Since the TF coils were completed in January of 1998, we have performed the first experiments to confine pure electrons in the separatrix shown in Fig. 1 (a). Electrons are injected from the electron gun which is placed near the X point. Plotted in Fig. 3 is a profile of $-\Phi$ along the z axis. Each data is taken in separate shots and the head of the electron gun is set just inside the separatrix for the profile in Fig. 3. The value of $-\Phi$ is about 300 eV at $z = 0$, and then monotonically decreases to $\sim$ 150 eV at the separatrix ($z = 6.5$ cm). It should be noted that a steep gradient of $-\Phi$ appears at the separatrix, indicating that the electrons are well confined inside the separatrix. Assuming there is no positive charge there, the value of n_e can be calculated to be $\sim 10^{12}$ m^{-3} from $\nabla^2 \Phi = e n_e / \varepsilon_0$.

The value of $-\Phi$ strongly depends on the strength of B_r. It is recognized from Fig. 4 that $-\Phi$ inside the separatrix is about 50 V without B_r. However, as B_t is applied, $-\Phi$ significantly increases up to $\sim$ 500 V ($B_t \sim$ 25 G), implying that a shear effect of **B** results in longer confinement of pure electrons inside the separatrix. This might be attributed to

suppression of microturbulence by a magnetic shear. In fact, a preliminary measurement of electrostatic fluctuations provides the frequency in range of $10^6 - 10^7$ Hz with the magnitude of 10^{-3} of the ambient potential, and the value of $\tilde{\Phi}/\Phi$ seems to decrease as B_t is applied up to 25 G.

Finally, from the decay signal of the potential probes, we can estimate the confinement time τ_N of pure electrons. The value of τ_N is the order of 1sec.

IV. SUMMARY

In summary, we have completed to construct an internal-ring device, Proto-RT. The magnetic field B of Proto-RT is static so that experiments on the device can be performed in well-controlled laboratory setting. Moreover, the device has a great flexibility to produce various B configurations such as a closed-field configuration with X point, Spherator type, and Dipole fields. Those properties allow us to investigate fundamental physics of (1) magnetically confined plasma, (2) trapping of antimatter, (3) anomalous resistivity in magnetic null and so on. Regarding to (1), the experiments to confine pure electron plasma have been just initiated, and the value of $n_e \sim 10^{12}$ m^{-3} seems to be attained inside a separatrix. No disruption of pure electron plasma is so far observed. The confinement time of the electron plasma is inferred to be the order of 1 sec. A shear effect of magnetic fields results in longer confinement of the plasma. According to a simple calculation based on the generalized Bernoulli's law [1, 2], such non-neutrality of $\Delta n_e \sim 10^{12}$ m^{-3} is already enough to attain $\beta_{center} \sim 3.5$. Thus, a plan to inject a high-pressure quasi-neutral plasma to the pure electrons is now going on to explore the expected high-β equilibrium with flow.

[1] S.M. Mahajan and Z. Yoshida, Phys. Rev. Lett. **81** (1998) 4863.
[2] Z. Yoshida *et al.*, in *Proceedings of 17th IAEA Fusion Energy Conference* (IAEA), IAEA-CN-69/ICP/10 (R) (1998).
[3] Z. Yoshida *et al.*, Phys. Rev. Lett. **81** (1998) 2458.

Physics of Fat Current Carrying Tori and Proposed Program SPIRIT
[Self-organized Plasma with Induction , Reconnection, and Injection Techniques]

M. Yamada, H. Ji, R. Kulsrud, C.Z. Cheng, D. Mikkelsen, H Himura and S. Zweben
Princeton Plasma Physics Laboratory, Princeton, N.J. 08543

In this paper the recent primary results from the Magnetic Reconnection Experiment (MRX) are discussed with their relationship to the current carrying pinch discharges such as spherical torus, spheromak and field reversed configurations. The basic scenario of a new fusion concept exploration project, SPIRIT will be also discussed. This proposed experiment will enable us to explore important new regimes of high-beta compact toroid(CT) plasmas with a special focus on field reversed configurations (FRCs). Compact toroid plasmas can be generated by merging co- and counter-helicity spheromaks produced by inductive discharges utilizing flux cores. A particularly attractive feature of this project is the capability to investigate systematically the MHD stability and confinement features of compact high beta plasmas with large trapped flux over a wide range of the key parameters. s^* ($=R_s/\rho_i$), the ratio of plasma size to ion gyro-radius and the plasma elongation ($0.5 < E < 4$. Large variations in $s^* = 4\text{-}60$ ($<s> = 1\text{-}15$) are made possible by counter-helicity merging of two spheromaks to form FRCs. In addition, this project can accommodate a neutral-beam injection(NBI) of a few megawatts to extend the lifetime of the plasma for much longer than one millisecond. This aspect will significantly broaden the scope of the experiment by enabling active control of plasma stability with toroidal rotation and also by providing an additional current drive and beam heating. This NBI would induce a plasma spinning with high velocity of up to the order of $V_{Alfvén}$, which would in turn help stabilize the global MHD modes. Recently a new equilibrium code has been developed at PPPL to assess the stability properties of the FRC configuration with a sheared rotation. NBI would also decrease the value of s. This experiment will have a significant merit for a study of the boundary regime between FRC and other compact roroid plasmas elucidating their key confinement physics issues.

Recent Progress of Merging Experiments in TS-3 and TS-4

Yasushi Ono, Michiaki Inomoto, Yoshinobu Ueda and TS-3 & 4 groups
Department of Electrical Engineering, University of Tokyo

Abstract

Merging formation of field-reversed configuration (FRC) explored not only a new scenario of highly-efficient FRC formation/amplification experiment but also a new boundary research between FRC, spheromak and spherical tokamak (ST). A new finding is that the produced FRC is transformed stably into an ultra-high-ß ST by applying external toroidal field $B_{t,ext}$. The toroidal field was observed to vanish around magnetic axis after the $B_{t,ext}$ application to the FRC, indicating formation of diamagnetic ST. The hollow current profile of FRC was maintained during the equilibrium transition, eliminating the need for the difficult hollow-current-formation process of start-up discharge of high-ß ST. The energy-conversion effect of merging transforms the force-free merging spheromaks with paramagnetic current into the FRC with diamagnetic current and the further application of $B_{t,ext}$ the FRC into the ultra-high-ß (>60%)/diamagnetic ST, indicating the close relationship between FRC and ST in second stability.

1. Introduction

A novel merging formation of FRC has been developed in the TS-3 merging experiment at University of Tokyo[1-3]. As shown in Fig.1, two force-free (low-ß) spheromaks with opposing toroidal magnetic field B_t were axially collided and were transformed into an oblate FRC with $B_t \approx 0$ and ß≈0.6-1[1-3]. The toroidal magnetic energy of the low-ß spheromaks was successfully transformed into the ion thermal energy of the high-ß FRC by use of energy conversion effect of magnetic reconnection[2]. This unique method has various advantages over the conventional fast theta-pinch formation: (1) slow formation, (2) stable and highly-efficient formation, (3) large ion heating power of merging and (4) current drive by ohmic heating coil or by continuous merging. The produced FRCs have high-ß >0.6 (>>0-0.1: spheromaks), ion temperature $T_i \approx 100$-200eV much higher than electron temperature $T_e \approx 20$eV and small elongation factor ε: 0.8-1 (<<5-20: conventional FRCs). This equilibrium transition indicates the importance of boundary research between the paramagnetism of spheromaks / low-ß STs and the diamagnetism of FRCs / high-ß STs. This paper addresses two important issues on this boundary research: (1) how different the high-ß FRC equilibrium is from that of low-ß spheromak equilibrium and (2) whether the produced FRC can be transformed to a high-ß/diamagnetic ST in the second stability or not. The high-ß ST formation through FRC indicates the close relation between high-ß ST and FRC. This new method is useful to optimize the CT configuration for higher ß, better stability and longer confinement time.

2. Experimental Setup

The TS-3 merging device was used to study the boundary between FRC, spheromak and ST. Its cylindrical vacuum vessel with length of 1m and diameter of 0.8m has two poloidal (PF) coils and two sets of eight electrode pairs to form two spheromaks with opposing B_t. Their polarities of B_t were determined by those of the electrode discharge currents. A center stack of torus and OH coils (diameter≈0.12m) was inserted along the geometric axis to produce external toroidal field for ST operation and volt-second for current sustainment of CTs. Each produced spheromak has major radius R≈0.18-0.22m, aspect ratio A≈1.5, $T_i \approx T_e \approx 10$eV, $n_e \approx 2$-50×10^{19}m^{-3} and B<2kG. Merging speed of the two
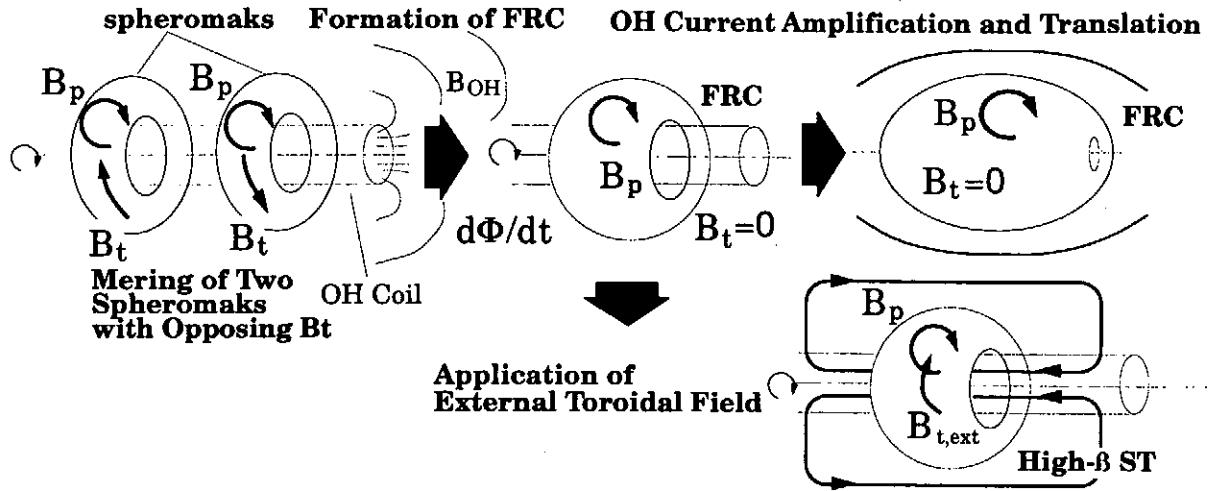
FIG. 1 FRC merging formation / OH current-amplification and
application of external toroidal field (formation of High-ß ST/FRC)

spheromaks was controlled by magnetic pressure of the PF coil currents and separation coil currents on the midplane. A 2-D array of magnetic probe composed of 200 coils was inserted on r-z plane of the vessel to measure directly the 2-D magnetic field profile. The poloidal flux contours, current density etc., were calculated based on this measurement. A polichrometer with optical multichannel analyzer was used for Doppler broadening measurements of spectrum lines to obtain radial profile of T_i. An electrostatic probe was inserted to measure the T_e profile and the n_e profile which was calibrated by the CO_2 laser interferometer.

3. Experimental Results
3.1 Transition from Spheromak to FRC during FRC Merging formation

Figures 2 show the poloidal flux/B_t contours, the radial profiles of B_t and the toroidal current densities j_t of the initial merging spheromak (a) and the produced FRC (b), which were obtained from the 2-D magnetic field measurement. The opposing B_t of two spheromaks were observed to vanish in agreement with the formation of an FRC without B_t. As already reported in Ref.[2], the particle acceleration effect of magnetic reconnection converts this toroidal magnetic energy into the ion thermal energy of the FRC. It is noted that the merging process transforms the peaked j_t profile of the spheromak to the hollow one of the FRC. This hollow j_t profile agrees with the theoretical prediction[4] and is needed to sustain the high thermal pressure of FRC. Its thermal pressures calculated both from $\nabla p = j \times B$ and T_i, T_e and n_e measurements were about five times larger than that of the spheromak.

Figure 2(c) shows $h = (j_t/r)_r = R/\langle j_t/r \rangle$ factor calculated from the j_t profile, as a function of X_s (=radius ratio of separatrix to conductive shell). The h values of our oblate FRCs is located along the line of the conventional FRC scaling deduced from n_e measurement[4]. This fact indicates that our oblate FRC is similar to the conventional prolate FRCs in the high-X_s regime. However, j_t of our FRC was found to vanish sharply around the separatrix, unlike the theoretical models of FRC whose j_t were often assumed to be finite at the separatrix.

3.2 Boundary between FRC and High-ß ST
(Ultra-High-ß ST Formation by Use of FRC)

Recently, we found that the oblate FRC can be transformed into a new high-ß equilibrium of ST. Our basic idea is shown in Fig. 3(a): typical q_ψ-p_ψ (s-α) diagram of ST for ballooning instability (q_ψ: shear parameter, p_ψ: pressure gradient). Because of strong toroidal effect, it has the narrow window between the first and second stability regimes, unlike those

of the conventional tokamaks[6]. It has been studied how low-ß STs in the first stability regime can be transformed into high-ß STs in the second stability regime through this narrow window. However, it is easier to transform the oblate FRC to the high-ß ST in the second stability regime, because the FRC with ß≈1 is located near this regime. We demonstrated this new type of high-ß ST formation by applying the external toroidal field $B_{t,ext}$ to the FRC, as shown in Fig. 1.

Figures 3(b) show the 2-D contours of poloidal flux and toroidal field amplitude and radial profiles of j_t and thermal pressure p calculated from $\nabla p = j \times \mathbf{B}$, after $B_{t,ext}$ was applied to the FRC right after its merging formation. The OH current drive was also used to maintain the flat top of plasma current. The poloidal flux and B_t contours indicate that the FRC without B_t is transformed stably into a new ST with finite B_t. Its life time≈100μsec is even longer than that of the produced FRC. More than 80% of the thermal pressure of FRC was maintained after the B_t application, indicating that no serious instability occurs during this equilibrium transition. The hollow j_t profile also lasted to sustain the high thermal pressure of the high-ß ST, as shown in Fig. 3(b). The sustained ß≈0.6 is much higher than the conventional ß of ST. Figures 4(a) and (b) show the radial B_t profiles of the high-ß ST transformed from FRC and the conventional ST. Note that the B_t profile (solid line) of the former ST is located in the diamagnetic side of the vacuum B_t profile (dotted line) in sharp contrast with the peaked B_t profile of the latter ST. The poloidal beta of the former is estimated as high as 1-1.2. Our new formation method was found to fully suppress the strong paramagnetism of ST probably by virtue of the new path to the high-ß ST shown in Fig. 4(a). These results indicate that this high-ß ST is much closer to the FRC than to the paramagnetic ST.

4. Conclusions

Our merging formation of FRC lead us to the new generation of oblate FRC experiment with high energy efficiency and current amplification. It also explored the new possibility of ultra-high-ß ST formation by use of FRC. All these results indicate the importance of studying the relationship between various CTs, especially FRC, high-ß ST, spheromak and low-ß ST. Our FRC/ST experiment has been made to optimize the stability/confinement properties of CTs, because the FRC has high ß characteristics and ST has better stability and confinement. This motivation lead us to the construction of a new upgraded confinement device TS-4 for the boundary research of CT confinements and their merging. It has two flux cores for two CT production in its cylindrical vacuum vessel with length of 2.5m and length of 1.9m. Two CTs with major radius ≈0.5m, A≈1.2-1.5 and B_t≈3-5kG will be merged together for high-ß FRC/ST formation and heating. Our merging formation of FRC has been recently adopted by several US experiments: MRX, SSX, Swift-FRC and SPIRIT as a promising slow formation method of FRCs.

References

[1] ONO Y. et al., Plas. Phys. Cont. Nucl. Fus. Res. 1992 , 2, 619, (1993).; ONO Y., Trans. Fus. Tech. 27, 369, (1995).
[2] ONO Y. et al., Phys. Rev. Lett. 76, 3328, (1996); ONO Y. et al., Phys. Plasmas 4, 1953 (1997); ONO Y. et al., Phys. Fluids B 5, 3691, (1993).
[3] ONO Y. et al., Plas. Phys. Cont. Nucl. Fus. Res. 1996, 2, 263.
[4] STEINHAUER R. et al., Phys. Fluids B 4, 645, (1992).
[5] HORIUCHI R., SATO T., Phys. Plasmas 4 277, (1997).
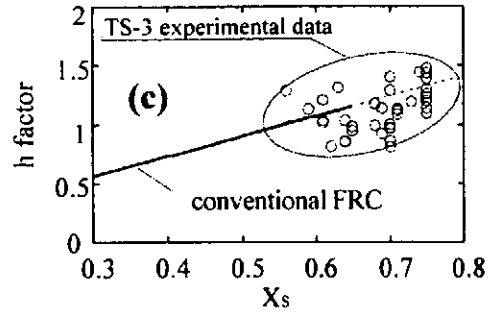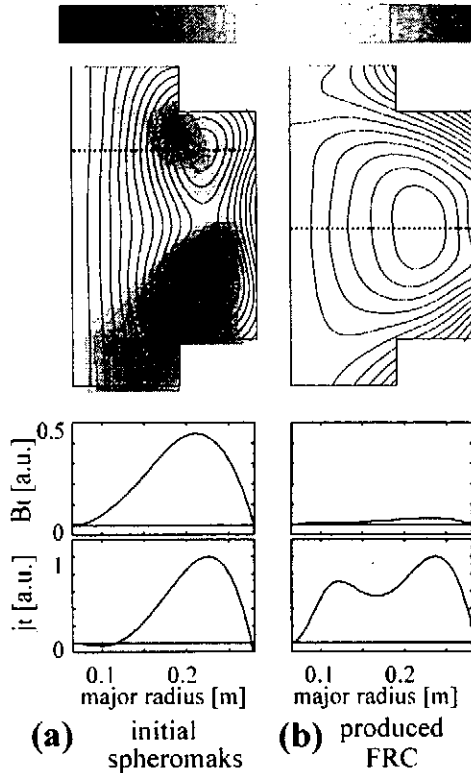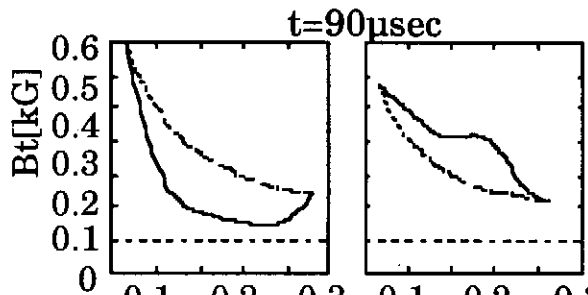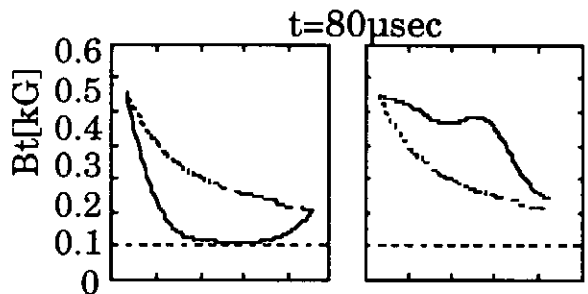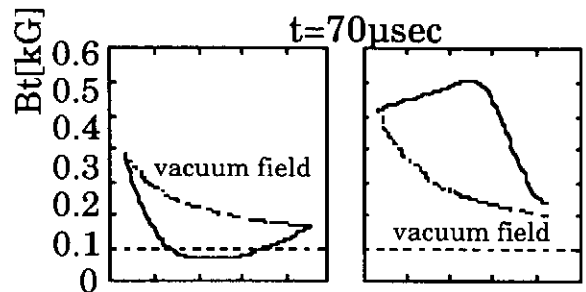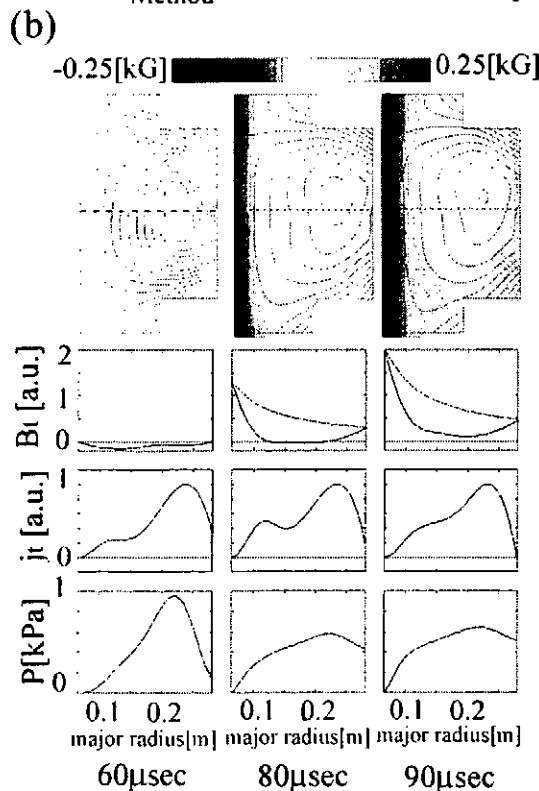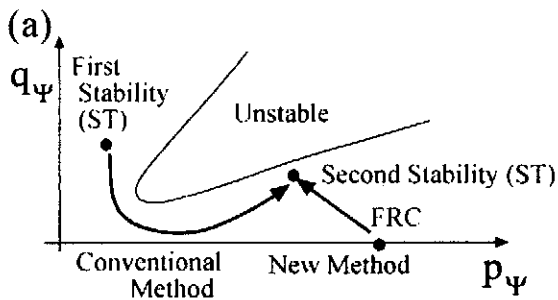[6] MILLER R. L., et. al., Phys. Plasmas. 4, 1062, (1997).

FIG. 2 Poloidal flux contours and radial profiles of B_t, j_t of the initial spheromaks (a) and the produced FRC (b), and the FRCs in h-X_s space (c).

FIG. 4 Radial B_t profiles of high-ß ST (a) and conventional ST (b).

FIG. 3 Basic idea of forming high-ß ST in s-α diagram (a), r-z contours of poloidal flux and toroidal field strength and radial profiles of B_t, j_t and thermal pressure p of the FRC and the produced high-ß ST (b).

High-Beta Spherical Tokamak Formation by Use of Merging Phenomenon

Yoshinobu Ueda and Yasushi Ono
Dept. of Electr. Eng., Univ. of Tokyo

Abstract

Novel high-power heating experiment of compact torus (CT) has been developed in the TS devices by use of merging effects. This method enables us to inject whole magnetic and thermal energies of a colliding CT into a target CT within short reconnection time. The maximum heating power of 10MW was obtained in our initial low-field (0.03-0.08T) and small-scale ($R < 0.2$m) experiment. This heating energy is provided mostly by ion acceleration effect of magnetic reconnection. The ion heating energy as well as the merging speed increases with decreasing the q-value (B_t component) of two toroids. The merging process causes the β-values of CTs to increase by factor 2-3 and the poloidal β increment increases with increasing the q-value of CT.

1 Introduction

The TS (Tokyo Univ. Spherical Torus) experimental group has been investigating various merging phenomena of CTs (STs, spheromaks and RFPs) and their applications, using the TS-3 merging device. Its main objects are (1) 3-D investigation of magnetic reconnection and its application, (2) comparison of various CTs in a single device and (3) merging formation of FRC and its application to ultra-high-β ST formation. The high-power heating of CT is one of the major applications of reconnection effects to fusion plasmas [1]-[4]. As shown in Fig. 1, the produced CT is collided with the target CT in the axial direction. Their reconnection is expected to heat plasma through its particle acceleration effect [4]. This heating method is unique, because whole magnetic/thermal energy of the colliding CT can be used for heating of the target CT within short merging/reconnection time [5]. Unlike the other heating methods, it will realize GW-order heating power easily in the present large tokamak experiments and is expected to be a future attractive high-power heating method of CTs. Our TS-3/4 devices can produce and merge together various CTs with wide range of q-value. This paper addresses two important issues on the high-power heating characteristics: (1) how its heating and reconnection characteristics depend on the q-value of the merging CTs, (2) how this heating changes the CT equilibria, especially in terms of their beta (β) values. The fast merging of low-q CT realized the maximum heating power of 10MW in our initial experiment and increased β of the target CT by factor $\approx$ 2-3, revealing the high-β properties of CT equilibria.

2 Experimental Setup

Our TS-3/4 merging devices enable us to axially collide and to merge two CTs with wide range of q-value from 0.2 to 30. As shown in Fig. 2, the TS-3 merging device has two poloidal field (PF) coils and two sets of eight electrode pairs for two CT formations in a cylindrical vacuum vessel with length of 1m and diameter of 0.8m. These coils were used to inject arbitrary amount of toroidal and poloidal fluxes into the CTs. Right after their formation, the CTs have major and minor radii of 0.2m and 0.14m. Reversed currents
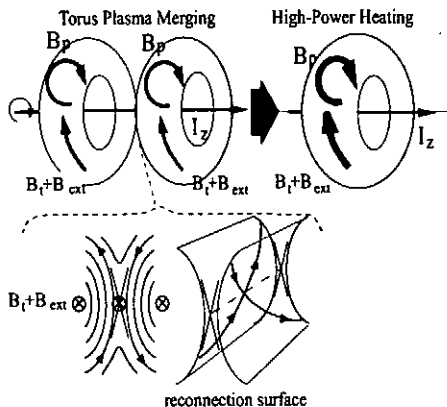
Fig. 1: Plasma heating scheme of compact toroids by use of merging (magnetic reconnection) effect.
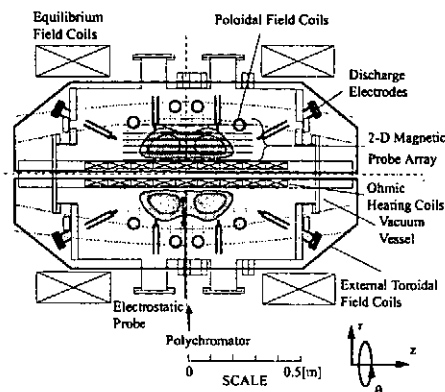

Fig. 2: The TS-3 merging device.

I_{acc} of the two PF coils were used to increase the plasma colliding force as well as the reconnection speed. The arbitrary toroidal field $B_{i,ext}$ was applied to the CTs, varying toroidal field B_t ($= B_{t,ext} + B_{t,in}$) of the CT continuously from low-q RFP region to high-q tokamak region. The 2-D array of magnetic probe was located on the r-z plane of the vessel to measure the poloidal and toroidal magnetic field profiles of the merging plasmas. Radial profile of ion temperature T_i was measured on the midplane by use of a Doppler broadening of H_β and C_{II} lines. An electrostatic probe was inserted at $z = 0$ to measure radial profiles of electron temperature T_e and density n_e.

3   Experimental Results

3.1   High Power Heating Effect of Merging

Figures 3 show poloidal flux with B_t contours and q profile of the CT plasmas with various center toroidal coil current I_{tfc} right after merging. For simplicity, the injected CT had the same flux as the target CT to maximize the heating effect. These data were obtained from the 2-D magnetic probe measurements on r-z plane. As I_{tfc} was increased from -5kA to 50kA, the q-value was observed to increase from the RFP regions ($q_0 \sim 0.1$), through the spheromak region to the tokamak region ($q_0 > 1$). In the present operation, the initial merging plasmas had the poloidal magnetic field $B_p \sim 0.05$T, ion and electron temperatures $T_i \approx T_e \sim 5$-10eV and density $n_e \sim 10^{20}$m^{-3}. Figures 4 show time evolutions of thermal energies of the merging CTs and a single CT, which were calculated from measurements of T_i, T_e and n_e. In all cases, the thermal energies of the merging CTs were observed to increase significantly as soon as they started merging. The maximum heating power of 10MW was obtained in the case of spheromak ($I_{tfc} = 0$). The thermal energies of the merged CTs were much larger than those of the single CTs in all cases. It is also noted that the heating energy increases with decreasing the q-value of the merging CTs. The heating energy was mainly contributed by an increment of ion temperature while electron temperature and density mainteined almost the same values.
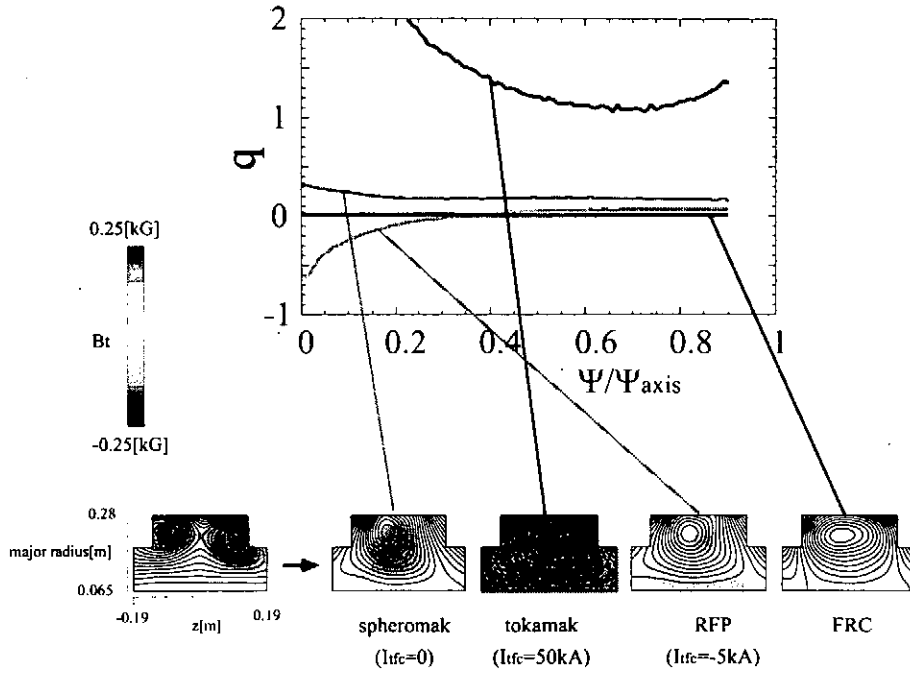
Fig. 3: Pololidal flux contours with B_t field strength and q profiles of ST, spheromak, RFP and FRC.
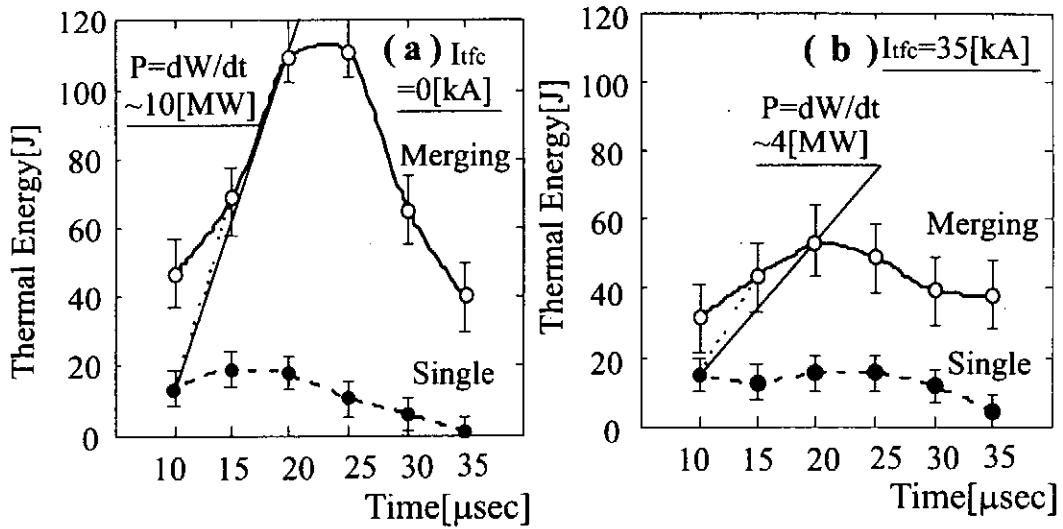

Fig. 4: Time evolutions of thermal energies of merging CTs (solid lines) and single CTs (dotted lines). The CTs are spheromaks (a) and STs ($I_{tfc} = 35kA$) (b).

3.2 High Beta Propertie of CTs

A question is how much of the injected heating energies are confined in those CTs with different q-values. As shown in Fig. 4, the thermal-energy of the high-q ST decays much slower than that of the spheromak with the lowest q. Figures 5 show the poloidal betas β_p, the central betas β_0 and the averaged betas β_N (normalized by the Troyon scaling value) of the CTs after merging and the single CTs, as a function of I_{tfc}. Right after the heating, these betas tend to decrease sharply to the constant values which are shown in Fig. 5. It was clearly observed that the merging process increases β_p and β_0 by factor 2-3. It is noted that the β_p increment increases with increasing I_{tfc} (q-value). These results indicate that the ST with higher q-value has better confinement to sustain the large heating energy of merging. Though most of the B_t profiles were located still on paramagnetic side of vacuum B_t profile, the high-power heating effect of merging was observed to reduce the paramagnetism of CTs. It is interesting to check whether this tendency agrees with the Troyon scaling or not. Figure 5(c) indicates that the present averaged β is always about four times larger than the Troyon limit. It is concluded that the high-β confinement of CT improves with increasing its q-value, while the ion heating energy of merging increases with decreasing the q-value.

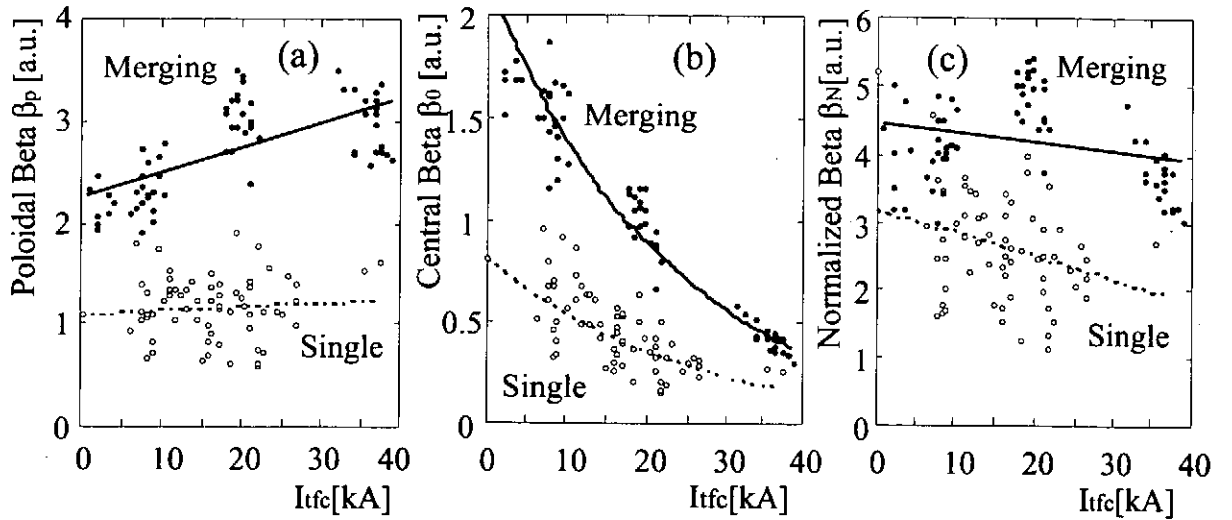Fig. 5: (a) Central poloidal betas β_p, (b) central betas β_0 and (c) averaged betas β_N (normalized by the Troyon scaling value) of merging CTs and single CTs, as a function of I_{tfc}.

4 Conclusions

In summary, our TS-3/4 CT merging experiments demonstrated the high-power heating characteristics of merging STs and spheromaks for the first time. The maximum heating power of 10MW was obtained in the initial low-field and small-scale experiment. The heating effect of merging is explained well by the anomalous ion heating effect of magnetic reconnection. The ion heating energy and merging speed increase with decreasing their q-value. However, the CT with higher q-value was observed to confine the injected thermal

energy longer. The β_p increment increases with increasing q-value.

References

[1] M. Katsurai et al., Plas. Phys. Cont. Nucl. Fus. Res. **2**, 415 (1994).

[2] Y. Ono et al., Phys. Fluids B **5**, 3691 (1993); Y. Ono et al., Plas. Phys. Cont. Nucl. Fus. Res. **2**, 263 (1996).

[3] Y. Ono et al., Plas. Phys. Cont. Nucl. Fus. Res. **2**, 619 (1992); Y. Ono, Trans. Fus. Tech. **27**, 369 (1995).

[4] Y. Ono et al., Phys. Rev. Lett. **76**, 3328 (1996); Y. Ono et al., Phys. Plasmas **4**, 1953 (1997).

[5] Y. Ueda et al., submitted to IEE Japan.

Flux Enhancement in Field-Reversed Configuration
with Rotating Magnetic Field

Masami Ohnishi, Jiro Kitagaki
Institute of Advanced Energy, Kyoto University
Uji, Kyoto 611, Japan

Waheed N. Hugrass
Department of Physics, University of New England
Armidale, New South Wales 2351, Australia

A Field-Reversed Configuration (FRC) is the candidate of environmentally clean D-^{3}He fusion reactor, since it can afford to confine a very high beta plasma. A Field Reversed Theta Pinch produces a hot and dense FRC plasma, which decays in a short period due to Joule dissipation. The flaw may be gotten rid of by applying a rotating magnetic field to a preexistent FRC to drive a steady current. The method has already shown numerically to be effective for keeping an FRC in steady state.

The work is extended to a case of the internal flux enhancement by the rotating magnetic field, of which frequency increases gradually in time. Maxwellian equations as well as Ohm's equation are simultaneously solved in the radial-azimuthal plane of the cylindrical coordinates. Based upon the computation, an evolution of an FRC is studied by the simple model including the effects of increasing the internal magnetic flux through a rotating magnetic field and controlling an axial magnetic field accordingly to the increased internal flux. We use the empirical energy confinement scaling obtained by LSX experiments. The dynamic behaviors of a plasma pressure, a separatrix radius and length are examined by solving the radial force balance and the energy balance under the assumption of preservation of a current radial profile during the evolution.

We obtain the conditions on the initial plasma parameters, an external axial magnetic field and a rotating magnetic field for the successful evolution. The initial FRC is essential to have a low density in order to cope with the large power loss during the evolution process. In conclusion, it is numerically shown that the evolution of an FRC to the plasma with much larger internal magnetic flux by applying externally the rotating magnetic field.

Recent Results From The Star Thrust Experiment (STX)

John Slough and Kenneth Miller
University of Washington Redmond Plasma Physics Laboratory
14700 NE 95th St, Suite 100
Redmond WA 98052
425-881-7706

INTRODUCTION

The Field Reversed Configuration (FRC) is a high β plasma with a closed magnetic field geometry which has great potential to be used as a space propulsive device and power source. However, present formation techniques are inefficient and massive, and cannot be extrapolated to reactor conditions since there is no method to sustain the configuration once formed. The STX experiment has recently begun experiments to study the formation and sustainment of the FRC using a rotating magnetic field. The success of this technique would vastly simplify and enable future FRC endeavors.

It is recognized that nuclear fusion could be an ideal source for space power and propulsion due to the high specific energy of its fuel, and the high specific impulse that is inherent in its exhaust products. However, most fusion confinement concepts are unsuited for space power production due to their large size and complexity, and are non-ideal for propulsion due to the use of D-T fuel which releases most of its energy in the form of high energy neutrons. A notable exception to these constraints is the FRC which is a simple elongated current ring confined in a modest field solenoidal magnet, as sketched in Figure 1.
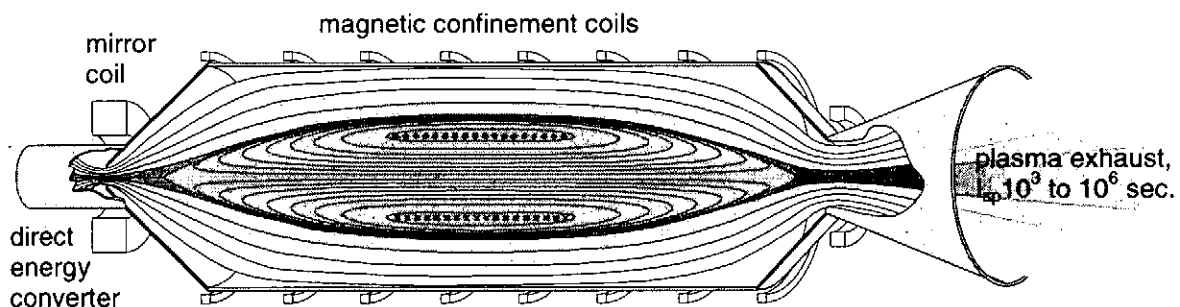

Figure 1. FRC as Power Source and Ion Engine for High Energy Space Missions.

The FRC lacks any significant toroidal field, which results in a compact high β plasma that is suitable for burning advanced aneutronic fuels. Synchrotron radiation would limit ignition of high temperature aneutronic fuels in the low β environment of most confinement geometries. The linear geometry and magnetic separatrix are a natural attribute for propulsive applications. Despite observed experimental robustness, the stability of FRCs is uncertain due to a lack of magnetic shear, but

kinetic effects have been demonstrated to stabilize FRCs up to at least modest sizes in the completed LSX experiments [1]. Further stability studies require a formation method that would allow the flux to be increased in the equilibrium FRC in order to produce the conditions relevant to a FRC reactor.

The near ideal reactor attributes of the FRC has led the DOE to fund an extension of the LSX program, TCS (Translation Confinement & Sustainment), designed to reach ever larger sizes for investigating confinement and stability limits. An important aspect of that program is the application of a rotating magnetic field (RMF) to both enlarge and sustain the plasma. The RMF is a uniform rotating field that is
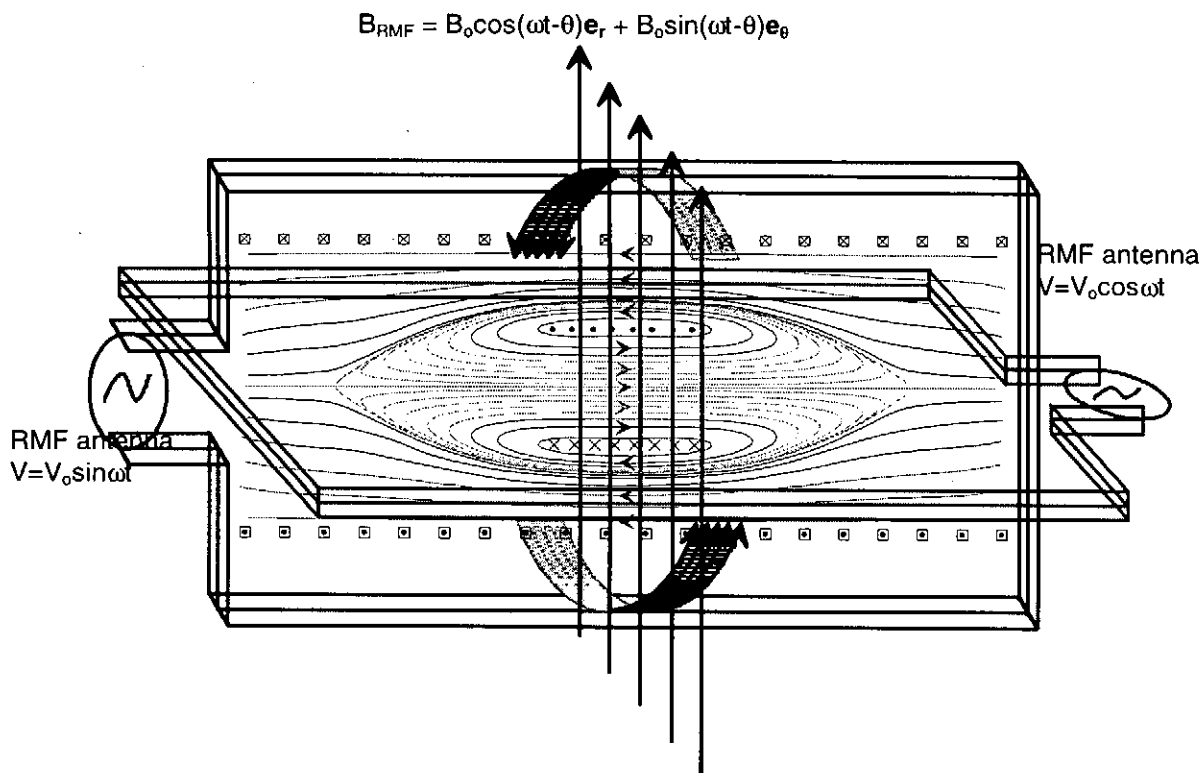
$$B_{RMF} = B_ocos(\omega t - \theta)e_r + B_osin(\omega t - \theta)e_\theta$$

Figure 2:   *Schematic of RMF antenna and resultant magnetic field.*

always transverse to the axis of symmetry, as shown on Figure 2. It has been demonstrated that the RMF can drive steady azimuthal currents in cold FRCs in the Australian Rotomak experiments [2]. These experiments however have never shown plasma confinement, since the open transverse RMF field componant was as large or larger than the confining axial field. The TCS experiment will employ the standard Field Reversed Theta Pinch (FRTP) technique for making large, hot FRCs. It is anticipated that the RMF field will then penetrate the FRC on a diffusion time scale and then sustain the configuration. STX however avoids the uncertainty of the penetration problem by initiating the FRC with the RMF already present.

RMF THEORY

The RMF drives a strong azimuthal current that reverses the direction of the external magnetic field and produces the FRC configuration (Figure 2). Unlike FRTP formation, where this current is driven by an induced azimuthal voltage caused by a

rapid reversal of the external field, the RMF current is driven in an inherently steady state manner which should allow for the subsequent sustainment of the configuration. A starting point for understanding the current drive process is the generalized Ohm's Law:

$$E = \eta j + j \times B/ne = \eta[j + (\omega_{ce}/\nu_{ei})j \times e_b].$$ (1)

If the Hall term $j \times B/ne$ is negligible, the electrons are unmagnetized, $E_\theta = \eta j_\theta$ is positive, and from Faraday's law, $d\phi/dt$ is negative. This means flux is leaving the FRC (less field reversal) and it is decaying. With the Hall term included, E_θ, for sufficiently small η or large $j_z B_r$, can be negative. The axial current is driven by an induced axial electric field, and the Hall term has the opposite sign of ηj_θ. When E_θ is negative, $d\phi/dt$ is positive, flux is entering the FRC, and it is growing (more field reversal). In the fluid picture, the RMF, when fully penetrated, creates an oscillatory $E_z = \omega r B_r$ which drives j_z such that $\langle j_z B_r \rangle$ reverse the ohmic ηj_θ. In the particle picture, the electrons appear to be tied to the RMF and rotate co-synchronously with it, while the ions remain at rest.

The first requirement on the RMF, as has been mentioned above, is that the electrons be magnetized while the ions are not.

$$\nu_{ei} << \omega_{ce} \qquad \omega_{ci} < \omega_{RMF} < \omega_{ce}$$ (2a,b)

This requirement is obvious from the extended form of Equation (1), where the Hall term is given in terms of ω_{ce}/ν_{ei}. $\omega_{ce} = eB_{RMF}/m_e$ and $\omega_{ci} = eB_{RMF}/m_i$ are the electron and ion gyro-frequencies with respect to the rotating field. Equation 2a is satisfied as one increases B_{RMF} and T_e while decreasing n ($\nu_{ei} \propto n/T_e^{3/2}$). However, according to Equation 2b, increasing B_{RMF} forces one to select a higher ω_{RMF}. Even if the ions are not magnetized, it is also necessary that the electrons do not transfer their momentum to the ions over a long time scale. Two-fluid calculations show this is easy to achieve with even minimal fueling rates since the fuel ions are deposited with zero angular momentum, and they diffuse out much faster then they gain momentum from collisions with the electrons [3].

The second requirement on the RMF is that it penetrates the plasma. The RMF effective skin depth should be on the order of the FRC's radius. The solution of Ohm's law, neglecting the Hall term, is characterized by the RMF penetrating a distance $\delta = (2\eta/\omega\mu_o)^{1/2}$, which is the resistive skin depth for a conductor in an RF field. The regime of interest, however, occurs for a hot low resistivity plasma, with $\nu_{ei} << \omega_{ce}$. In this regime, the Hall term dominates and the solution to Ohm's law yields $j_\theta \approx ner\omega$ and $j_z \approx E_z/(\eta\omega_{ce}^2/2\nu_{ei}^2)$, which states that the electrons are in synchronous rotation with the RMF and their axial oscillation is severely restricted. This suggests an effective resistivity of $\eta_{eff} = \eta\omega_{ce}^2/2\nu_{ei}^2$, and an effective skin depth of $\delta_{eff} = (\omega_{ce}/\nu_{ei})\delta$.

One can then define two dimensionless parameters that describe the RMF penetration condition.

$$\gamma_\omega = \omega_{ce}/\nu_{ei}, \qquad \lambda = R/\delta,$$ (3)

$$\gamma_\omega = \left(\frac{B_\omega}{en\eta} \right) \qquad\qquad \lambda = \left(\frac{\omega\mu_0}{2\eta} \right)^{1/2} R$$

Penetration can be maintained as long as $\gamma_\omega > \lambda$.

In order to penetrate, a somewhat larger field is required as can be seen in the numerical solution to the penetration of a conducting cylinder shown in Fig. 3. It is believed that the initial STX electron temperature $T_e \sim 2.5$ eV. The initial experiments were performed at an RMF frequency ω=2.2x10^6 rad/sec, at a peak RMF field B_ω=25 Gauss. The initial density from axial interferometry is ~ 5x10^{18} m^{-3}. These conditions imply a $\lambda \approx 10$, with a $\gamma_\omega = 6$ This value is not above critical and the current driven is less than that expected from fully synchronized electrons.
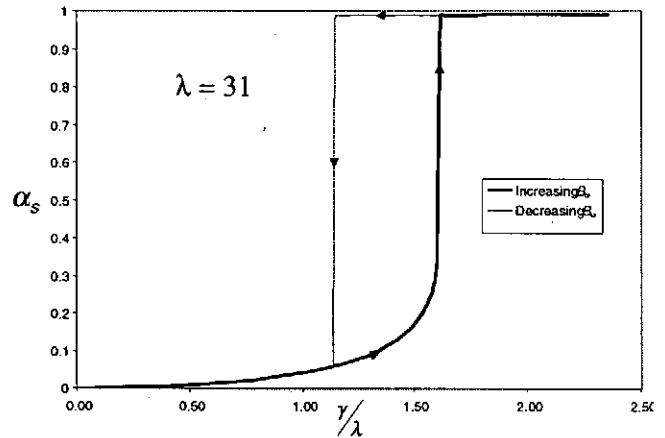

Figure 3: Ratio of the current driven to total maximum current, α_s as a function of the penetration parameters γ and ω.

STX APPARATUS

The STX vacuum wall consists of a 3-m long, 40-cm diameter quartz plasma tube that is surrounded by 4 turn solenoidal coils to provide an axial confinement field. Special "half" turn antennas, described below, produce the rotating magnetic field. A schematic of the device is shown below in Fig. 4.

0.4 m

3 m
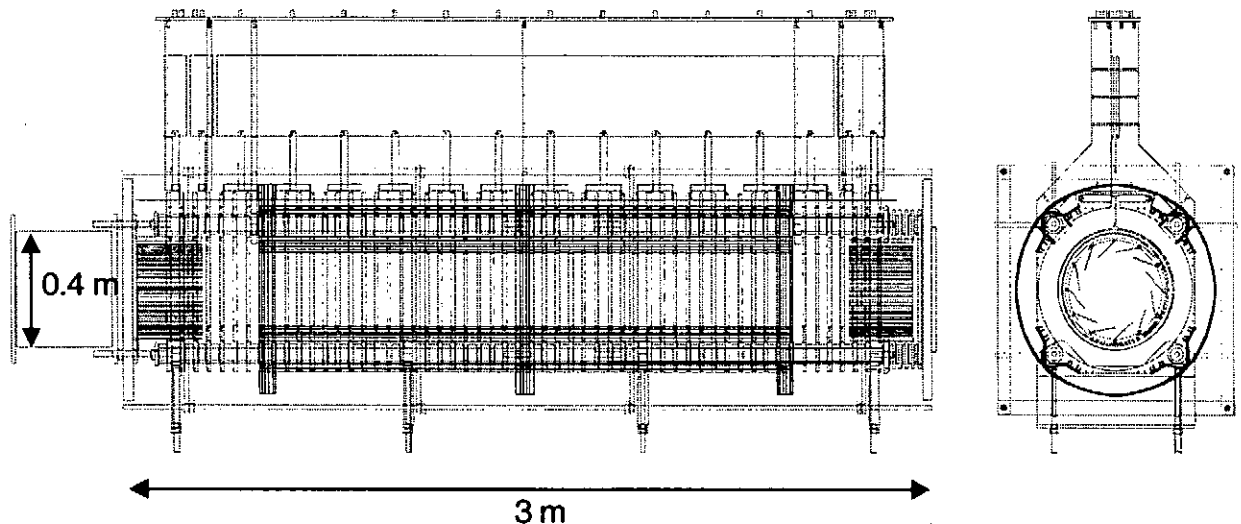
RMF Antennas

Two mutually perpendicular coils running the length of the experiment and driven 90 degrees out of phase generate the RMF. (Figure 2) To satisfy field uniformity constraints, each antenna coil is separated into 2 parallel coils, where the coil separation is set by a Helmholtz minimization to be R when the wires are at radius R from the axis of the machine. The antennas are placed outside the confinement

coils, at R = 0.36 m, for flexibility and ease of assembly. The large radius provides for great field uniformity inside the 0.2-m plasma tube radius.

RMF Power Supplies

In order to drive the RMF antennas, the 2 power supplies must be capable of delivering several megawatts for the duration of the experiment in order to rapidly ionize the plasma and heat it well past any radiation barrier.

The antenna power is provided by a resonant LC tank circuit driven by Isolated Gate Bipolar Transistor (IGBT) switches which are very high current on-off solid state devices. Each of two power supplies employ twelve IGBTs in parallel, with a primary current on the order of 12 kA. This current passes through the primary of a 20:1 air core transformer the secondary of which forms a parallel LC tank circuit (Q~100), where the inductor is the RMF antenna. The tank circuit transforms the square wave nature of the switch into a sinusoid. The IGBTs hold the voltage on the antenna constant, so that as the plasma load increases, more current is drawn from the switches. For tens of microseconds, the primary current output of 10 kA can be exceeded by a factor up to a factor of 3 without switch failure. The circulating current ramp-up from the vertical field antenna is shown in figure 5.
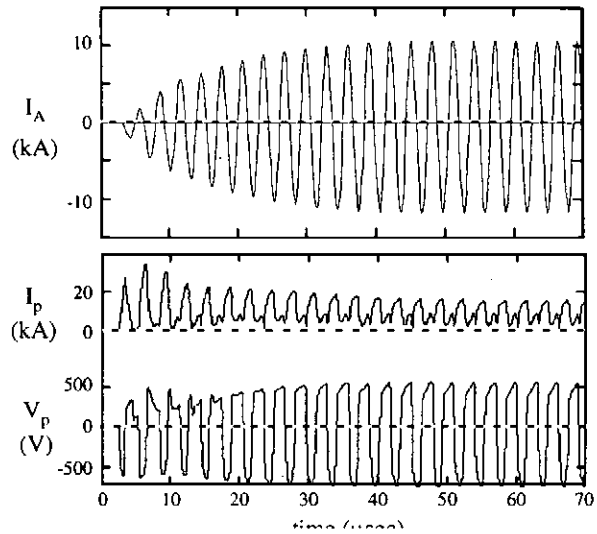
Figure 5: Experimental traces during the initial ramp-up of antenna current. From the top down, I_A is the total circulating current, I_p is the current flow in the transformer primary, and V_p is the voltage across the transformer primary.

Experimental Results

FRC's were generated using only the RMF antennas. The time history for excluded flux signals at various axial locations for two discharges are shown in
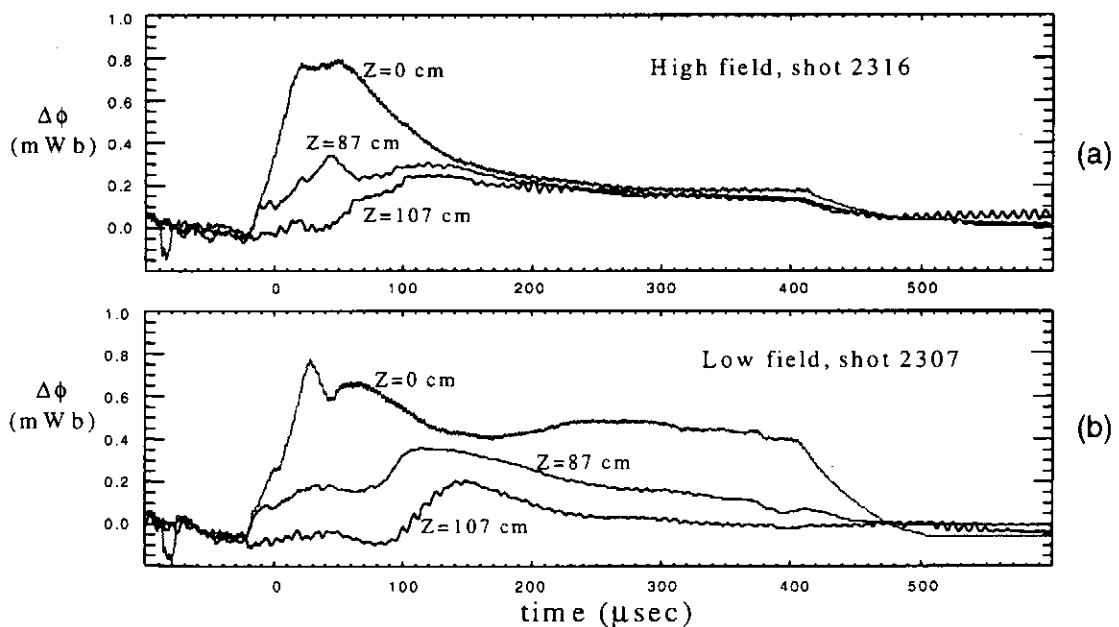
time (µsec)

Figure 6 above. The time history of the of the external magnetic field as well as the FRC excluded flux radius is shown in Figs. 7 and 8.

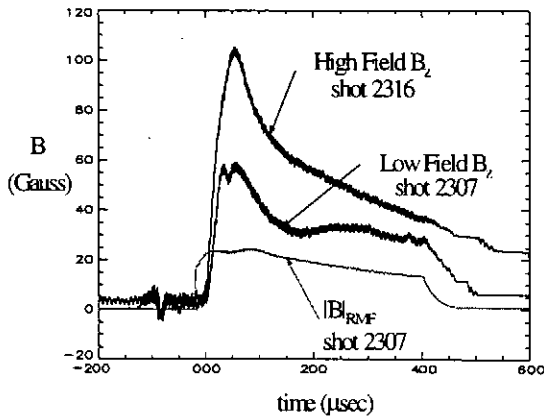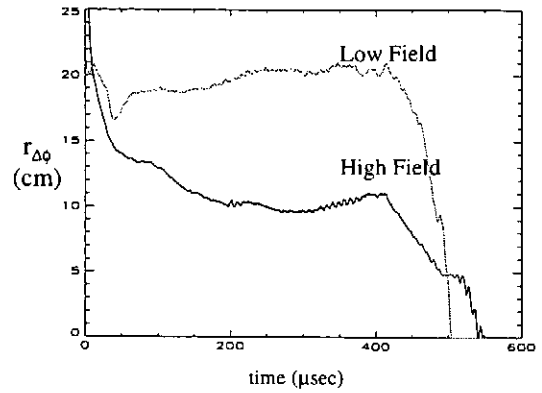Figure 7. Time hisory of external axial field and $|B_\omega|$.

Figure 8. Time history of the excluded flux radius.

It can be see that when the external field is kept low, just enough to keep the separatrix inside the vacuum wall, the FRC is maintained for the entire length of time that the RMF is applied. When the magnetic field is increased the current drive is seen to be lost. Using a slower magnetic field risetime (~0.3 msec) allowed for some understanding as to what may be happening as the axial B field is increased. For this case the axial interferometer yields a density time history at a radius of 12 cm as shown in Fig. 9. The filling pressure for this discharge was 0.4 mTorr D_2. This corresponds to a neutral D density of 2.67×10^{19} m^{-3}, so that the gas is only partially
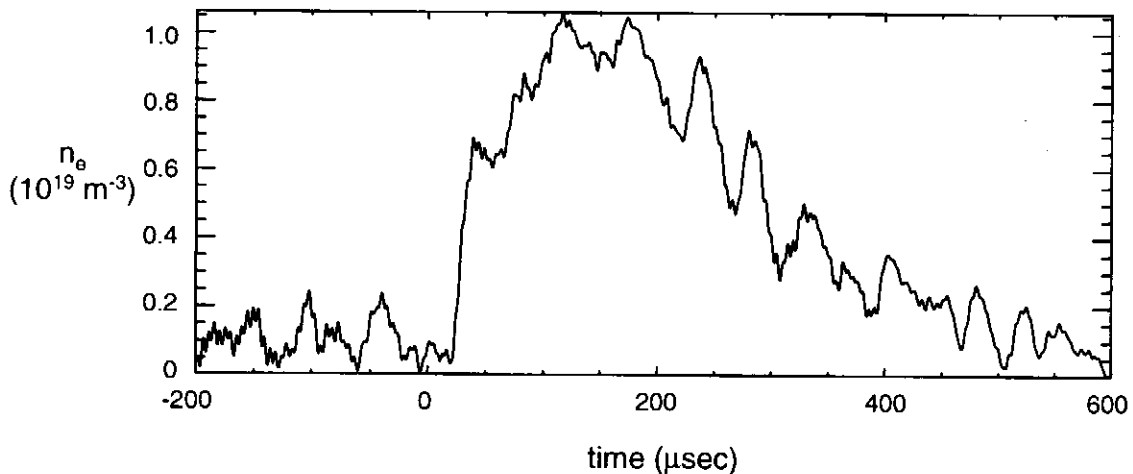

Figure 9. Electron density n_e at $r = 12$ cm. Density is inferred from a $1.06\mu m$ double-pass axial interferometer.

ionized at any time. The isolation of the FRC from the wall apparently allows for the ohmic heating of the driven FRC to increase in density. If the electron temperature is clamped by preionization losses, the parameter λ decreases until the condition for current drive is no longer satisfied (see Fig. 3). At this point the FRC decays and only a skin current is driven. This current is only sufficient to cause a reduction in the axial field, not reversal. This is manifested by a constant excluded flux signal along

the entire plasma column as in Fig. 6a after the first 100 µsec. The results from an internal radial array of B probes confirms this transition.

By measuring the increase in antenna resistance due to the plasma loading, one has a measure of the plasma resistivity. Ohmic heating power, P_Ω from a rigid rotor current profile, which is the result expected from the synchronous rotation of the electrons, yields

$$P_\Omega = \int \eta\, j^2\, dVol \cong 9\frac{\eta}{l_s} I_\theta^2 \qquad (4)$$

where l_s is the FRC length. The driven current can be related to the external field through Ampere's law:

$$B_e = \frac{\mu_0}{2 l_s} I_\theta \qquad (5)$$

The power delivered by the RMF antennas to the plasma is shown in Fig. 10. For
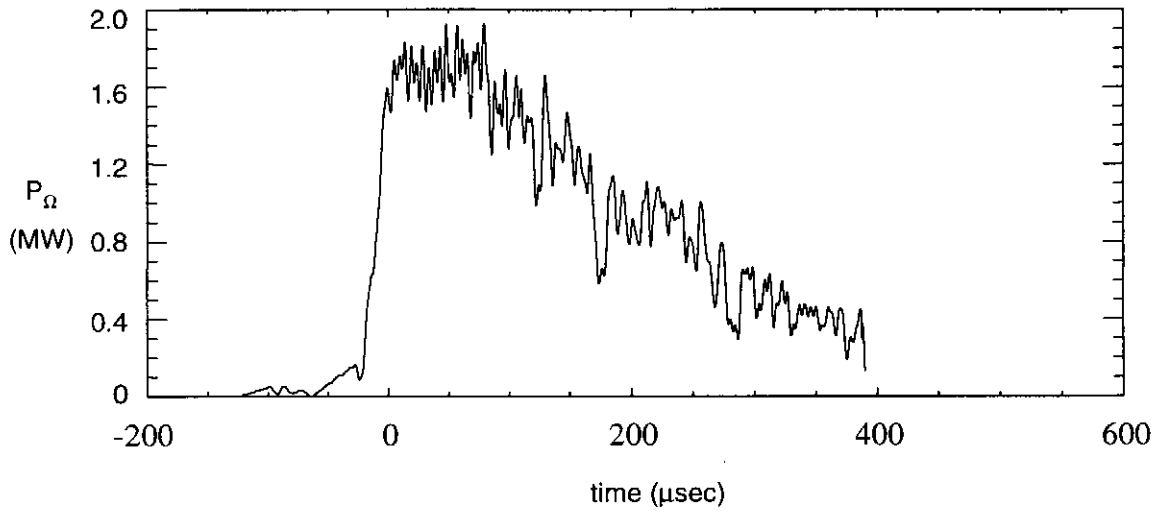

Figure 10. Increase in power loading of RMF antennas due to the presence of plasma.

low temperature plasmas the resistivity is typically classical. For this case, solving for the resistivity using equations 4 and 5, one has for the electron temperature.

$$T_e (eV) = 60 \left[\frac{l_s\,(m)\, B_e^2\,(kG)}{P_\Omega\,(MW)} \right]^{2/3}$$

During the period of field reversal, $P_\Omega \sim 1.6$ MW, $l_s \sim 2$ m, and $B_e \sim 0.08$ kG, which implies an effective electron temperature of 2.5 eV.

In order to achieve full penetration the ionization must be $\sim 100\%$. Only then will the electron temperature increase and maintain the ratio of γ to λ in a regime where the field will drive the full current. It is clear that the magnitude of the RMF field must be increased to accomplish this as well as a decrease in the starting neutral pressure. Future experiments will be focused in this direction.

References

[1] J.T. Slough, et al. "Transport, energy balance, and stability of a large field-reversed configuration", Phys. Plasmas **2**, 2286 (1995).

[2] A.J. Knight and I.R. Jones, "A Quantitative Investigation of Rotating Magnetic Field Current Drive in a Field Reversed Configuration", Plasma Physics and Controlled Fusion **32**, 575 (1990).

[3] M. Ohnishi and A. Ishida, "Effects of Radial Flow on Current Drive in Field Reversed Configurations by a Rotating Magnetic Field," Nucl. Fusion **36**, 232 (1996).

LOSS ESTIMATION OF TWDEC FOR A D-³He FRC FUSION REACTOR

M. Ishikawa[1], T. Kudo[2], T. Yamane[2], Y. Shimizu[2],
Y. Tomita[3], and H. Momota[3]

[1]*Institute of Engineering Mechanics, University of Tsukuba,*
Tsukuba 305-8573, Japan
[2]*Department of Electrical Engineering, Kyoto University,*
Yoshida-Honmachi, Sakyo-ku, Kyoto 606-8501, Japan
[3]*National Institute for Fusion Science, Oroshi-cho 322-6, Toki 509-5292, Japan*

Abstract

Loss mechanisms of TWDEC for a D-³He fueled FRC fusion reactor are studied with a numerical analysis. (1) The self-excitation of travelling wave has been attained by the one-dimensional analysis, which shows the conversion efficiency is about 70 to 73 %. (2) Axisymmetric two-dimensional analyses have shown that the loss related to the two-dimensional effect without collision with grids is about 5 %. (3) The loss related to the collision with grids is the most important, being about 11 %. (4) Effects of secondary electrons produced by the collision with grids is rather small and subrings can suppress effects of secondary electrons. (5) The loss related to leaked 3.6 MeV ⁴He is about 45 to 60 % of the total energy of leaked ⁴He. (6) The gross efficiency of TWDEC is estimated over 60 %.

1. Introduction

The energy supply of the whole world is estimated to be made by the oil 40.2%, the coal 28.9%, the natural gas 21.2%, the atomic energy 7.1%, and the hydro-power 3.1% (1994), showing that the fossil fuels such as oil, coal, and gas still provide about 90 % of the required energy[1]. It is reported that these resources are limited by 43 years for oil, 66 years for gas and 73 years for uranium, whereas only the coal can provide the energy for the long time span (235 years)[1]. On the other hand, the combustion of fossil fuels exhausts CO_2 into the atmosphere and the Intergovernmental Panel on Climate Change (IPCC) has estimated that the density of CO_2 would become twice of the level of prior-the-Industrial-Revolution around the mid of next century and the global mean surface temperature would increase by about 1° C in 2100 [2]. It is, therefore, very important to develop schemes to suppress the emission of CO_2 from power stations. One of them is to develop nuclear fusion power stations. The present paper treats an advanced concept which includes the advanced fuel and energy conversions.

The large part of produced energy in D-³He fusion plasma will be converted to the kinetic energy of charged particles, especially high energy proton ions. A conceptual design of the whole system of D-³He FRC fusion reactor was carried out to demonstrate the advantage of new concept [3]. As a part of the design, two kinds of direct energy conversion schemes have been proposed by H. Momota et al [4]. One of them is a cusp type direct energy converter (CUSPDEC), which will separate electrons and fusion proton ions and also convert the kinetic energy of electrons and low energy thermal ions into the electricity. A preliminary result of numerical analyses has been reported by Ishikawa and others [5]. Another scheme is the travelling wave direct energy converter (TWDEC), which will convert the kinetic energy of fusion proton ions into high frequency AC electric power. Some results of numerical study have reported by Ishikawa and others [5,6]. The present report describes a numerical study of loss mechanisms of TWDEC, of which basic parameters and generator configuration are taken from the conceptual design of the ARTEMIS-L reactor [3].

2. Brief Summary of Self Excitation of Travelling Wave

2.1 Basic Configuration of TWDEC

The basic configuration of TWDEC is a cylinder with a radius of 5 m and consists of a modulator and decelerators. The initial velocity of fusion proton ions is estimated with its kinetic energy of 15 MeV, while the total energy input into the TWDEC is 272.5 MW. After a preliminary optimization, the following parameters are decided:

Total length of TWDEC	=	30 m,
Wave length of modulator (λ)	=	2π m,
Number of modulator grids	=	5,
Number of decelerator grids	=	27,
Length of modulator	=	2π m,
Length of decelerator	=	$2.8 \times 2\pi$ m,
Frequency of travelling wave	=	8.54 MHz

2.2 Basic Equations Used for Self Excitation

The configuration of FRC fusion reactor is a long cylinder which consists of a formation chamber, a burning chamber, and direct energy converters (CUSPDEC and TWDEC) [3], and therefore the cylindrical coordinates (r-θ-z) are used in the present analysis.

The possibility of the self-excitation of travelling wave is shown by one-dimensional analyses (in the z direction). The basic equations used in the one-dimensional analysis are the momentum conservation equation of fusion proton ions:

$$\frac{\partial^2 V}{\partial z^2} = -\frac{\rho}{\epsilon_0}, \qquad (1)$$

Poisson's equation for the electric field including the space charge effect:

$$\frac{d^2 z}{dt^2} = -\frac{e}{m}\frac{\partial V}{\partial z}, \qquad (2)$$

$$m = \frac{m_{p0}}{\sqrt{1 - v^2/c^2}},$$

and electric circuit equations of external control circuit, shown in the section 2.3. In these equations e is the electric charge unit, m_{p0} the rest mass of proton, t the time, v the velocity of proton and V the electric potential; ρ the space charge density, and ϵ_0 the permittivity in the vacuum.

The momentum equation is analytically solved within each numerical mesh. Poisson's equation is solved with the Galerkin Finite Element Method (GFEM). The potential at the grids obtained with electric circuit equations becomes the boundary condition at the grids for Poisson's equation.

2.3 External Electric Circuit

Figure 1 illustrates the schematic diagram of the external electric circuit, where the displacement current at the grids is evaluated with the electric charge which is induced by the proton ion flow. The values of inductance L and capacitance c are decided by
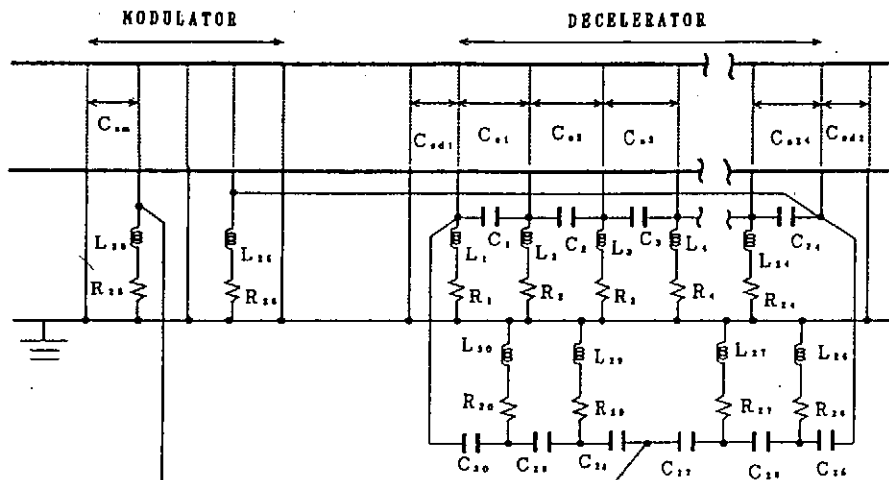

Fig.1 Schematic diagram of external electric circuit.

$$\omega^2 LC = 1 \qquad (3)$$

where ω is the angular frequency of travelling wave. After some try-and-errors it has been found that the Q-values of each unit external circuit must have the same value. The electric circuit equations are solved with the fourth order Runge-Kutta method.

2.4 Self-Excitation of Travelling Wave and Conversion Efficiency

It has been demonstrated that the designed circuit can yield the autonomous oscillation (self-excitation) of the travelling wave within the framework of one-dimensional approximation.

Figure 2 shows the process of self-excitation, where the potential value of 25th grid is depicted and Ts is the period of induced travelling wave. It takes about 800 periods of the wave, indicating that the self-excitation is rather a slow physics process but also very fast (within 0.1 ms) from the engineering view point.
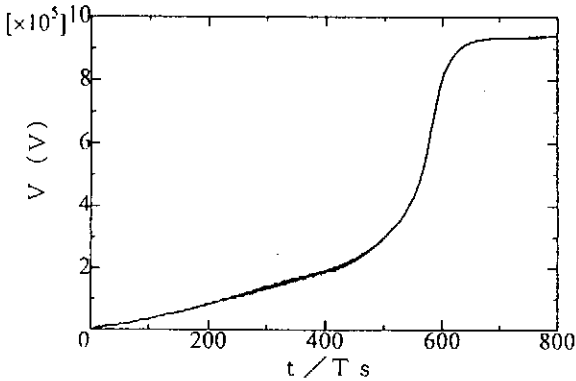

Fig.2 Self-excitation process of travelling wave.

A preliminary optimization of the grid potential and the grid position has been carried out, showing that the maximum value of grid potential of 1.0 MV and the distance of 3.5 λ between the last grid of modulator and the first grid of decelerator result in the maximum conversion efficiency of 70.9 %. According to this result, the configuration of TWDEC is fixed for the two-dimensional calculation.

Then, Fourier analyses have been carried out to find the reason why the distance of 3.5 λ between the last grid of modulator and the first grid of decelerator gives the maximum conversion efficiency, leading to further optimization [5]. It

has been shown that the maximum efficiency increases to 72.3 % at 3.8 λ of the first grid of decelerator.

3. Loss Mechanisms

3.1 Two-Dimensional Effects

Axisymmetric two-dimensional analyses on the r-z plane are carried out in order to estimate efficiency reduction due to two-dimensional effects. The external electric circuits are not included in the two-dimensional analyses, while values of grid potential are given independently, which form the travelling wave with designed frequency and the effect of magnetic field is included.

The basis equations are also the momentum equation of proton ions:

$$m\frac{d^2 r}{dt^2} = -\frac{\partial u}{\partial r} \qquad (4)$$

$$m\frac{d^2 z}{dt^2} = -\frac{\partial u}{\partial z} \qquad (5)$$

$$m\frac{d\theta}{dt} = \frac{1}{r}\left(\frac{p_\theta}{r} - eA_\theta\right) \qquad (6)$$

$$u = u^0 + eV \qquad (7)$$

$$u^0 = \frac{1}{2m}\left(\frac{p_\theta}{r} - eA_\theta\right)^2, \qquad (8)$$

and Poisson's equation:

$$\frac{\partial^2 V}{\partial r^2} + \frac{1}{r}\frac{\partial V}{\partial r} + \frac{\partial^2 V}{\partial z^2} = -\frac{\rho}{\epsilon_0}. \qquad (9)$$

where A_θ is the θ-component of vector potential, p_θ the θ-component of angular momentum and u the generalized potential.

The r-z plane is divided by triangles and the momentum equation is solved analytically within the triangles. The θ-component of momentum of proton ions is also estimated.

Poisson's equation is solved with the Galerkin FEM with the first order triangular elements. Given values of grid potential play a role of the boundary condition.

We have proposed a cylindrical grid which is made of five co-axial, cooling-water circular pipes of one cm diameter, as shown in Fig.3. The ratio of open space for protons is 99.2 % for each grid.

It is found that the two-dimensional effects are small in the first half of channel but increase much in the last quarter as the energy of protons is converted into the electric energy, as shown in Fig.4, where the collision with grids is included.

The maximum efficiency of 65.5 % has been obtained with the grid voltage of 1.7 MV when the

collision loss with the grids is neglected. The reduction of efficiency due to the two-dimensional effects is about 5 %. The potential decreases between the grids in the radial (r) direction, and, therefore, the effective potential reduces compared with the one-dimensional case, resulting in higher grid voltage required in the two-dimensional analyses.
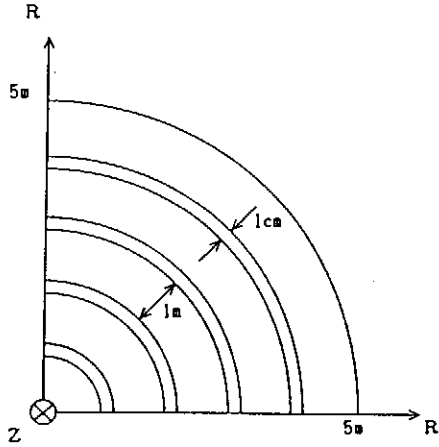

Fig.3 Schematic diagram of cylindrical grids.
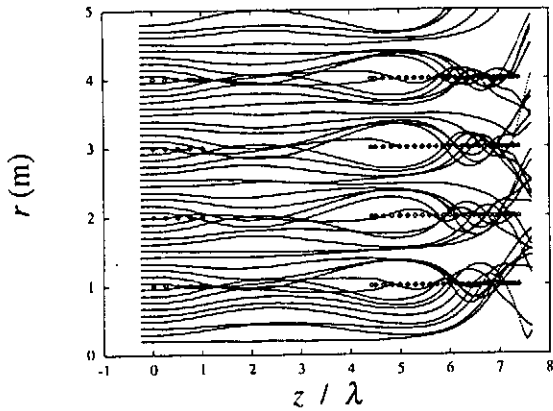
3.2 Collision Loss with Grids

Fig.4 Trajectory of protons projected on r-z plane.

It is found that the maximum efficiency becomes 54.7 % with the grid voltage of 1.4 MV when the collision loss is included. The reduction of conversion efficiency due to the collision with grids is about 11 %, which is rather large. It should be noticed, however, that the proposed system includes total 32 grids and thus the simplest estimation of the conversion efficiency is $0.709 \cdot (0.992)^{32} = 0.548$. The two-dimensional

result of efficiency of 54.7 % is, therefore, very good, although the two-dimensional effects look like rather large from the view point of ion trajectory (Fig.4) and potential distribution.

The optimum grid voltage decreases compared with the case of no collision loss, simply because the higher voltage enhances the two-dimensional effect and increases the collision of proton ions with the grids.

3.3 Secondary Electrons

3.3.1 Behavior of secondary electrons

When the protons collide with the grids, the secondary electrons are produced, depending on materials and proton energy. The copper is selected for the grids as an example in the present study and the produced electron number is taken from published data [7, 8, 9]. The data used for the present study is depicted in Fig.5, where the yield is rather small in the range of high energy, which has a large effect on the place of secondary electron emission.
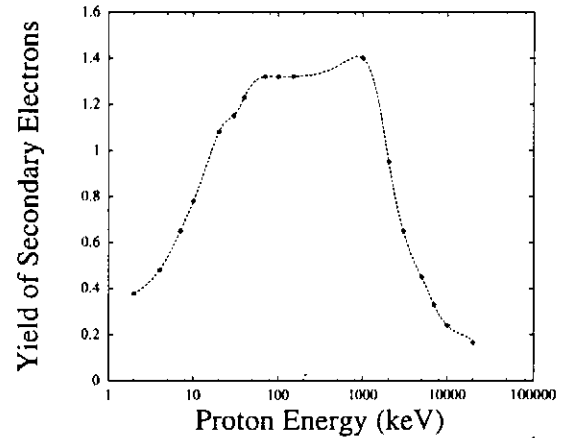

Fig.5 Relation of secondary electron emission yield and proton energy.

The guiding-center approximation is used for the electrons, since the Larmor radius of electrons is very small under the present condition. The momentum equation of electrons are added to Eqs.(4) to (9). The z-component of momentum equation is given by:

$$m_e \frac{d^2 z}{dt^2} = -eE_z \qquad (10)$$

$$m_e = \frac{m_{e0}}{\sqrt{1 - v^2/c^2}} \qquad (11)$$

where m_{e0} is the rest mass of electron and E_z the z component of electric field.

The θ component of electron velocity is given by:

$$v_\theta = \frac{E_r}{B_z} \qquad (12)$$

where B_z is the z component of magnetic flux density and E_r the r component of electric field. The electrons do not move in the r direction, because the electrons move along the magnetic field line within the framework of guiding-center approximation.

The electrons are accelerated into the relativistic velocity because of the strong electric field in the TWDEC, whereas the relativistic effect can be neglected for protons although the effect is always taken into account. During the computation the acceleration is very strong and thus the inertial mass of electron is updated about 1000 times within one numerical time step.
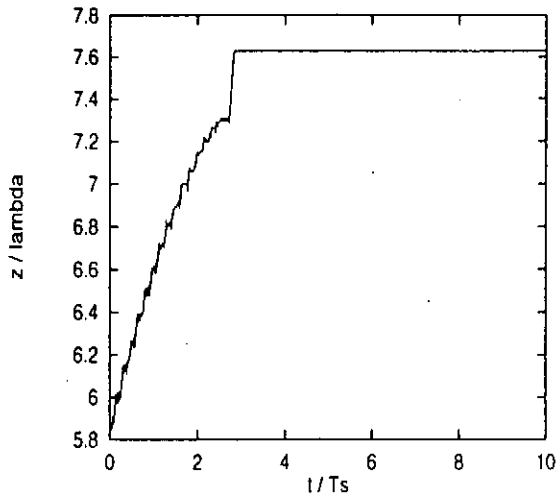

Fig.6 Trajectory of an induced secondary electron.

Figure 6 depicts the behavior of an induced secondary electron, which depends on the place and timing of emission. The secondary electrons are accelerated by the electric field of travelling wave, move back and forth with the travelling wave, and finally reach the exit.

The loss due to the secondary electrons is estimated by two ways. The first one is based on the interaction of the electrons and the electric field, whereas the second one is based on the conversion efficiency of TWDEC itself. The first loss estimation is done by adding over all electrons the following integration, which is the work of an electron with the electric field.

$$W = -\int eE_z dz \qquad (13)$$

Figure 7 depicts the variation of loss ratio obtained by Eq.(13), showing that the average loss is

about 1 % of the input kinetic energy of protons. The energy is bounced between the electrons and the electric field of travelling wave. The instantaneous loss reaches 8 %, but the average value is rather small.
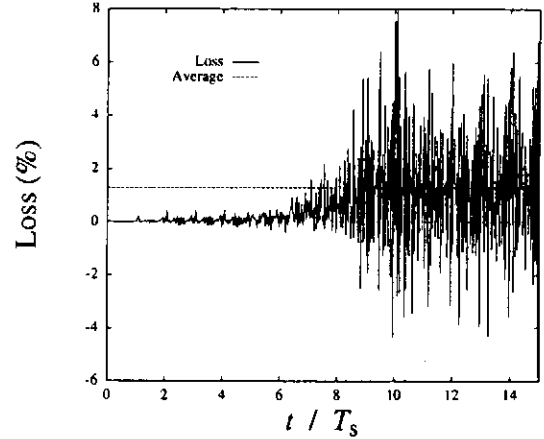

Fig.7 Variation of loss ratio due to secondary electrons (first estimation).

Figure 8 compares the variations of conversion efficiency of TWDEC, indicating that the effects of secondary electrons are rather small and the efficiency with electrons becomes slightly higher than that of no electron case. This is because the electrons decrease slightly the out-of-phase protons with higher energy.

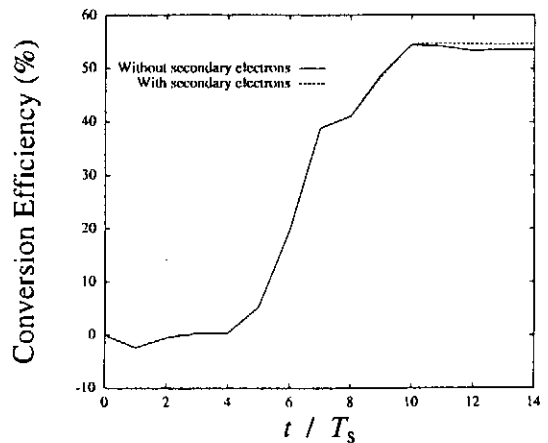

Fig.8 Comparison of conversion efficiency (effects of secondary electrons; second estimation).

3.3.2 Subrings to suppress secondary electrons

Figure 9 depicts the distribution of estimated number of the protons colliding at grids along the

generator. The number of collision protons fluctuates along the generator, but the tendency does not change much.
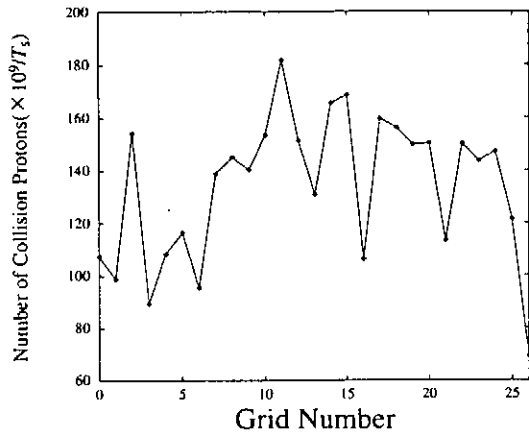

Fig.9 Distribution of collision protons.

Figure 10 shows the distribution of estimated number of the secondary electrons at grids along the generator. The number of secondary electrons increases along the generator, because the kinetic energy of protons decreases as converted into the electric energy along the generator, depending on the characteristics of emission of secondary electrons depicted in Fig.5.
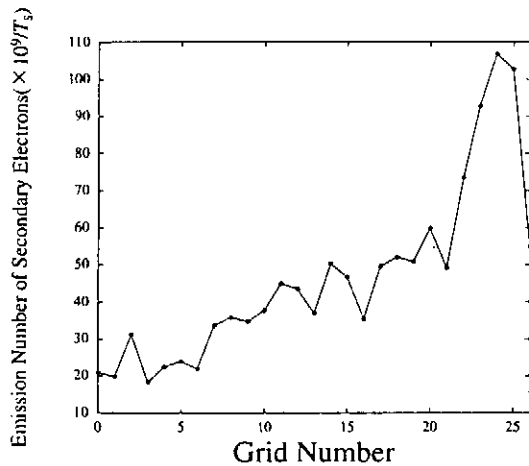

Fig.10 Distribution of produced secondary electrons.

Then we propose subrings which can suppress the secondary electrons to affect the performance of TWDEC. The subrings are implemented to each pipe of the cylindrical grids and a potential relative to the grid is maintained by cells. A numerical analysis has been carried out to estimate the required radius, pitch and electric potential

difference of subrings. The pipe of cylindrical grids is approximated as a linear column and an axisymmetric two-dimensional electric potential distribution is obtained with GFEM.
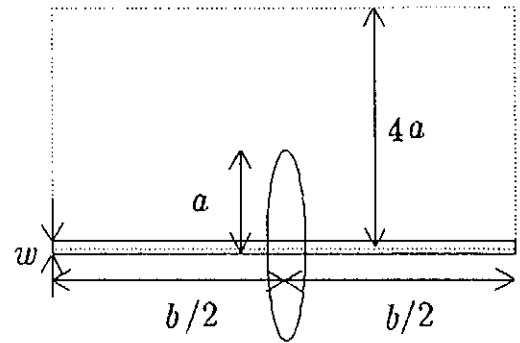

Fig.11 Schematic diagram of axisymmetric subring (a is the radius of subring, b the pitch and w the diameter of cylindrical pipe).

Figure 11 depicts the schematic diagram of an axisymmetric subring, where a is the radius of subring, b the pitch and w the diameter of cylindrical pipe. The area with length of b and radius of $4a$ is treated.
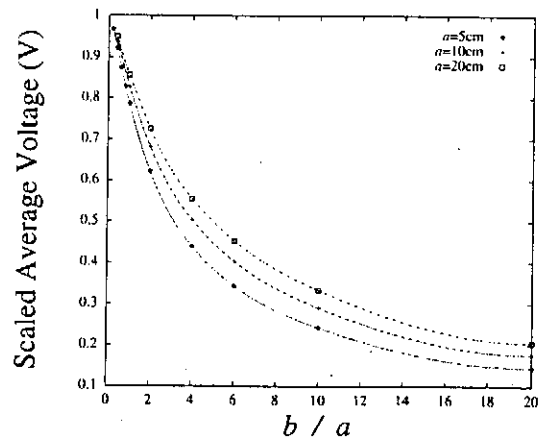
Fig.12 Effect of dimensions.

Figure 12 shows the relation of the scaled average voltage with the radius a and length b. It is seen that the radius of subring has rather a small effect and the ratio a/b must be larger than 5.

Figure 13 depicts the integrated energy distribution of secondary electrons, which shows the ratio of electrons covering up to the indicated energy. Figures 12 and 13 can indicate the needed voltage of cells. If the subrings of 5 cm radius are implemented with a pitch of 25 cm and the cells of 30 V are installed at each subring, the effects of secondary electrons up to about 7.6 eV can be

suppressed, which is about 65 % of all secondary electrons, where the average energy of emitted electrons is assumed to be 2.4 eV.

Fig. 13 Integrated energy distribution of secondary electrons.

Therefore, suppressor subrings can be implemented, which can suppress easily over 60 % of the secondary electrons, if required.

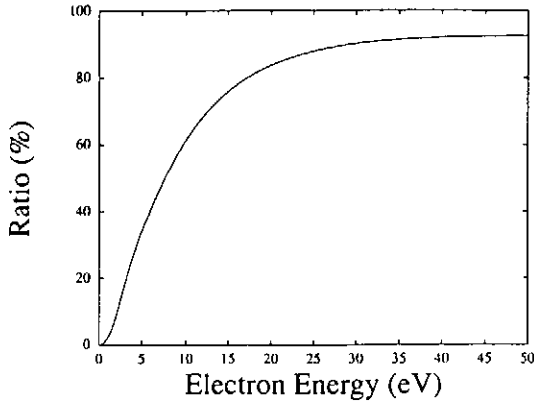The numerical results show that the average energy of protons which collide with the grids of decelerator decreases gradually along the generator, as the kinetic energy of protons is converted into the electric energy due to the interaction with travelling wave, whereas the maximum energy does not change much along the generator because the out-of-phase protons with high energy always exist.
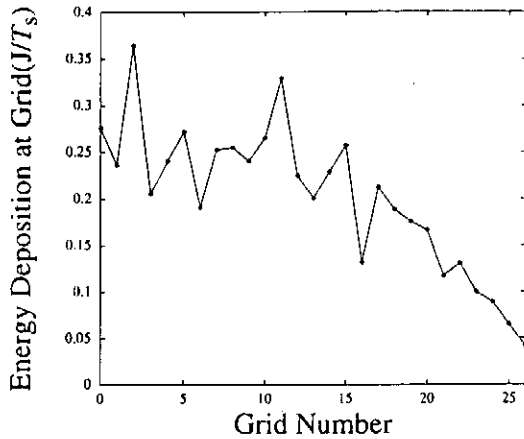
Fig. 14 Energy distribution deposited by protons at grids.

Figure 14 depicts the distribution of total energy deposited at the grid by protons which collide with the grids of decelerator. The deposit

energy at the grid also decreases gradually along the generator. The maximum energy of protons does not have a large effect, because the number of protons with higher energy is small.

3.4 Leakage of High Energy ^{4}He

The D-^{3}He reaction will also produce the 3.6 MeV ^{4}He's, and if they leak into the TWDEC from the fusion plasma, there must be some effects on the performance of TWDEC. It is assumed that the total energy of leaked 3.6 MeV ^{4}He ranges from 0.1 % and 10 % of the total kinetic energy of protons.

Fig. 15 Velocity distribution of leaked ^{4}He.

Fig. 16 Conversion efficiency of leaked ^{4}He.

Figure 15 shows the relative velocity distribution of leaked ^{4}He along the generator, where the total energy is assumed to be 10 % of the total energy of protons. The leaked ^{4}He also can be bunched at the modulator but becomes out-of-phase toward the entrance of decelerator, and

is scattered rather uniformly over a wide energy range in the decelerator, resulting in gaining energy as a whole.

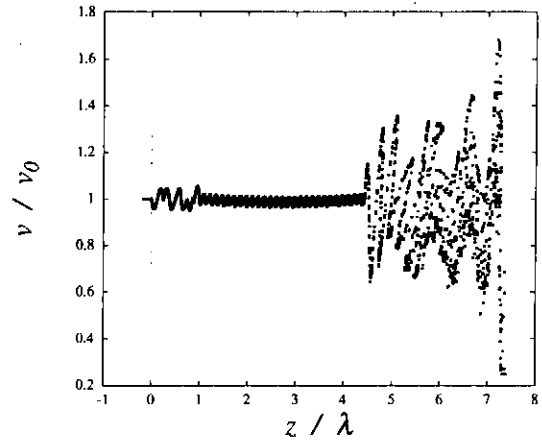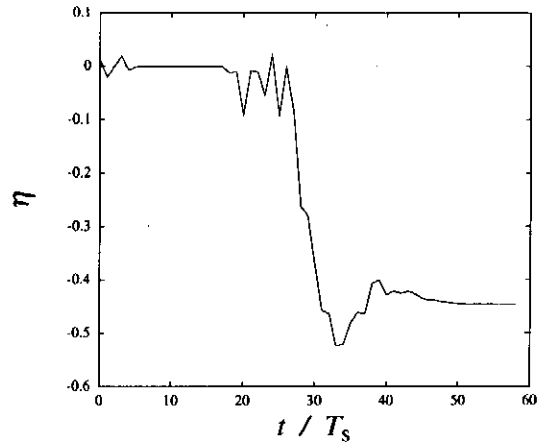Figure 16 depicts the variation of the conversion efficiency of leaked ^{4}He, showing that the leaked ^{4}He obtains about 45 % of initial energy from the electric field, corresponding to Fig. 15. The computation has shown that the loss becomes larger (about 60 %) when the total energy of leaked ^{4}He decreases.

It is, thus, shown that the reduction of produced AC power is about 60 % to 45 % of kinetic energy of leaked 3.6 MeV ^{4}He. The leakage of 3.6 MeV ^{4}He should, therefore, be maintained as small as possible.

4. Electric Power Station

When the fusion reactor is considered as an electric power station, three kinds of electric power are produced: (1) AC power from a conventional thermal cycle, (2) low voltage DC power from the CUSPDEC, and (3) high voltage, high frequency AC power from the TWDEC. Thermal energy of the cooling water of the TWDEC can, thus, be transferred to the thermal cycle where more than 30 % of conversion efficiency into the electricity can be realized as the conventional steam Rankine cycle.

The overall gross efficiency of the TWDEC can be estimated as 54.7 + 45.3 x 0.3 = 68.3 %, which is very high compared with the conventional D-T reactors.

The frequency of AC power produced with the TWDEC is too high and therefore must be converted into DC power with some devices which must be studied in a near future. It should be noticed that the estimated voltage is adequate for DC transmission lines and the produced power can be easily transferred to existing large AC networks through DC transmission lines.

5. Concluding Remarks

The loss mechanisms of TWDEC for a D-^{3}He fueled FRC fusion reactor have been studied with the numerical analysis.

(1) The self-excitation of travelling wave has been attained by the one-dimensional analysis, which shows the conversion efficiency is about 70 to 73 %.

(2) The axisymmetric two-dimensional analyses have shown that the loss related to the two-dimensional effect without collision with grids is about 5 %.

(3) The loss related to the collision of protons with grids is the most important, being about 11 %.

(4) Effects of the secondary electrons produced by the collision of protons with grids is rather small and the subrings which can suppress the effects of secondary electrons can be implemented rather easily.

(5) The loss related to the leaked 3.6 MeV ^{4}He is about 45 to 60 % of the total energy of leaked ^{4}He. The leakage of 3.6 MeV ^{4}He should be suppressed as small as possible.

(6) The gross efficiency of TWDEC is estimated to be over 60 %.

References

[1] Handbook of Energy and Economic Statistics in Japan, The Energy Conversation Center, Japan (1996).

[2] J. T. Houghton et al. (editor), "Summary for Policymakers", Climate Change 1995, Cambridge University Press (1996).

[3] H. Momota et al., "D-^{3}He Fueled FRC Reactor 'ARTEMIS-L'", Proc. 14th Int. Conf. Plasma Physics and Controlled Nuclear Fusion Research, IAEA-CN-56/G-13 (1992).

[4] H. Momota, "Direct Energy Conversion of 15 MeV Fusion Protons", LA-11808-C, Los Alamos National Laboratory, pp.8-13 (1990).

[5] M. Ishikawa, T. Kudo, T. Yamane, Y. Tomita and H. Momota, "Numerical Study of Direct Energy Converters for a Deuterium-Helium FRC Fusion Reactor", Proc. IAEA/TC Meeting "Innovative Approaches to Fusion Energy" (1997).

[6] M. Ishikawa, T. Kudo, T. Yamane, S. Hayashi, Y. Tomita and H. Momota, "Simulation of Direct Energy Converters for a D-^{3}He FRC Fusion Reactor", Proc. US-Japan Workshop "Physics Base of D-He3 Fusion", pp.105-108 (1998).

[7] E. W. Thomas, "Secondary Electron Emission", Nuclear Fusion, pp.94-104 (1984).

[8] D. Hasselkamp, "Kinetic Electron Emission from Solid Surfaces under Ion Bombardment", Particle Induced Electron Emission, Springer-Verlag (1992).

[9] E. W. Thomas, "Particle Induced Electron Emission", Atomic and Plasma-Material Interaction Data for Fusion, International Atomic Energy Agency, Vol.1, pp.79-91 (1991).

3D HYBRID AND MHD/PARTICLE SIMULATIONS OF FIELD-REVERSED CONFIGURATIONS

E. V. Belova, W. Park

Princeton Plasma Physics Laboratory, Princeton, NJ 08543, USA

Abstract

A nonlinear 3D code in cylindrical geometry is being developed for the stability studies of FRC. Two numerical schemes have been implemented: a hybrid scheme with particle ions and fluid electrons, and an MHD/particle scheme in which the background plasma is described by MHD equations, and energetic ions are treated via particle simulations. The MHD equations are advanced on a finite-difference mesh in a cylindrical coordinate system, while particle pushing is done on a 3D Cartesian grid. Full ion dynamics is retained in order to include large-orbit effects (with $s \sim 1$), which are important for the tilt mode stabilization in FRC. Also, in contrast to the previous work, δf method is utilized to reduce numerical noise in the simulations. The code has been benchmarked against previous MHD simulation of tilting instability in FRC [1,2]. It was found that rigid rotation reduces the growth rate, but does not stabilize the mode even for rotation rates equal to the Alfvén time. Sheared rotation is found to be destabilizing for the velocity profile considered. Simulations with a fast ion beam with 1% of the bulk ion density and $\bar{s} \sim 3$ did not show a reduction in growth rate of the tilting instability.

Introduction

Numerous analytical and numerical calculations were conducted to study the internal tilt mode in a field-reversed configuration (FRC) [1-6]. Non-ideal MHD effects, including the finite ion Larmor radius effect, energetic ion beam effect, and ion kinetic effects were considered to explain the discrepancy between the FRC stability on MHD time scale [7] observed in the experiments and the theoretically predicted instability to the $n = 1$ tilt mode with the growth rate $\gamma = CV_A/Z_S$. Here, V_A is a characteristic Alfvén velocity, Z_S is the separatrix half-length, and C is a coefficient of the order of unity.

The plasma rotation and the inclusion of the Hall term were found to reduce the growth rate; however, a change in a linear mode structure prevented the complete stabilization [1], which was predicted earlier based on the dispersion analysis employing an MHD type displacement as a trial function.

A Vlasov-fluid dispersion functional [3] was used to describe the ion kinetic effects, and a greatly decreased growth of the tilting mode compared to the MHD prediction

was found by computing the eigenfrequencies for an MHD type trial function and $\bar{s} \sim 2$. Here, $\bar{s} = \int_{R_0}^{R_s} r \, dr/(R_s \rho_i)$, R_0 and R_s are the magnetic null and the separatrix radius, respectively, and ρ_i is the local ion Larmor radius. However, contradictory results regarding the kinetic stabilization were obtained in 3D particle simulations [5,6], where it was found that the tilt mode growth rate is only slightly affected by $\bar{s}$ value, and strongly depends on the value of the plasma beta at the magnetic separatrix β_s. The latter result was explained as a stabilizing influence of the gyrating ions crossing the separatrix repeatedly ('anchoring ions') and thus connecting the internal and external regions [6].

The effect of energetic ion beams on tilting instability was studied in [4] using MHD/particle simulations, and it was found to stabilize the tilt mode for beam energy of about 40% of the total energy and beam density larger than 1.5% of the bulk density.

In this paper, the new 3D hybrid MHD/particle code developed for the stability study of FRC is described. In contrast to the previous work [5,6], δf method is used to reduce numerical noise in the simulations. Equations of the δf scheme are presented and the solution of the equilibrium problem with kinetic ions is discussed. Results of MHD simulations including sheared rotation, and initial results of the simulation with energetic ion beams are described.

Simulation model

Two numerical schemes have been implemented: a hybrid scheme with particle ions and fluid electrons, and an MHD/particle scheme in which the background plasma is described by MHD equations and energetic ions are treated via particle simulations.

The particle ion motion is described by Lorentz force equations with the standard leapfrog scheme used for the time advance.

In the hybrid kinetic ions/fluid electrons scheme the electric field is calculated from the electron momentum equation neglecting the inertial term

$$\mathbf{E} = -\mathbf{u}_e \times \mathbf{B} - \frac{\nabla p_e}{e n_e} + \eta \mathbf{J}, \tag{1}$$

where $\mathbf{u}_e = -(\mathbf{J} - \mathbf{J}_i)/(e n_e)$ is the electron fluid velocity.

In the MHD/kinetic ion model the energetic ion density is assumed to be small compared to the bulk density, $n_i \ll n_b$, and the current coupling scheme [8] is used:

$$\rho_b \frac{d\mathbf{v}_b}{dt} = -\nabla p_b + (\mathbf{J} - \mathbf{J}_i) \times \mathbf{B}/c - e n_i(\mathbf{E} - \eta \mathbf{J}), \tag{2}$$

$$\mathbf{E} = -\mathbf{v}_b \times \mathbf{B} + \eta \mathbf{J}, \tag{3}$$

where ρ_b, v_b and p_b are bulk density, velocity and pressure; J_i is energetic ion current and quasineutrality is assumed.

A 2D self-consistent equilibrium is found by solving the Grad-Shafranov equation including equilibrium flows, and it is used as an initial condition for 3D stability calculations. MHD equilibrium with sheared flow is obtained assuming constant temperature, $T = p/\rho$, in which case the pressure profile can be written as:

$$p(\psi, r) = p_0 g(\psi) \exp\left(\frac{m_i r^2 \omega^2}{2T}\right), \qquad (4)$$

where $\omega = \omega(\psi)$ is the angular velocity, and the Grad-Shafranov equation becomes

$$r\frac{\partial}{\partial r}\left(\frac{1}{r}\frac{\partial \psi}{\partial r}\right) + \frac{\partial^2 \psi}{\partial z^2} = -r^2\left[p_0\frac{\partial g}{\partial \psi} + p_0 g\frac{m_i r^2}{T}\omega\frac{\partial \omega}{\partial \psi}\right]\exp\left(\frac{m_i r^2 \omega^2}{2T}\right). \qquad (5)$$

An equilibrium with kinetic ions is found by solving the equation

$$r\frac{\partial}{\partial r}\left(\frac{1}{r}\frac{\partial \psi}{\partial r}\right) + \frac{\partial^2 \psi}{\partial z^2} = -r^2\frac{\partial p_b}{\partial \psi} + J_{\phi i}, \qquad (6)$$

were $J_{\phi i}$ is the azimuthal component of the ion current.

MHD simulations

The MHD simulations were performed for the pressure profile inside the separatrix given by [2]:

$$p(\psi) = p_0(K_0 + x - \frac{d}{2}x^2), \qquad x = \frac{\psi}{\psi_0}, \qquad (7)$$

where ψ_0 is the value of the flux at the magnetic null point, K_0 a numerical parameter proportional to the value of the plasma beta at separatrix, and d is the profile hollowness parameter. Simulations were carried out for $\beta_s = 0.1$, $d = -0.5$, elongation $2 \leq E \leq 4$, and different velocity profiles.

Rigid rotor rotation is found to be stabilizing, with normalized growth rate reduced to $\gamma Z_s/V_A = 0.96$ and 0.74 for Mach number $M = 0.5$ and $M = 1.$, respectively, in agreement with previous calculations [1]. Here, the Mach number is defined as $M = V_0/V_A$, where V_0 is velocity at the magnetic null.

Fig. 1 shows contours of constant ψ and pressure for a calculation with velocity profile $\omega(\psi) = \omega_0(\psi/\psi_0)^2$ inside the separatrix and no rotation outside, with rotation rate $M = 0.5$. The calculated growth rate for this profile, $\gamma Z_s/V_A \approx 2$, is larger than the growth rate for an equilibrium without rotation. The destabilizing effect of the sheared rotation in this case can be due to a free energy associated with the
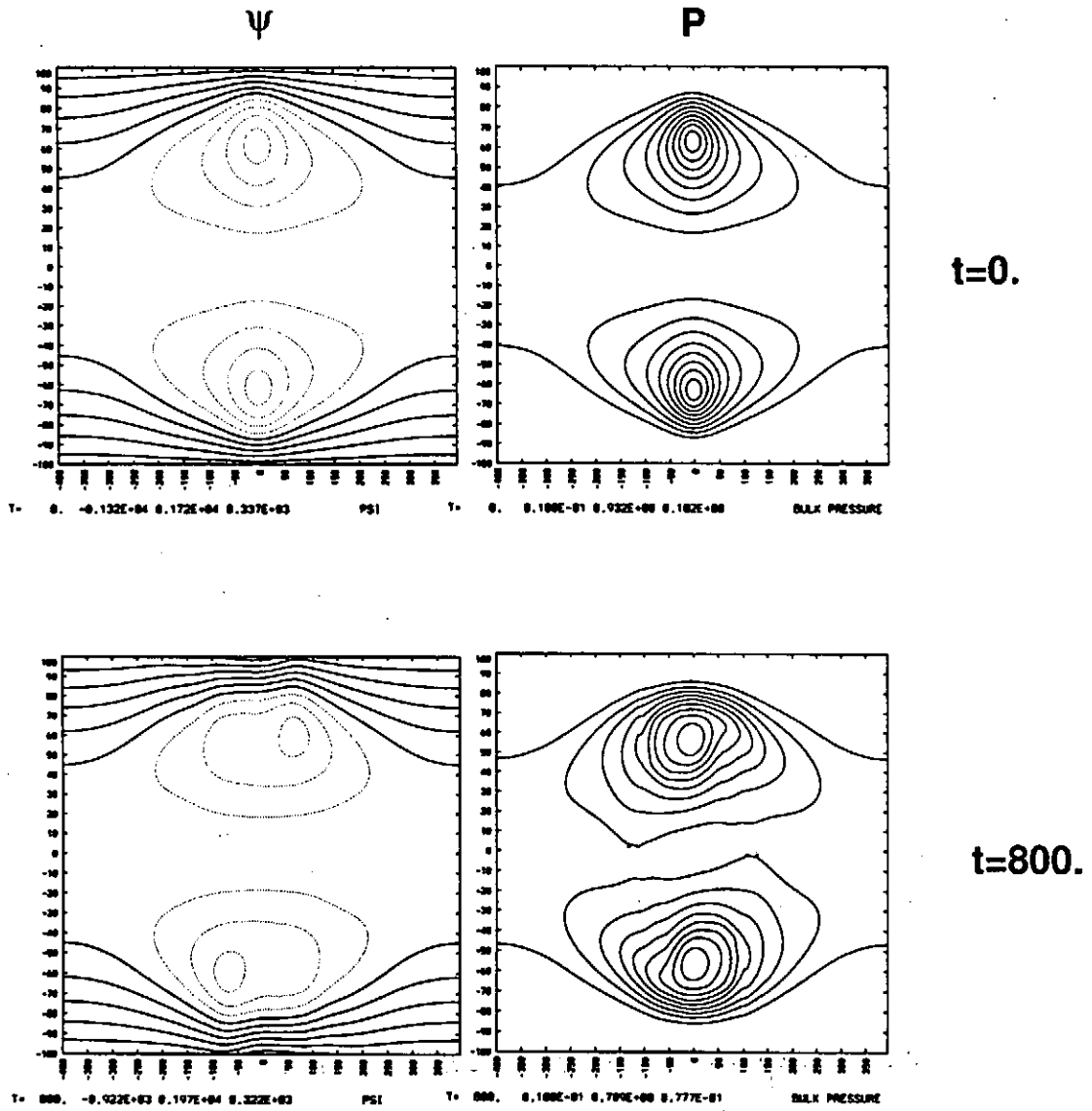
ψ   P

t=0.

t=800.

Figure 1: Contour plots Ψ and pressure from a tilt calculation using equilibrium with sheared rotation.

sheared rotation (velocity shear instability similar to Kelvin-Helmholtz instability), or a current profile effect, because the strong rotation at the magnetic null changes the equilibrium profile to a more peaked one, which is also found to be a destabilizing effect [2].

Since the mechanisms leading to FRC rotation are believed to be the loss of particles with a preferential angular momentum and end shorting of the open field lines, the outer field lines are likely to rotate with larger angular velocity than the internal field lines. The simulations were carried out for the velocity profile $\omega(\psi) = \omega_0(0.7 - \psi/(3\psi_0))$, with $M \approx 0.2$ and with a rotational velocity difference of $0.4V_A$ between the magnetic null and the separatrix. No reduction of the growth rate due to rotational shear has been found for these rotation rates.

δf scheme and kinetic equilibrium for FRC

The equilibrium ion distribution function F_0 is a function of the integrals of motion, which in the case of an azimuthally symmetric equilibrium, are the energy, $\varepsilon = m_i v^2/2$, and the azimuthal angular momentum, $p_\phi = m_i r v_\phi - e\psi$, where $\psi = -rA_\phi$ and it is assumed that there is no zero order electric field. In δf scheme the zero order moments of the distribution function are calculated analytically, and the particle simulations are applied to the calculation of the perturbed ion density and current. The weight $w = \delta F/P$ is assigned to each simulation particle, and satisfies the equation:

$$\frac{dw}{dt} = -\left(\frac{F}{P} - w\right) \frac{dF_0}{dt} \frac{1}{F_0}, \tag{8}$$

where F is the ion distribution function, and P is the distribution function of simulation (marker) particles.

For $F_0 = F_0(\varepsilon, p_\phi)$ the time advancing of the particle weights requires calculation of time derivatives of ε and p_ϕ:

$$\dot{\varepsilon} = e\mathbf{v} \cdot (\mathbf{E} - \eta\mathbf{J}) \tag{9}$$

$$\dot{p}_\phi = er[(E_\phi - \eta J_\phi) + \mathbf{v} \times \mathbf{B} \cdot \hat{\phi}] - e\frac{d\psi}{dt}, \tag{10}$$

where the last equation can also be written as

$$\dot{p}_\phi = -er(\eta J_\phi) + e\sum_\alpha v_\alpha \frac{\partial A_\alpha}{\partial \phi}, \tag{11}$$

where $\partial\mathbf{A}/\partial t = -\mathbf{E}$.

As a particular choice of the equilibrium distribution function one can take the exponential rigid-rotor distribution function:

$$F_0 = F_0(\varepsilon - \omega p_\phi) \tag{12}$$

$$= n_0 (m_i/2\pi T_i)^{3/2} \exp(-\varepsilon/T_i + \omega p_\phi/T_i), \tag{13}$$

where ω is the constant angular rotation frequency, T_i is the uniform ion temperature. It can be shown that this distribution function corresponds to a local Maxwellian distribution with the ion density given by

$$n_i(\mathbf{x}) = n_0 \exp \left(\frac{m_i r^2 \omega^2}{2T_i} - \frac{e\psi\omega}{T_i} \right) \tag{14}$$

and the mean ion velocity $V_\phi = r\omega$.

Another choice of distribution function

$$F_0 = n_0 (m_i/2\pi T_i)^{3/2} \exp(-\varepsilon/T_i)(K + C_1 p_\phi + C_2 p_\phi^2) \tag{15}$$

results in the equilibrium similar to the MHD equilibrium with pressure profile given by (7). This can be shown by calculating the moments of F_0:

$$n_i(\psi, r) = n_0[(K + C_2 m_i r^2 T) - C_1 e\psi + C_2 e^2 \psi^2] \tag{16}$$

$$J_{\phi i}(\psi, r) = e n_0 T (C_1 - 2C_2 e\psi) r \tag{17}$$

$$P_{zz} = P_{rr} = p(\psi, r) = n_i(\psi, r) T \tag{18}$$

$$P_{\phi\phi} = p(\psi, r) + 2C_2 n_0 m_i T^2 r^2 \tag{19}$$

where $\mathbf{P}$ is the ion stress tensor. Since the functional dependance $J_{\phi i}(\psi, r)$ is the same as in the MHD solution, for parameters C_1 and C_2 such that

$$J_{\phi i}(\psi, r) = -r p_0/\psi_0 (1 - d\,\psi/\psi_0), \quad \psi < 0 \tag{20}$$

the MHD equilibrium is reproduced. It must be noted that the ion pressure in this case is not a scalar, therefore, ion distribution can not be represented by the local Maxwellian distribution as it was done in [5,6]. Using the Maxwellian distribution for particle loading will result in F_0 which is not a solution of Vlasov equation.

The hybrid MHD/kinetic ions scheme was used to study the effect of energetic ions on the tilt instability. The 2D equilibrium solution using the exponential rigid-rotor distribution function (13) was calculated for $\omega R_0 = 1.8 V_A$ and large thermal velocity $v_{th} = 3V_A$ and energetic to bulk ion density ratio equal 0.03. A very peaked profile was obtained with most of the energetic ions consentrated near magnetic null point. 3D simulations with energetic ion density equal to 1% of bulk density (up to 25% of bulk pressure) and $\bar{s}$ values 2 and 5 show very little difference from the MHD growth rate.

References

1. R. D. Milroy et al., Phys. Fluids B **1**, 1225 (1989).
2. J. W. Cobb et al., Phys. Fluids B **5**, 3227, (1993).
3. D. C. Barnes et al., Phys. Fluids **29**, 2616, (1986).
4. D. C. Barnes and R. D. Milroy, Phys. Fluids B **3**, 2609, (1991).
5. R. Horiuchi and T. Sato, Phys. Fluids B **2**, 2652, (1990).
6. K. Nishimura, R. Horiuchi and T. Sato, Phys. Plasmas, **4**, 4035, (1997)
7. M. Tuszewski, Nucl. Fusion **28**, 2033, (1988).
8. W. Park et al., Phys. Fluids B **4**, 2033, (1992).

Spheromak as a Minimum Dissipation Non Force-Free State

B. Dasgupta[1], M. S. Janaki[1] and P. Dasgupta[2]

[1]Saha Institute of Nuclear Physics

I/AF, Bidhanagar, Calcutta 700 064, India

[2]Dept. of Physics, Kalyani University, West Bengal, India

Abstract

The principle of minimum dissipation together with the constraint of global magnetic helicity leads to the Euler-Lagrange equation $\nabla \times \nabla \times \nabla \times \mathbf{B} = \Lambda \mathbf{B}$ for a closed system containing magnetized plasma. The spheromak configuration emerges as a solution of this equation on using analytically continued Chandrasekhar Kendall eigenfunctions in the complex domain and assuming conducting boundary conditions $B \cdot \mathbf{n} = 0$ and $\mathbf{j} \times \mathbf{n} = 0$ at the boundary. The solutions differ significantly from the minimum energy state of Taylor as exhibited by a finite pressure gradient in the axisymmetric state. The value of β has been calculated in the $z = 0$ plane and is found to be about 40 %. For values of Λ, higher than the value corresponding to minimum dissipation state, double humped spatial behaviour of $\mathbf{j} \cdot \mathbf{B}/B^2$ and hollow pressure profiles are exhibited. These results show a good agreement with those obtained by solving nonlinear Grad-Shafranov equation containing pressure.

1   Introduction

Spheromak is a design for plasma confinement, where the magnetic field is self-organized to form a set of closed nested surface in a region of space. The Spheromak configuration corresponds to the classical "Hill's Vortex" of fluid dynamics. The toroidal and poloidal fields of a Spheromak are of equal strength approximately and are generated primarily by internal currents rather than external coils.

Important theoretical and experimental results for the spheromak problem came

from the application of Taylor's relaxation model that conjectured the magnetic fields in a spheromak plasma to relax towards a state of minimum energy subject to constant helicity. In a closed system, the minimum magnetic energy equilibrium satisfies the force free equation $\nabla \times \mathbf{B} = \lambda \mathbf{B}$ with λ=constant. Rosenbluth and Busaac[1] obtained the spheromak field configuration from the Chandrasekhar Kendal(CK) solution of the force-free equation and thus attempted to confirm that spheromak is a Taylor force-free state.

An ideal Taylor state is unsuitable for plasma confinement as it predicts a flat pressure profile. In reality, any plasma confining device must have a non-flat pressure profiles. For spheromak, such pressure profiles have been observed experimentally and departure from minimum state was also noticed[2-5].

Montgomery & Phillips[6] utilized the principle of minimum dissipation rate for the first time in an MHD problem to predict the relaxed states of a driven dissipative system. We try to establish here that a spheromak equilibrium is a non force-free relaxed state, and supports a significant fraction of perpendicular component of current as well as a pressure gradient by modelling the equilibrium as a state of minimum dissipation rate.

2   Euler Lagrange Equation

In presence of dissipation, a relaxed state with minimum dissipation under the constraint of conserved total helicity can be obtained. If only ohmic dissipation is considered, the dissipation rate for a magnetofluid is given by $R = \eta \int \mathbf{j}^2 d\tau$. The total magnetic helicity is defined as $K = \int \mathbf{A} \cdot \mathbf{B} d\tau$. The minimization procedure yields the following Euler-Lagrange equation

$$\nabla \times \nabla \times \nabla \times \mathbf{B} = \Lambda \mathbf{B} \tag{1}$$

where Λ is a Lagrange's undetermined multiplier.

3   Solutions of $\nabla \times \nabla \times \nabla \times \mathbf{B} = \Lambda \mathbf{B}$

We now propose to solve eq. (3) in terms of the Chandrasekhar-Kendall eigenfunctions [7] that are solutions of the force-free equation $\nabla \times \mathbf{B_0} = \lambda \mathbf{B_0}$. The magnetic field being a solenoidal field can be decomposed into its toroidal and poloidal ingredients:

$$\mathbf{B}_0 = \mathbf{B}_{0T} + \mathbf{B}_{0P}$$

$$\mathbf{B}_{0T} = \nabla \times (\xi \Phi_0), \quad \mathbf{B}_{0P} = \nabla \times \nabla \times (\xi \Psi_0) \tag{2}$$

Here ξ is a position vector. $\mathbf{B}_0$ satisfies the Taylor equation provided

$$(\nabla^2 + \lambda^2)\Phi_0 = 0, \quad \Psi_0 = \Phi_0/\lambda$$

In spherical polar coordinates (r, θ, ϕ)

$$\xi = \mathbf{r}, \quad \Psi_0(r,\theta) = \frac{\alpha_0}{\lambda} j_m(\lambda r) P_m^n(\cos\theta) e^{in\phi} \tag{3}$$

The classical spheromak equilibrium solution is given by $n = 0, m = 1$ state. The poloidal flux function for the force-free state, $\chi_0(r,\theta)$ is given by $\chi_0 = -r\sin\theta d\Psi_0/d\theta$ Lines of constant poloidal field for the force free fields are given by the $\chi_0 = $ constant lines. The solutions of $\nabla \times \mathbf{B}_0 = \mathbf{B}_0$ given by eq. (2) are now analytically continued [8] to complex values of λ in order to obtain solution of eq. (1).

$$\mathbf{B} = \nabla \times (\vec{\xi}\Phi) + \nabla \times \nabla \times (\vec{\xi}\Psi) \tag{4}$$

$$\text{with} \quad \Phi = \sum_{i=0}^{2} \alpha_i \Phi_i, \quad \Psi = \frac{1}{\lambda} \sum_{i=0}^{2} \alpha_i \omega^{2i} \Phi_i \tag{5}$$

where Φ_i are the solutions of $(\nabla^2 + \lambda^2 \omega^{2i})\Phi_i = 0$.

$$\Phi_i = j_m(\lambda \omega^i r) P_m^n(\cos\theta) e^{in\phi} \tag{6}$$

The expression for $\mathbf{B}$ given by eq. (4) satisfies eq. (1) for $\Lambda = \lambda^3$. The flux function correponding to eq. (1) for the $m = 1, n = 0$ state is obtained as

$$\chi(r,\theta) = \frac{r}{\lambda} \sum_{i=0}^{2} \alpha_i \omega^{2i} j_1(\lambda \omega^i r) \sin^2\theta$$

The constants α_i occuring in eq. (5) are fixed by assuming conducting boundary conditions

$$\mathbf{B} \cdot \mathbf{n} = 0, \quad \mathbf{J} \times \mathbf{n} = 0 \quad \text{at} \quad r = a \tag{7}$$

where a is the radius of the sphere. The constants are given by

$$\frac{\alpha_1}{\alpha_0} = -\frac{\omega^2(B_{1\theta}B_{2\phi}^* - B_{2\theta}^*B_{1\phi})\mid_{r=a}}{(B_{2\theta}B_{2\phi}^* - B_{2\theta}^*B_{2\phi})\mid_{r=a}} \tag{8}$$

$$\alpha_2 = \alpha_1^* \tag{9}$$

$\mathbf{B}_0, \mathbf{B}_1, \mathbf{B}_2$ are the magnetic fields corresponding to Ψ_0, Ψ_1 and Ψ_2 respectively. In order to obtain non-trivial values for the constants α_i, the fields at the boundary have to satisfy the following condition

$$B_{1r}Im(B_{2\theta}B_{2\phi}^*) - B_{1\theta}Im(\omega^2 B_{2r}B_{2\phi}^*) + B_{1\phi}Im(B_{2r}B_{2\theta}^*) = 0 \tag{10}$$

For a given vaue of n and m, the value of λa can be obtained from The eigensolution with lowest energy dissipation rate for the $n = 0, m = 1$ state has the eigenvalue $\lambda a = 3.99547$.

The magnetic field components for the $n = 0, m = 1$ state are given by

$$B_r = \frac{2}{\lambda r} \sum_{i=0}^{2} \alpha_i \omega^{2i} j_1(\lambda \omega^i r) \cos\theta \tag{11}$$

$$B_\theta = -\sum_{i=0}^{2} \alpha_i \left(\frac{\omega^{2i}}{\lambda r} j_1(\lambda \omega^i r) + j_1'(\lambda \omega^i r) \right) \sin\theta \tag{12}$$

$$B_\phi = \sum_{i=0}^{2} \alpha_i j_1(\lambda \omega^i r) \sin\theta \tag{13}$$

The $\mathbf{B}_P$ lines, given by χ=constant are sketched in Fig. 1 for $\lambda a = 3.99$.
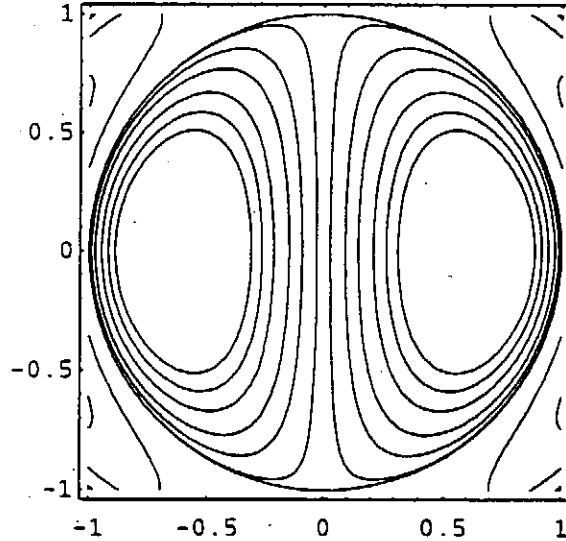

Fig. 1 A spheromak

In the $z = 0$ plane, the value of β can be computed from (since $B_r = 0$ in the z=0 plane) the following relation

$$\beta = \frac{\int_0^a p r^2 dr}{\int_0^a (B_\theta^2 + B_\phi^2) r^2 dr}$$

4   RESULTS

The eigensolution with lowest energy dissipation rate for the $n = 0, m = 1$ state has the eigenvalue $\lambda a = 3.995$. For this value of λa, the fields given in eqs.(11)-(13) satisfy the conducting boundary conditions. A plot of $\lambda = \mathbf{j} \cdot \mathbf{B}/B^2$ in the z =0 plane is shown in fig. (2). This is similar to some of the experimental observations[2-5], where a non-constant $j_\parallel/B$ profile is obtained in contrast to the usual Taylor state for which λ= constant. The profiles of poloidal B_θ and toroidal B_z magnetic field components in the z= 0 plane are shown in fig. 3.
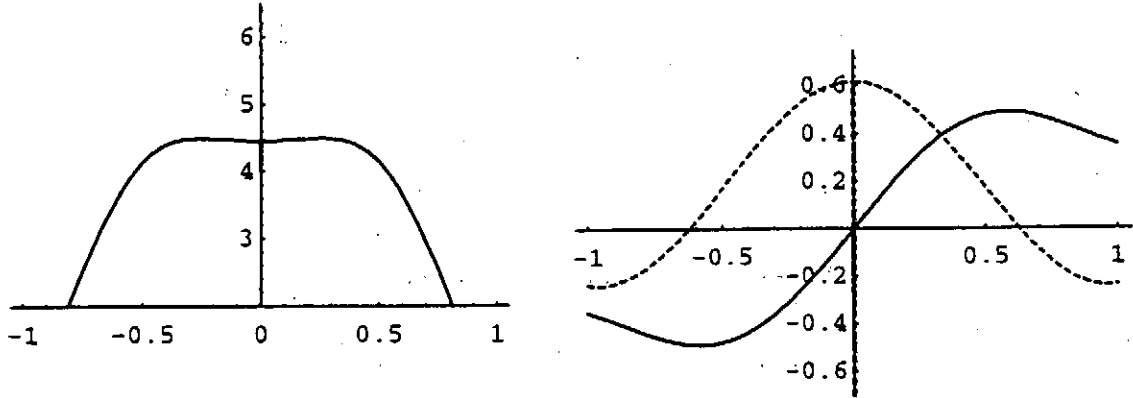
Fig. 2   A plot of $j_\parallel/B$ against r/a for the minimum dissipation state with $\lambda a = 3.99$.

Fig. 3   A plot of B_θ and B_z against r/a.

The pressure profile for this state is shown in fig. 4, and exhibits a peak at the center. The value of β in the $z = 0$ plane was calculated numerically and found to be about 40 %.
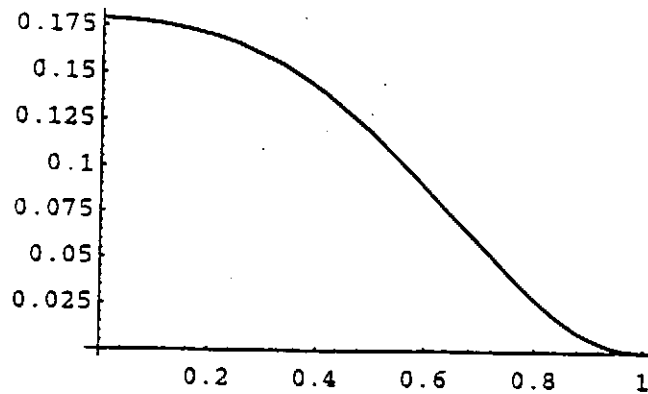

Fig. 4 Pressure profile for $\lambda a = 3.99$.

For the $m = 1, n = 0$ state with $\lambda a = 5$, the fields do not satisfy the boundary conditions given by eq. (10). A plot of the ration $j_\parallel/B$ against r/a is shown in fig. 5 and shows a double humped behaviour. The corresponding pressure profile shown in fig. 6 exhibits a hollow nature. The results are similar to the solutions obtained by solving the Grad-Shafranov equation numerically [9] where a linear ψ pressure model is assumed (ψ is the poloidal flux function).
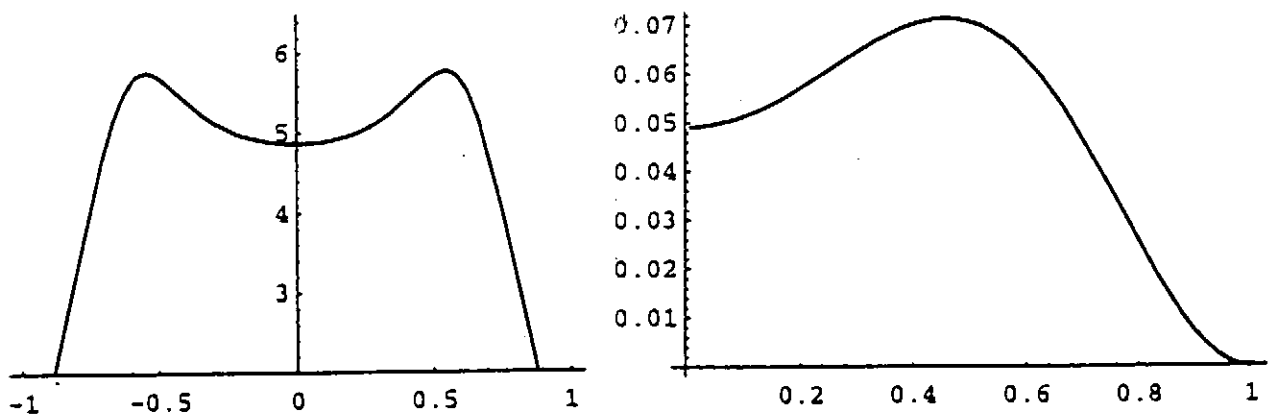

Fig. 5   A plot of $j_\parallel/B$ against r/a for $\lambda a = 5.0$.

Fig. 6   Pressure profile for $\lambda a = 5.0$.

References

[1] M.N. Rosenbluth and M.N. Bussac, Nucl. Fusion **19**, 489 (1979).

[2] G.W. Hart et. al., Phys. Rev. Lett. **51**, 1558 (1983).

[3] F. J. Wysocki, Phys. Rev. Lett. **61**, 2457 (1988).

[4] S. O. Knox et. al., Phys. Rev. Lett. **56**, 842 (1986).

[5] R. Martin et. al., Plasma Phys. Contr. Fusion **35**, 269 (1993).

[6] D. Montgomery and L. Phillips, Phys. Rev. A **38**, 2953 (1988).

[7] S. Chandrasekhar and P.C. Kendall, Astrophys. J. **126**, 457(1957).

[8] B. Dasgupta et. al., Phys. Rev. Lett. **81** 3144 (1998).

[9] T. Yeh and G.K. Morikawa, Phys. Fluids **14**, 781 (1971).

Virtual Cathode in a Spherical Inertial Electrostatic Confinement

Hiromu Momota and George H. Miley

Dept. Nuclear Engineering, University of Illinois at Urbana-Champaign,

214 Nuclear Engineering Lab. 103 S. Goodwin Avenue, Urbana, IL 61801, USA

INTRODUCTION

The Spherical Inertia Electrostatic Confinement (SIEC) is widely accepted as one of the simplest candidate among various fusion approaches for controlled fusion. Indeed, it has no externally applied magnetic field and ions are focused in the small volume near the spherical center. Fig.1 shows a cross section of the single-grid Spherical IEC. When deuterium is used, ions produced in the discharge are extracted from the plasma by the cathode grid, accelerated, and focused in the center. The grid provides recirculation of ions, increasing the ion density. Consequently a very high-density core of fuel ions is created in the center region. This might enhance fusion reactions, since the reaction rate is proportional to the square of the fuel density. Nevertheless, the high density of ions produces a high potential hill, which decreases the kinetic energy of incoming ions and consequently reduces fusion reactions. Electron effects are thought to change the potential shape in such a way as to avoid this problem. In an experiment at high currents, a potential structure develops in the non-neutral plasma, creating virtual electrodes that further enhance ion containment and recirculation [1-2]. (see Fig.2). Hirsch [3] pointed out firstly an existence of the potential well or a virtual cathode structure in the potential hill. Nevertheless, discussions on the virtual cathode have still continued. This is attributed to the fact that Hirsch have discussed only a simple case where the charged particles are monoenergetic and have no angular momentum. Analyses including angular momentum have been reported [4-8]. These studies, however, introduced unacceptable assumptions or have been completely numerical such that the underlying phenomena become hard to understand. Thus the topic assumes a strong importance [7]. It is the purpose of this paper to clarify the formation mechanism of the virtual cathode and to derive the conditions necessary for formation of a virtual cathode structure.

We will discuss the steady-state solution for two opposite cases. One is the case where electron collisions are so small that the velocity distribution function can be described in terms of the collision-free kinetic equation. The second is the case where electrons suffer collisions so frequently that the collision-free kinetic equation is no more applicable. The electrons are described in terms of Boltzman's distribution, corresponding to thermal equilibrium. In both cases, ions are collision-free and their velocity vector also diverges away from the center by a small angle.

DIVERGENT VELOCITY OF IONS

In experimental devices in the laboratory, ions are generated outside the spherical cathode structure, which are negatively biased. Ions are accelerated by the cathode and pass through the cathode region towards the center. Ions arrive at the central region and then turn back to the cathode region, where they are reflected again towards the center. The spherical symmetry of the electrostatic field near the cathode region is, however, incomplete because the cathode has a discrete structure. This non-symmetric electric field near the cathode region gives the ion beam a certain divergence. Let the divergence of the ion velocity vector towards the center be Δ_i at the cathode region. The distribution function of ions at $r = a$ takes the form:

$$f_s(a,v_r,v_{\perp a}) = \frac{n_{sa}}{2\pi v_a^2} \delta(|v_a| - V_s) \frac{1}{\Delta_s^2} \exp(-\gamma_a^2 / \Delta_s^2) \qquad \sin\gamma \equiv \frac{v_{\perp}}{v} \tag{1}$$

The distribution function at a radius $r = r$ is then given by:

$$f_s(r,v_r,v_{\perp}) = \frac{n_{sa}}{2\pi v_a} \sqrt{\frac{M_s}{2}} \frac{\delta(v_r - \sqrt{2[H_s - q_s\varphi(r)]/M_s - v_{\perp}^2})}{\sqrt{H_s - q_s\varphi(r) - M_s v_{\perp}^2/2}}$$

$$\times \frac{1}{\Delta_s^2} \exp\left[-\frac{v_{\perp}^2}{2(H_s - q_s\varphi_a)\Delta_s^2 a^2 / M_s r^2}\right] \tag{2}$$

This equation shows that the divergence of the particle becomes larger near the spherical center than at the cathode region, providing that the effects of electrostatic potential are inappreciable.

The particle density is obtained by integrating the above equation over velocity space, giving:

$$n_s(r) = \frac{n_{sa} a^2}{r^2} \sqrt{\frac{H_s - q_s\varphi_a}{H_s - q_s\varphi(r)}} \frac{1}{D_s^2(r)} \int_0^1 \frac{\exp[-\xi / D_s^2(r)]}{\sqrt{1-\xi}} d\xi$$

$$where, \qquad D_s^2(r) \equiv \frac{\Delta_s^2 a^2}{r^2} \frac{H_s - q_s\varphi_a}{H_s - q_s\varphi(r)} \tag{3}$$

In the region close to the center ($r \ll \Delta_s a$), where the value $D_s^2(r)$ is much larger than unity, we obtain:

$$n_s(r) = \frac{2n_{sa}}{\Delta_s^2} \sqrt{\frac{H_s - q_s\varphi_a}{H_s - q_s\varphi(r)}} \left(1 - \frac{2}{3D_s^2(r)}\right). \tag{4}$$

Thus the ion density in the dense core region is roughly $2n_{sa} / \Delta_s^2$. This assumes the ion density is low enough and accordingly the effects of electrostatic potential can be ignored.

For the case of collision-free electrons, the distribution function is expressed by equation (3), where $q_s = -e$ and $n_{sa} = n_{ae}$. Nevertheless, since the kinetic energy of electrons is very low at

the cathode region, they are strongly effected by perturbations in the electrostatic potential. Therefore, the above arguments concerning the core density and core radius break down. Results are still obtainable after numerical calculations, and will be presented in the following section.

Discussions presented so far are applicable in a limiting case where particles suffer no collisions. In general, the collision frequency between electrons is much larger than that of ions. Thus within a SIEC, the electrons suffer a large self-collision rate. Formation of a virtual cathode for this case has been studied by Ohnishi et al. [2]. They have assumed, however, charge neutrality of the plasma, and no solution to Poisson equation has been obtained. In a stationary plasma where the mean electron-electron collision time is much smaller than the mean life time of electrons trapped within the chamber, the distribution function of electrons is determined by detailed balance, resulting simply in Boltzman's distribution:

$$n_e(r) = n_{ea} Exp\left[-\frac{e}{kT}(\varphi(r) - \varphi_a) \right].$$
(5)

Throughout the present paper, we are interested for a case ion collision is negligibly small and consequent ion distribution functions are given by the equation (2).

The exact electrostatic potential has to be determined from Poisson's equation:

$$-\varepsilon_0 \frac{1}{r^2} \frac{d}{dr} r^2 \frac{d\varphi}{dr}(r) = Zen_i(r) - en_e(r)$$
(6)

This equation is supplemented by the equations for particle density given in equation (3) or (5) as a function of the electrostatic potential. The quantity Z stands for the charge number of the ion and we will henceforth put it equal to unity since we are interested in D-D fusion. Equation (6) with (3) or (5) for the particle density is a complicated nonlinear differential equation and we are unable to obtain its solution analytically. A certain numerical calculation is, therefore, needed to study the detail of the virtual cathode. An outline of these calculations and the resulting solutions are presented in the next section.

NUMERICAL SOLUTIONS TO POISSON'S EQUATION

In carrying out numerical calculations, we will employ the following model:

(a) The electrostatic potential φ_a at $r = a$ is approximately the same as the voltage $-V_g$ applied onto the spherical cathode. This condition gives us one of the needed boundary conditions for obtaining a solution to Poisson's equation.

(b) Ions are first produced outside the cathode region where the electrostatic potential is zero. The hamiltonian of ions is therefore zero.

(c) Concerning electron birth, we are considering two opposite cases. In the first case, electrons

are completely collision-free and their birth are at $r = a$ with a small radial velocity $\varepsilon e V_g$. Then the electron hamiltonian of is $e V_g (\varepsilon + 1)$. The ratio of electron density to the ion density α at the cathode region is a controllable variable. In the opposite case, electrons suffer many collisions and, therefore, their density is given by Boltzman's distribution. The ratio of electron density to the ion density α for this case is still a variable.

(d) The divergence Δ of ions is 0.2 at the cathode region.

For the purpose of simplifying the equations to be solved numerically, a set of non-dimensional variables is introduced:

$$\frac{r}{a} \equiv \rho, \qquad 1 - \frac{-\varphi(r)}{V_g} \equiv F(\rho), \quad \therefore F(\rho = 1) = 0,$$

$$\frac{n_i(r)}{n_i(a)} \equiv N_i(\rho), \quad \therefore N_i(\rho = 1) = 1 \qquad \frac{n_e(r)}{n_i(a)} \equiv N_e(\rho), \; N_e(\rho = 1) = \alpha \qquad (7)$$

$$\frac{n_i(a)e}{\varepsilon_0} \frac{a^2}{V_g} \equiv \Omega^2 \quad (= \omega_{\mathrm{pi}}^2 \, a^2 / v_i^2)_{r=a}$$

In terms of these non-dimensional variables, the equation set takes the form:

$$\frac{1}{\rho^2} \frac{d}{d\rho} \left(\rho^2 \frac{dF}{d\rho}(\rho) \right) = - \Omega^2 [N_i(\rho) - N_e(\rho)] \qquad (8)$$

$$N_i(\rho) = \frac{1}{\Delta_i^2} \sqrt{1 - F(\rho)} \int_0^1 \frac{d\xi}{\sqrt{1-\xi}} \exp[-\frac{\rho^2}{\Delta_i^2}(1 - F(\rho))\xi] \qquad (9)$$

and

$$N_e(\rho) = \frac{\alpha}{\Delta_e^2} \sqrt{\frac{F(\rho)+\varepsilon}{\varepsilon}} \int_0^1 \frac{d\xi}{\sqrt{1-\xi}} \exp[-\frac{\rho^2}{\Delta_e^2} \frac{F(\rho)+\varepsilon}{\varepsilon}\xi] \qquad (10)$$

or

$$N_e(\rho) = \alpha \; \mathrm{Exp}[k^2 F(\rho)] \qquad k^2 \equiv \frac{e V_g}{\kappa T} \qquad (11)$$

The boundary conditions associated to these equations are:

$$F(1) = 0$$

$$\frac{dF}{d\rho}(1) = -\Omega^2 \int_0^1 [N_i(\rho) - N_e(\rho)]\rho^2 d\rho \qquad (12)$$

A comment is required about the boundary conditions: since all the physical quantities are regular functions of the normalized radius ρ, the second boundary condition should be $dF / d\rho = 0$ at

$\rho = 0$. This condition at the spherical center requires certain complicated procedures for solving the nonlinear differential equation. We employed, therefore, an alternative boundary condition. By assuming tentatively a certain value of $dF / d\rho(\rho = 1)$, we execute flip-flop calculations. The resultant value of the tentatively obtained total charge will be employed as the value $dF / d\rho(\rho = 1)$ for the next step of the iteration. If the result satisfies the second boundary condition in (12), it is adopted as the solution. Once the result satisfies the condition (12), it also satisfies the condition $dF / d\rho = 0$ at $\rho = 0$. Further, we applied the following approximated formula for the integral in equations (9) and (10):

$$\int_0^1 \frac{\exp(-\eta^2 t)}{\sqrt{1-t}} dt \approx 2\exp\left(-\frac{5}{4}\eta^2\right) + \frac{\eta^2}{1+\eta^4} \tag{13}$$

This approximation significantly simplifies the calculation. The validity of the approximation is illustrated in Fig.1. The approximated formula is only slightly larger than the integral, however, the difference seems insignificant relative to our results. Results of numerical calculations are exhibited in from Fig.2 to Fig.6 for a various densities of ions and electrons at the cathode region. These results are discussed in some detail next.

Figs. 3 (a)-(c) shows a solution to equations (7)-(9) and (12) for thermal electrons in a low collision and low-density plasma. The density parameter $en_{ia}a^2 / \varepsilon_0 V_g$ is as small as 0.1 and electron density and ion density is the same at the cathode region. Fig.3 (a) shows the density profile. Because of the small electrostatic-potential for this low-density operation, ions are little affected by the potential. Ion focuses into a high-density core with a high electrostatic potential. Ion density at the core of radius $a\Delta_i$ is approximately $2 / \Delta_i^2$ times the ion density n_{ia} at the cathode region. The density profile of the electrons is exhibited in Fig.3 (b). Since thermal electrons have no focusing property, their profile is broad. A broad profile of thermal electron is disable to create a high peak of its density inside the potential hill near the center. Consequently, no virtual cathode or potential well appears in the potential hill. We confirm these facts about the potential profile in Fig. 3(c).

Figs. 4 (a)-(c) show a solution for a case where only the electrons differ from the conditions used in the previous solution. As for ions, their essential properties are as same as the previous case [Fig.4 (a)]. The representative kinetic energy of electrons at the cathode region is as small as 0.0003 times the applied voltage onto the cathode. Accordingly, the canonical angular momentum of electrons is very small. The radial electric field accelerates electrons towards the center, keeping their angular momentum constant. In other words, the divergence of electron flow decreases at an inner region, which allows electrons to penetrate deep inside the potential hill. Consequent electron focuses into a small region around the center and a high peak in the density profile of electron forms a potential well inside the potential hill. This is shown in Fig. 4 (b). The appearance of the virtual cathode in the potential hill is a quite general result in an aligned flow of electrons, as is seen in Fig. 4(c).

Figs. 5 (a)-(c) show the effects of the divergence of aligned electrons in a collision-free plasma.

Only the divergence changes and all other plasma parameters are same as the two prior examples. The divergence Δ of electron is 0.4, 0.1, and 0.025 in Fig.5 (a), Fig.5 (b), and Fig.5 (c), respectively. The sharp electron focusing makes it possible to achieve a virtual cathode, but this effect is not enough to appreciably cancel the potential hill.

Figs. 6 (a)-(c) and Figs. 7 (a)-(c) concern cases of aligned electrons while the ion density at the cathode region changes. The divergence of ions Δ_i is chosen as 0.2 and that of electrons Δ_e is 0.025. Figs. 6 (a)-(c) show the density profile of ions versus the edge density of the ions. If the ion density at the cathode region increases, the effects of electrostatic potential become appreciable. As is shown in Fig.6 (a), in the case of low ion edge density $en_{ia}a^2 / \varepsilon_0 V_g = 0.1$, the electrostatic potential only slightly changes the density profile of ions. For a case of intermediate ion edge density $en_{ia}a^2 / \varepsilon_0 V_g = 0.5$, the large self-electrostatic field decelerates the ion motion. This results immediately in an increase of the ion density, as is shown in Fig. 6 (b). Fig. 6(c) shows potential profile for the case of high edge ion density ($en_{ia}a^2 / \varepsilon_0 V_g = 0.8$). Due to the large effect of the electrostatic potential, the deceleration of radial motion by ions produces a large bump in the ion density profile. The location of the bump is the point where equation $e\varphi(r)r^2 = \Delta_i^2 e\varphi_a a^2$ is approximately satisfied. This condition exactly corresponds to condition (14). An appreciable number of ions are reflected at this point to form the density bump.

It may be interesting to watch the potential profile associated to the bump up of ion density. Potential profiles are exhibited in Figs. 7 (a)-(c) corresponding to Figs. 6 (a)-(c), respectively. For the case of high edge density where the bump in ion density profile appears, no bump in the potential profile appears. Throughout our numerical calculations, no second virtual anode follows the density bumps of ion that have been pointed out by Hirsch [1]. Ions with a certain angular momentum are easier to reflected back compared with ions with zero angular momentum. Thus a majority of ions are reflected back before they can form a virtual anode.

Figs. 8 (a)-(c) show the density profile of ions, versus the edge densities of ion for the case of thermal electrons. The parameters used are essentially the same as Figs. 6 (a)-(c) respectively, except for the divergence angle of electrons. No second peak of ion density is observed, even in the case of high ion density. No second virtual anode appears either in this case.

Application of a high edge density of aligned electrons focused towards the center enables a larger depth of the virtual cathode. This fact is demonstrated in Figs. 9 (a)-(c), for the case of high density, $en_{ia}a^2 / \varepsilon_0 V_g = 0.8$. By increasing the electron density at the edge, the electron density is increased everywhere in SIEC. The electron density near the center also increases and consequently a deep well on the potential hill near the center is formed. The potential of nearly 90 % of the ion kinetic energy at the cathode region decreases to 45 % when a high electron density is applied at the cathode region.

Similar trials to increase the edge density of thermal electrons have been done. Nevertheless, no solution is found if the edge density of electrons is more than 1.4 times the ion density.

No ion hole appears inside the virtual cathode for the case of aligned electrons since ions with small angular momentum cover the potential well to form a peak of the ion density at the center.

The increment that is considered for the electron density at the cathode region is as large as factor six. This brings, however, a decrease of the total electric charge of a system of only 14 percent. If electrons are thermal and consequently distributed broadly, neither a secondary ion hill nor a virtual cathode is formed.

CONCLUSIONS AND DISCUSSIONS

We have studied double structure or virtual cathode formation of a spherical inertial electrostatic confinement. The study concerns particle's distribution with divergence Δ of the direction of the velocity around the center and addition of edge electron density.

(a) The angular momentum of both ions and electrons causes a virtual cathode in a potential hill near the spherical center of SIEC.

(b) The potential hill is small if the density parameter $en_{ia}a^2 / \varepsilon_0 V_g$ is much smaller than unity. In this case, the radius of the high-density core is $a\Delta$ and ion density at the core is $2 / \Delta^2$ times the ion density at the cathode region.

(c) If the density parameter $en_{ia}a^2 / \varepsilon_0 V_g$ is close to unity, the height of the potential hill becomes appreciable. This causes a large bump in the density profile of ions for the case of aligned electrons. No potential bump or virtual anode, however, appears to be associated with the ion bump. For the case of thermal electrons, no ion bump appears.

(d) An appreciable potential well inside the potential hill appears at a high-density operation if one applies an enhanced electron density, as well as a small divergence of aligned electrons at the cathode region.

(e) No ion hole appears in the potential well, but ion peaks at the potential well.

Applications of conclusions of these studies are only restricted for the limited situation described in section 4. For cases where the density parameter $en_{ia}a^2 / \varepsilon_0 V_g$ is larger than unity, no solution to the nonlinear Poisson equation has been obtained.

It has been obvious that the electron plays an essential role in virtual cathode formation. Detailed studies on the electron distribution function are needed to estimate precisely the laboratory SIEC.

The density limit $en_{ia}a^2 / \varepsilon_0 V_g < 1$ for a steady solution restricts the development of the SIEC to a low power level fusion device. A steady-state device may satisfy the condition $n_{ia}a^2 \approx 2.5 \times 10^{12} / m$.

When we apply high-density parameters larger than unity, numerical solutions to Poisson's equation take complex value at the inner region of SIEC. This suggests that a certain additional term is needed to obtain a physically acceptable solution. The solution might be a time-dependent one, involving an unstable or oscillating solution.

In this paper, we ignored all inter-particle collisions. However, further studies on a

collisional equilibrium scale of related fueling and loss processes are essential for understanding the complete picture for a SIEC.

ACKNOWLEDGEMENTS

REFERENCES

[1] G. H. Miley, et al., "Discharge Characteristics of the Spherical Inertial Electrostatic Confinement (IEC) Device," *IEEE Trans. on Plasma Science*, **25**, 4, 733-739, (1997).

[2] George H. Miley and Yibin Gu , "IEC Neutron Source Development And Potential Well Measurements," *Current Trends In International Fusion Research*, E. Panarella, ed., NRC Press, Canada, 1999.

[3] HIRSCH, R.L.J. *Appl. Physics* **38**, 4522 (1969).

[4] OHNISHI, M., YAMAMOTO Y., YOSHIKAWA K., and SATO K., "Multi-Potential Well Formation and Neutron Production in Inertial-Electrostatic Confinement Fusion by Numerical Simulations," in *Proceedings of 16th IEEE/NPSS Symposium on Fusion Energy* Vol.2(1995), 1468-1471.

[5] HU, K. M. and KLEVANS, E. H., *Phys. Fluids* **17**(1974), 227-231

[6] CHERRINGTON B. E. et al., Annals New York Academy of Sciences.

[7] TZONEV, I. V., MILEY, G. H., and NEBEL, R. A., "A Computational Study of the Convergence of Large Angular Momentum, High Current Ion Beams in an Inertial Electrostatic Confinement (IEC) Device," *International Conference on Phenomena in Ionized Gases XXII* **4**(1995), 197-198

[8] SATSANGI, A. J., "Light Intensity Measurements of an Inertial Electrostatic Confinement Fusion Plasma," M.S. thesis, Department of Nuclear Engineering, University of Illinois at Urbana-Champaign, 1996.
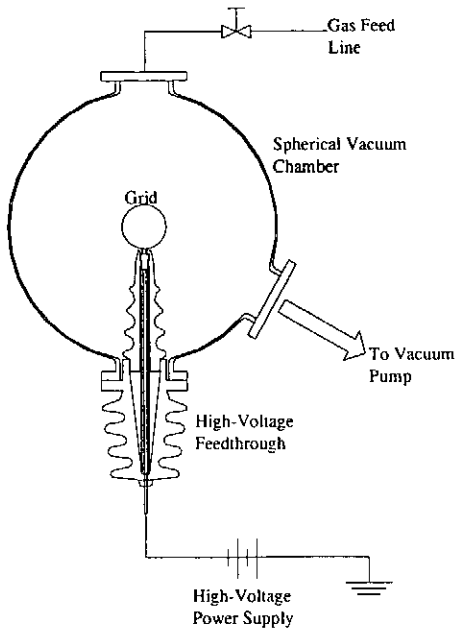
[9] NEVINS, W. M. *Phys. Plasma* **2**, 3804 (1995)

Fig.1: Cross section showing construction of the single-cathode Spherical IEC. This design, along with a special "open" cathode design that provides a STAR mode plasma, are used in UI neutron source work
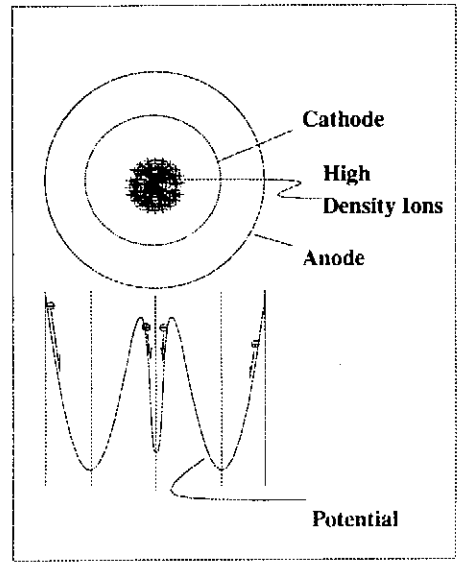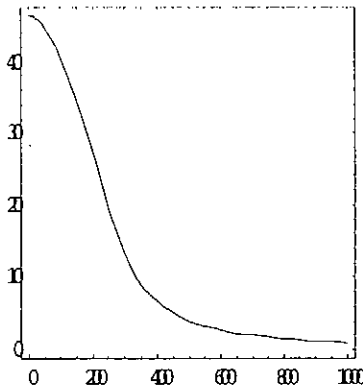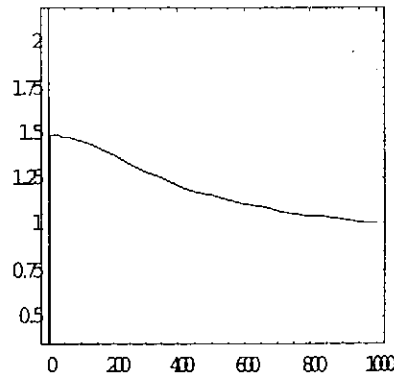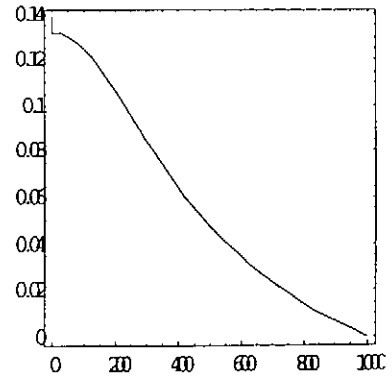

Fig.2: Potential structure develops in the non-neutral plasma, creating virtual cathode

(a): ion density

(b): electron density

(c): electrostatic potential

Fig.3: A radial profile of ion density, electron density, and electrostatic potential in a case of low density plasma: $e n_{ia} a^2 / \varepsilon_0 V_g = 0.1$. Other parameters are $n_{ea} / n_{ia} = 1$, divergence of ions $\Delta_i = 0.2$ and electrons are thermal.

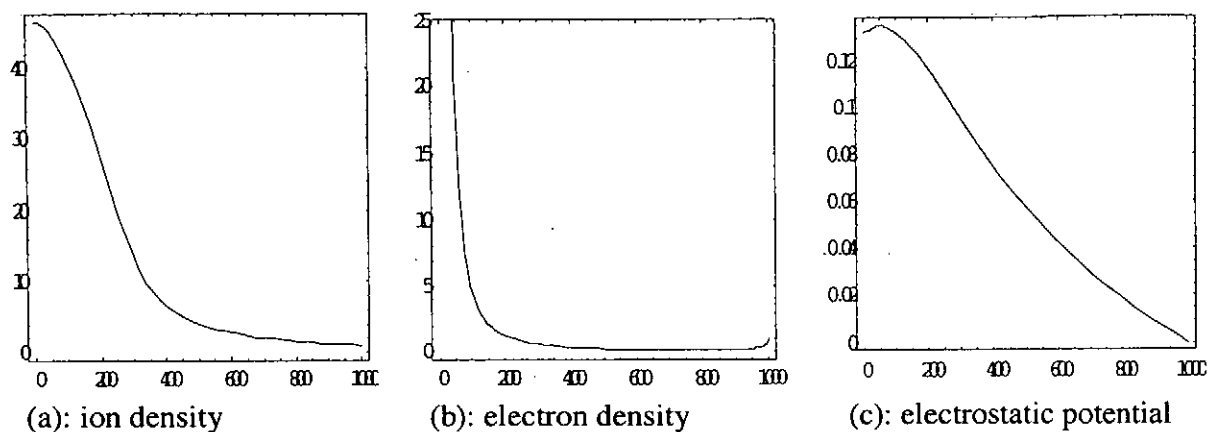(a): ion density (b): electron density (c): electrostatic potential

Fig.4: A radial profile of ion density, electron density, and electrostatic potential in a case of low-density plasma: $en_{ia}a^2 / \varepsilon_0 V_g = 0.1$. Other parameters are $n_{ea}/n_{ia} = 1$, divergence of ions $\Delta_i = 0.2$, and that of electrons $\Delta_e = 0.1$.

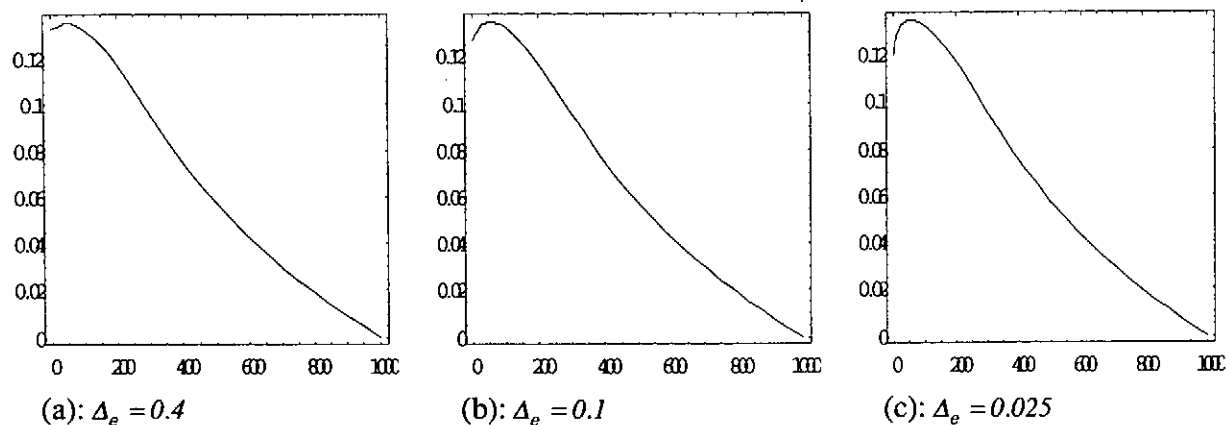(a): $\Delta_e = 0.4$ (b): $\Delta_e = 0.1$ (c): $\Delta_e = 0.025$

Fig.5: Potential profile for different electron divergence in low-density plasma ($en_{ia}a^2 / \varepsilon_0 V_g = 0.1$). Other parameters are $n_{ea}/n_{ia} = 1$, and $\Delta_i = 0.2$.

(a): $en_{ia}a^2 / \varepsilon_0 V_g = 0.1$ (b): $en_{ia}a^2 / \varepsilon_0 V_g = 0.5$ (c): $en_{ia}a^2 / \varepsilon_0 V_g = 0.8$
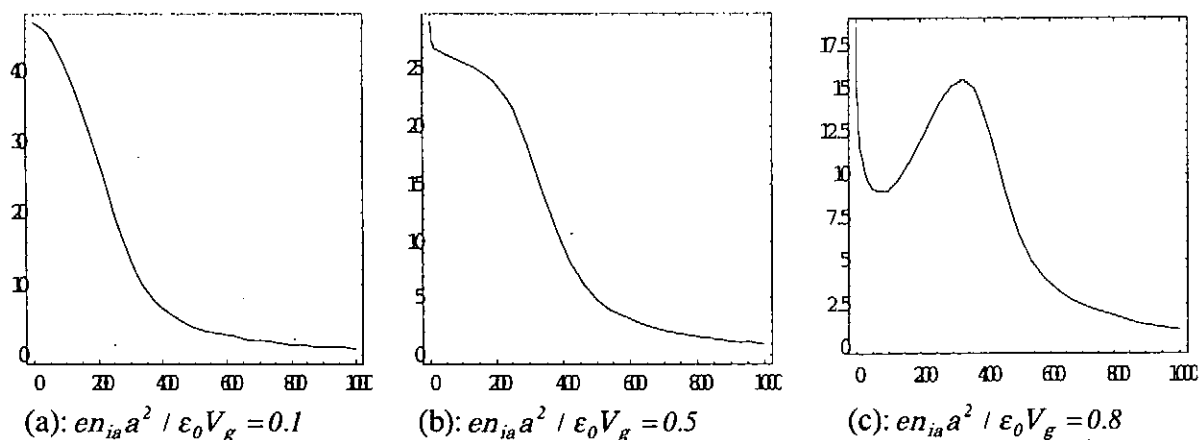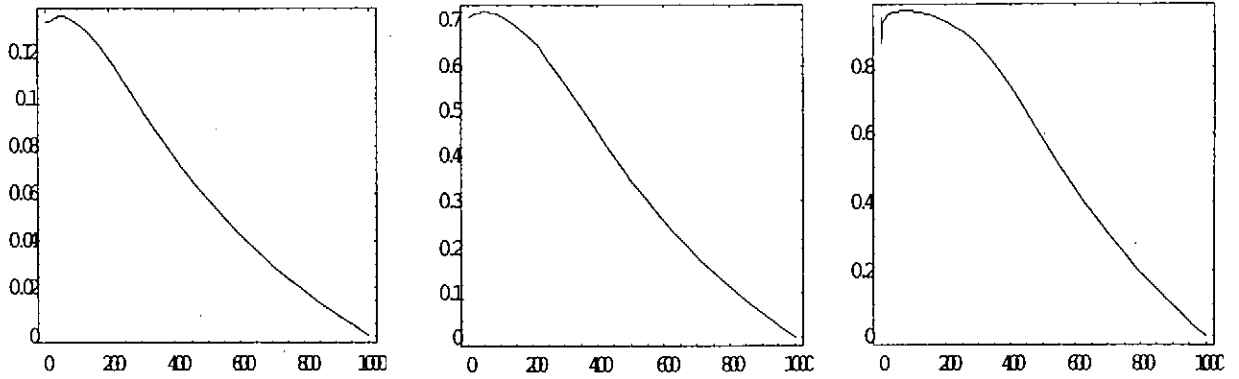
Fig.6: Density profiles of ions at various density in a case of $n_{ea}/n_{ia} = 1$, $\Delta_i = 0.2$, and $\Delta_e = 0.025$.
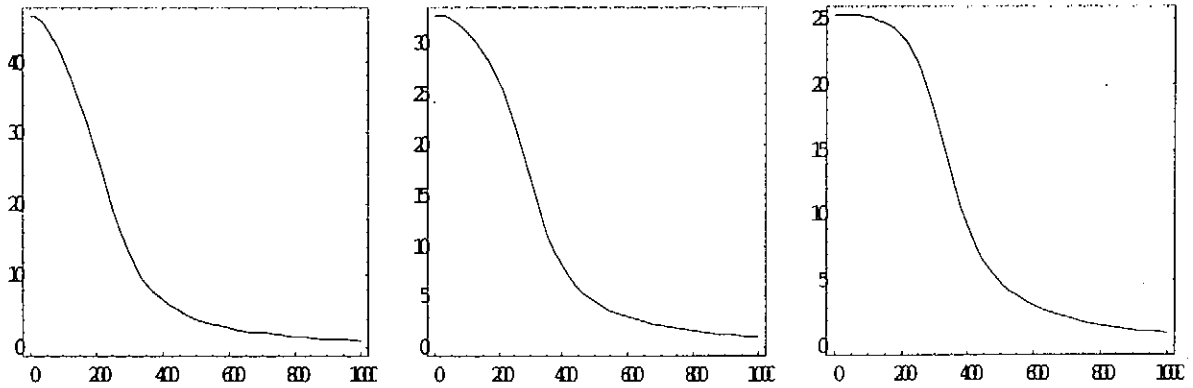
(a): $en_{ia}a^2 / \varepsilon_0 V_g = 0.1$ (b): $en_{ia}a^2 / \varepsilon_0 V_g = 0.5$ (c): $en_{ia}a^2 / \varepsilon_0 V_g = 0.8$

Fig.7: Potential profile at various densities for a case of $n_{ea}/n_{ia} = 1$, $\Delta_i = 0.2$, and $\Delta_e = 0.025$.
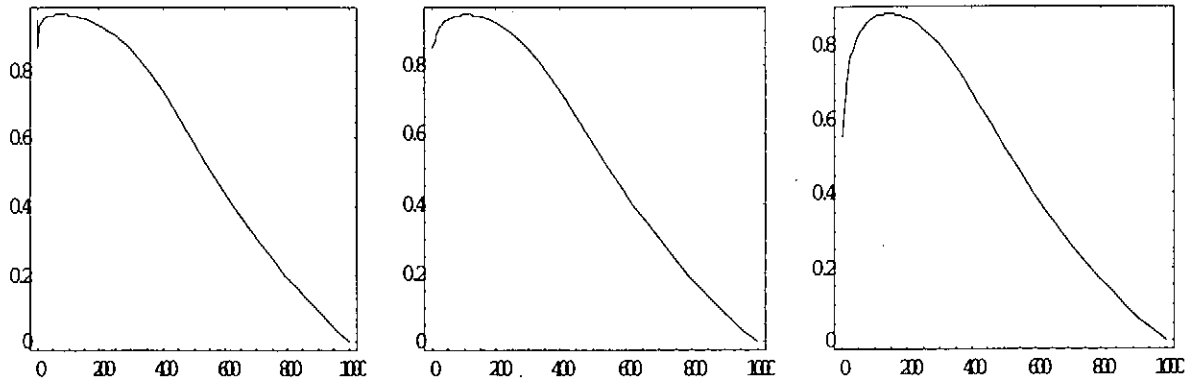

(a): $en_{ia}a^2 / \varepsilon_0 V_g = 0.1$ (b): $en_{ia}a^2 / \varepsilon_0 V_g = 0.5$ (c): $en_{ia}a^2 / \varepsilon_0 V_g = 0.8$

Fig.8: Density profiles of ions at various densities for a case of $n_{ea}/n_{ia} = 1$, $\Delta_i = 0.2$, and thermal electrons

(a): $n_{ea}/n_{ia} = 1$ (b): $n_{ea}/n_{ia} = 2.5$ (c): $n_{ea}/n_{ia} = 6.0$

Fig.9: Potential profiles of various density rations of electron and ion at the cathode region in a High-density plasma: $en_{ia}a^2 / \varepsilon_0 V_g = 0.8$, $\Delta_i = 0.2$, and $\Delta_e = 0.025$

Publication List of NIFS-PROC Series

NIFS-PROC-1   " *U.S.-Japan on Comparison of Theoretical and Experimental Transport in Toroidal Systems Oct. 23-27, 1989* ", Mar. 1990

NIFS-PROC-2   " *Structures in Confined Plasmas –Proceedings of Workshop of US-Japan Joint Institute for Fusion Theory Program– *"; Mar. 1990

NIFS-PROC-3   " *Proceedings of the First International Toki Conference on Plasma Physics and Controlled Nuclear Fusion –Next Generation Experiments in Helical Systems– Dec. 4-7, 1989"* Mar. 1990

NIFS-PROC-4   " *Plasma Spectroscopy and Atomic Processes –Proceedings of the Workshop at Data & Planning Center in NIFS–*"; Sep. 1990

NIFS-PROC-5   " *Symposium on Development of Intensed Pulsed Particle Beams and Its Applications February 20 1990"*; Oct. 1990

NIFS-PROC-6   " *Proceedings of the Second International TOKI Conference on Plasma Physics and Controlled Nuclear Fusion , Nonlinear   Phenomena in Fusion Plasmas -Theory and Computer Simulation-";* Apr. 1991

NIFS-PROC-7   " *Proceedings of Workshop on Emissions from Heavy Current Carrying High Density Plasma and Diagnostics";* May 1991

NIFS-PROC-8   " *Symposium on Development and Applications of Intense Pulsed Particle Beams, December 6 - 7, 1990"*; June 1991

NIFS-PROC-9   "*X-ray Radiation from Hot Dense Plasmas and Atomic Processes"*; Oct. 1991

NIFS-PROC-10   " *U.S.-Japan Workshop on "RF Heating and Current Drive in Confinement Systems Tokamaks" Nov. 18-21, 1991,* Jan. 1992

NIFS-PROC-11   " *Plasma-Based and Novel Accelerators (Proceedings of Workshop on Plasma-Based and Novel Accelerators) Nagoya, Japan, Dec. 1991";* May 1992

NIFS-PROC-12   " *Proceedings of Japan-U.S. Workshop P-196 on High Heat Flux Components and Plasma Surface Interactions for Next Devices";* Mar. 1993

NIFS-PROC-13   「NIFS シンポジウム
「核燃焼プラズマの研究を考える―現状と今後の取り組み方」
1992 年 7 月 15 日、核融合科学研究所」1993 年 7 月
NIFS Symposium "Toward the Research of Fusion Burning Plasmas -Present Status and Future strategy-", 1992 July 15, National Institute for Fusion Science"; July 1993 (in Japanese)

NIFS-PROC-14   " *Physics and Application of High Density Z-pinches",* July 1993

NIFS-PROC-15   岡本正雄、講義「プラズマ物理の基礎」
平成 5 年度　総合大学院大学1994 年 2 月
M. Okamoto,
"Lecture Note on the Bases of Plasma Pysics"Graduate University for Advanced Studies Feb. 1994
(in Japanese)

NIFS-PROC-16   代表者　河合良信
平成 5 年度　核融合科学研究所共同研究
研究会報告書「プラズマ中のカオス現象」
"Interdisciplinary Graduate School of Engineering Sciences" Report of the meeting on Chaotic Phenomena in Plasma Apr. 1994 (in Japanese)

NIFS-PROC-17   平成 5 年度 NIFS シンオジウム報告書
「核融合炉開発研究のアセスメント」平成 5 年 11 月 29 日-30 日　於　核融合科学研究所
"Assessment of Fusion Reactor Development" Proceedings of NIFS Symposium held on November 29-30, 1993 at National Insitute for Fusion Science" Apr. 1994(in Japanese)

NIFS-PROC-18   "*Physics of High Energy Density Plasmas Produced by Pulsed Power"* June 1994

NIFS-PROC-19   K. Morita, N. Noda (Ed.),

"*Proceedings of 2nd International Workshop on Tritium Effects in Plasma Facing Components at Nagoya University, Symposion Hall, May 19-20, 1994*", Aug. 1994

NIFS-PROC-20 研究代表者　阿部　勝憲　（東北大学・工学部）
所内世話人　野田信明
平成 6 年度　核融合科学研究所共同研究 [研究会] 「金属系高熱流束材料の開発と評価」成果報告書

K. Abe and N. Noda (Eds.),
"*Research and Development of Metallic Materials for Plasma Facing and High Heat Flux Components*"
Nov. 1994(in Japanese)

NIFS-PROC-21 世話人：森田　健治（名大工学部）、金子　敏明（岡山理科大学理学部）
「境界プラズマと炉壁との相互作用に関する基礎過程の研究」研究会報告
K. Morita (Nagoya Univ.), T. Kaneko (Okayama Univ. Science)(Eds.)
"*NIFS Joint Meeting "Plasma-Divertor Interactions" and "Fundamentals of Boundary Plasma-Wall Interactions" January 6-7, 1995 National Institute for Fusion Science*" Mar. 1995 (in Japanese)

NIFS-PROC-22 代表者　河合　良信
プラズマ中のカオス現象
Y. Kawai,
"*Report of the Meeting on Chaotic Phenomena in Plasma, 1994*" Apr. 1995 (in Japanese)

NIFS-PROC-23 K. Yatsui (Ed.),
"*New Applications of Pulsed, High-Energy Density Plasmas*"; June 1995

NIFS-PROC-24 T. Kuroda and M. Sasao (Eds.),
"*Proceedings of the Symposium on Negative Ion Sources and Their Applications, NIFS, Dec. 26-27, 1994*",
Aug. 1995

NIFS-PROC-25 岡本　正雄
新古典輸送概論（講義録）
M. Okamoto,
"*An Introduction to the Neoclassical Transport Theory*" (*Lecture note*), Nov. 1995 (in Japanese)

NIFS-PROC-26 Shozo Ishii (Ed.),
"*Physics, Diagnostics, and Application of Pulsed High Energy Density Plasma as an Extreme State*";
May 1996

NIFS-PROC-27 代表者　河合　良信
プラズマ中のカオスとその周辺非線形現象
Y. Kawai,
"*Report of the Meeting on Chaotic Phenomena in Plasmas and Beyond, 1995*", Sep. 1996 (in Japanese)

NIFS-PROC-28 T. Mito (Ed.),
"*Proceedings of the Symposium on Cryogenic Systems for Large Scale Superconducting Applications*", Sep.
1996

NIFS-PROC-29 岡本　正雄
講義「核融合プラズマ物理の基礎 - I」
平成 8 年度　総合研究大学院大学　数物科学研究科　核融合科学専攻 1996年 10月
M. Okamoto
"*Lecture Note on the Fundamentals of Fusion Plasma Physics - I*" *Graduate University for Advanced Studies;* Oct. 1996 (in Japanese)

NIFS-PROC-30 研究代表者　栗下　裕明（東北大学金属材料研究所）
所内世話人　加藤　雄大
平成 8 年度核融合科学研究所共同研究 「被損傷材料の微小体積強度評価法の高度化」 研究会　1996年 10月　9日　於：核融合
科学研究所

H. Kurishita and Y. Katoh (Eds.)
NIFS Workshop on Application of Micro-Indentation Technique to Evaluation of Mechanical Properties of Fusion Materials, Oct. 9, 1996, NIFS ; Nov. 1996 (in Japanese)

NIFS-PROC-31 岡本　正雄
講義「核融合プラズマ物理の基礎 - II 」
平成 8 年度　総合研究大学院大学　数物科学研究科　核融合科学専攻　1997年 4月
M. Okamoto
"*Lecture Note on the Fundamentals of Fusion Plasma Physics - II*" *Graduate University for Advanced*

Studies; Apr. 1997 (in Japanese)

NIFS-PROC-32 代表者　河合　良信
平成8年度　核融合科学研究所共同研究　研究会報告「プラズマ中のカオスとその周辺非線形現象」

Y. Kawai (Ed)
Report of the Meeting on Chaotic Phenomena in Plasmas and Beyond, 1996; Apr. 1997 (mainly in Japanese)

NIFS-PROC-33 H. Sanuki,
Studies on Wave Analysis and Electric Field in Plasmas; July 1997

NIFS-PROC-34 プラズマ対向機器・PSI・熱・粒子制御合同研究会報告
平成 9 年 6 月 27 日（金）9:00 ～16:20　核融合科学研究所・管理棟 4 F 第 1 会議室
1997年　10月
T. Yamashina (Hokkaido University)
Plasma Facing Components, PSI and Heat/Particle Control June 27, 1997, National Institute for Fusion Science T. Yamashina (Hokkaido University) ; Oct. 1997 (in Japanese)

NIFS-PROC-35 T. Watari,
Plasma Heating and Current Drive; Oct. 1997

NIFS-PROC-36 T. Miyamoto and K. Takasugi (Eds.)
Production and Physics of High Energy Density Plasma; Production and Physics of High Energy Density Plasma; Oct. 1997

NIFS-PROC-37 (Eds.)T. Fujimoto, P. Beiersdorfer,.
Proceedings of the Japan-US Workshop on Plasma Polarization Spectroscopy and The International Seminar on Plasma Polarization Spectroscopy January 26-28, 1998, Kyoto; June 1998

NIFS-PROC-38 (Eds.) Y. Tomita, Y. Nakamura and T. Hayashi,
Proceedings of the Second Asian Pacific Plasma Theory Conference APPTC '97, January 26-28, 1998, Kyoto; Aug. 1998

NIFS-PROC-39 (Ed.) K. Hirano,
Production, Diagnostics and Application of High Energy Density Plasmas; Dec. 1998

NIFS-PROC-40 研究代表者　加古　孝（電気通信大学）
所内世話人　渡辺　二太
平成 10 年度核融合科学研究所共同研究 研究会「プラズマ閉じ込めに関連する数値計算手法の研究」
Ed. by T. Kako and T. Watanabe

Proceeding of 1998-Workshop on MHD Computations "Study on Numerical Methods Related to Plasma Confinement Apr. 1999

NIFS-PROC-41 Ed.) S. Goto and S. Yoshimura,
Proceedings of The US-Japan Workshop and The Satellite Meeting of ITC-9 on Physics of High Beta Plasma Confinement in Innovative Fusion System, Dec. 14-15, 1998, NIFS, Toki; Apr. 1999